

## ABSTRACT

Title of Document:                      Fabrication and Characterization of  
Compositionally-Graded Shape Memory  
Alloy Films

Directed By:                              Professor Hugh A. Bruck,  
Department of Mechanical Engineering

The miniaturization of engineering devices has created interest in new actuation methods capable of high power and high frequency responses. Shape memory alloy (SMA) thin films have exhibited one of the highest power densities of any material used in these actuation schemes. However, they currently require complex thermomechanical training in order to be actuated, which becomes more difficult as devices approach the microscale. Previous studies have indicated that SMA films with compositional gradients have the added feature of an intrinsic two-way shape memory effect (SME). In this work, a new method for processing and characterizing compositionally-graded transformable thin films is presented. Graded NiTi SMA films were processed using magnetron sputtering. Single and multilayer graded films were deposited onto bulk NiTi substrates and single crystal silicon substrates, respectively. Annealing the films naturally produced a compositional gradient across the film-substrate or film-film interface

through diffusion modification. The films were directly characterized using a combination of atomic force microscopy (AFM), x-ray diffraction and Auger electron spectroscopy. The compositional gradient was indirectly characterized by measuring the variation in mechanical properties as a function of depth using nanoindentation. The similarity of the indentation response on graded films of varying thickness was used to estimate the width of the graded interface. The nanoindentation response was predicted using an analysis that accounted for the transformation effects occurring under the tip during loading and the variation of elastic modulus resulting from the compositional gradient. The recovery mechanisms of the graded films are compared with homogeneous films using a new nanoscale technique. An AFM integrated with a heating and cooling stage was used to observe the recovery of inelastic deformation caused through nanoindentation. The graded films exhibited a two-way SME with a reduced hysteresis, while the homogeneous films exhibited the classical one-way SME. The fabrication and characterization techniques developed in this work have the potential to be applied to general graded and multi-layer film systems.

FABRICATION AND CHARACTERIZATION OF COMPOSITIONALLY-  
GRADED SHAPE MEMORY ALLOY FILMS

by

Daniel Paul Cole

Dissertation submitted to the Faculty of the Graduate School of the  
University of Maryland, College Park, in partial fulfillment  
of the requirements for the degree of  
Doctor of Philosophy  
2009

Advisory Committee:

Dr. H. Bruck, Associate Professor of Mechanical Engineering, Chair

Dr. A. Baz, Professor of Mechanical Engineering

Dr. T. Li, Assistant Professor of Mechanical Engineering

Dr. A. Roytburd, Professor of Materials Science and Engineering

Dr. S. Solares, Assistant Professor of Mechanical Engineering

© Copyright by  
Daniel Paul Cole  
2009

# Dedication

To my parents, Patty and Andy

## Acknowledgements

I would first like to thank my family for their love and support throughout my entire academic career. Their constant encouragement and dedication to my success has made this effort possible.

I would like to express my sincere thanks to my research advisor, Dr. Hugh Bruck, for his guidance through my time at the University of Maryland. I am indebted to him for his support, which has help shape me on a both a professional and personal level. My sincere thanks also go to Dr. Alec Roytburd for his many useful discussions on shape memory materials. I wish to acknowledge Dr. Amr Baz, Dr. Teng Li and Dr. Santiago Solares for serving on my Ph.D. committee. I would also like to acknowledge Dr. Miao Yu for allowing me access to her lab for the film processing.

I am grateful for Dr. Huiqing Jin and Dr. Wei-Yang Lu at Sandia National Labs for giving me the opportunity to work with them in their research group. I would like to thank my great colleagues, Arun, Alan, Jon, Bernard and the rest of the Functionally Graded Materials Lab for their many valuable discussions and their help with my research.

I thank my housemates, Kyle, Jamie, Brendan and Nick for being such great friends throughout graduate school.

I would also like to thank my girlfriend, Therese, for all of her love and support. I am truly lucky to have found such a great inspiration in my life.

# Table of Contents

DEDICATION .....	II
ACKNOWLEDGEMENTS .....	III
TABLE OF CONTENTS .....	IV
LIST OF TABLES.....	VI
LIST OF FIGURES .....	VII
LIST OF ACRONYMS .....	XI
<b>1. INTRODUCTION.....</b>	<b>1</b>
1.1. BACKGROUND .....	1
1.2. MOTIVATION FOR RESEARCH.....	1
1.3. DISSERTATION OUTLINE .....	5
<b>2. LITERATURE REVIEW .....</b>	<b>6</b>
2.1. SHAPE MEMORY ALLOYS.....	6
2.1.1. <i>Shape Memory Effect in SMAs</i> .....	6
2.1.2. <i>SMAs in the Form of Thin Films</i> .....	9
2.1.3. <i>Characterizing Shape Memory Effect in Thin Films</i> .....	13
2.1.4. <i>Characterizing Shape Memory Alloys using Nanoindentation</i> .....	15
2.2. NANOINDENTATION .....	19
2.3. FUNCTIONALLY GRADED MATERIALS .....	29
2.3.1. <i>Indirect Characterization of Gradients in Materials: Point Loading</i> .....	31
2.3.2. <i>Direct Characterization of Gradients in Thin Films: Auger Electron Spectroscopy</i> 33	
<b>3. EXPERIMENTAL METHODS .....</b>	<b>39</b>
3.1. GRADED SHAPE MEMORY ALLOY THIN FILM PREPARATION .....	39
3.1.1. <i>Sputter Deposition Setup</i> .....	39
3.1.2. <i>NiTi films on NiTi Ribbon Substrates</i> .....	45
3.1.3. <i>Bilayer NiTi films on Single Crystal Si Substrate</i> .....	46
3.2. DIRECT SMA FILM CHARACTERIZATION.....	47
3.2.1. <i>Scanning Probe Microscopy for Microstructural Analysis</i> .....	47
3.2.2. <i>Nanoindentation SPM on Surface Modified NiTi Substrates</i> .....	48
3.2.3. <i>Atomic Force Microscopy</i> .....	49
3.2.4. <i>Depth Profiling using Auger Electron Spectroscopy</i> .....	50
3.2.5. <i>X-ray diffraction for Crystal Structure Analysis</i> .....	52
3.2.5.1 XRD of NiTi film on NiTi Substrate.....	53
3.3. INDIRECT SMA FILM CHARACTERIZATION.....	55
3.3.1. <i>Nanoindentation for Nanomechanical Property Analysis</i> .....	55
3.3.2. <i>Nanoindentation of NiTi film on NiTi Substrate</i> .....	56
3.3.3. <i>Nanoindentation of NiTi Bilayer Films on Si Substrates</i> .....	58
3.4. NANOSCALE CHARACTERIZATION OF SHAPE MEMORY EFFECT .....	59
3.4.1. <i>A Posteriori Recovery of Nanoindenters after Heating</i> .....	59
3.4.2. <i>In situ Recovery Analysis using AFM and Heating Stage</i> .....	60
<b>4. RESULTS AND DISCUSSION .....</b>	<b>63</b>
4.1. DIRECT CHARACTERIZATION OF GRADED SMA FILMS .....	63
4.1.1. <i>Scanning Probe Characterization of Grain Structure</i> .....	63
4.1.1.1 Atomic Force Microscopy of Film Microstructure.....	64

4.1.2.	<i>Depth Profiling of Graded Films using AES</i> .....	69
4.1.3.	<i>XRD Characterization of Crystal Structure</i> .....	74
4.2.	INDIRECT CHARACTERIZATION OF SMA FILMS USING NANOINDENTATION .....	77
4.2.1.	<i>Nanoindentation of Homogeneous SMA Films on Si Substrates</i> .....	77
4.2.2.	<i>Nanoindentation of Graded SMA Films on NiTi Substrates</i> .....	79
4.2.3.	<i>Characterization of Graded Interface of Modified NiTi Substrate</i> .....	82
4.3.	MODELING OF NANOINDENTATION RESPONSE IN GRADED SMA FILMS .....	88
4.3.1.	<i>Determining the Extent of the Composition Gradient due to Diffusion Modification</i> 88	
4.3.2.	<i>Predicting the Nanoindentation Response on Graded Films</i> .....	90
4.4.	CHARACTERIZING RECOVERY OF DEFORMATION IN SMA FILMS .....	98
4.4.1.	<i>A posteriori Nanoindentation SPM characterization of recovery after heating: Characterizing one-way SME</i> .....	98
4.4.2.	<i>AFM with In Situ Heating: Characterizing Two-Way SME</i> .....	102
4.4.2.1	Calibration of New <i>in situ</i> Technique using Gold Films.....	103
4.4.2.2	Applying <i>in situ</i> Technique to Active Films .....	104
4.4.2.3	Studying SME in Individual Nanoindents .....	107
<b>5.</b>	<b>CONCLUSIONS</b> .....	<b>112</b>
5.1.	SCIENTIFIC AND TECHNICAL CONTRIBUTIONS.....	112
5.1.1.	<i>Method for Processing Compositionally-Graded SMA Films with Intrinsic Two- Way SME using Diffusion Modification</i> .....	112
5.1.2.	<i>Using Nanoindentation to Characterize Extent of Graded Interface in Graded Films</i> 112	
5.1.3.	<i>Analyzing the Nanoindentation Response on Actively-Transforming and Graded Films</i> 113	
5.1.4.	<i>Developing a Nanoscale Technique for Characterizing Recovery of Inelastic Deformation in SMA films</i> .....	113
5.1.5.	<i>Applying in situ Recovery Technique to Characterize Graded Films: Two-way SME and Reduced Hysteresis</i> .....	114
5.2.	FUTURE WORK.....	114
5.2.1.	<i>Optimize Performance of SMA Films</i> .....	115
5.2.2.	<i>Characterize Mechanical Properties of Films Further into Graded Region</i> .....	116
5.2.3.	<i>Indent SMA Films with Spherical Probe for Recovery Tests</i> .....	117
5.2.4.	<i>Implement Graded Film into MEMS Device</i> .....	118
	<b>APPENDIX</b> .....	<b>119</b>
	<b>REFERENCES</b> .....	<b>120</b>



## List of Tables

Table 1. List of specimens fabricated and tested in this research effort. A list of specimens not characterized in this work can be found in the Appendix. (AES = Auger electron spectroscopy, AFM = atomic force microscopy, NI = nanoindentation, XRD = x-ray diffraction, REC = recovery of inelastic deformation test).....	45
Table 2. This table is a list of specimens made that were fabricated but not tested in this research effort. However, the samples have been retained in case a need to characterize them arises in the future. ....	119

## List of Figures

Figure 2-1. Solid-state phase transformation that occurs in SMAs. The effect can be seen through applied mechanical or thermal loading [51].	7
Figure 2-2. Typical hysteresis loop of a SMA showing the transformation temperatures, hysteresis, and recovered stress [52].	8
Figure 2-3. Series of bright-field TEM images showing the isothermal crystallization of NiTi [46].	12
Figure 2-4. Optical micrograph of martensitic transformation that occurs in a NiTi thin film [46].	12
Figure 2-5. Surface of a SMA within a single crystal in the (a) high temperature austenite phase and (b) low temperature martensite phase [42].	14
Figure 2-6. Zone scheme proposed by Shaw et al.: First with radius <i>cp</i> deforms plastically, second zone with radius <i>cmr</i> deforms through martensitic rearrangement, outer zone deforms elastically [34].	16
Figure 2-7. Loading curve showing the isothermal austenite-martensite transformation in a NiTi film [63].	18
Figure 2-8. Transducer assembly in Hysitron's nanoindentation system [65].	20
Figure 2-9. Typical loading curve for an elastic-plastic material [30].	20
Figure 2-10. Schematic of the indentation with Berkovich tip and subsequent deformation of the sample surface [30].	22
Figure 2-11. Determination of contact depth proposed by Oliver and Pharr [30].	23
Figure 2-12. Hardness (a) and elastic modulus (b) of 500 nm Al film on different substrate [37].	26
Figure 2-13. Schematic of the Berkovich tip penetrating into a film on substrate. The parameter corrects for the fact that the tip is not a flat punch [37].	28
Figure 2-14. Elastic modulus of 500 nm Al film on different substrates using modified reduced modulus formula proposed by saha et al. [37].	28
Figure 2-15. Variation of elastic modulus with respect to depth according to a simple power law [80].	32
Figure 2-16. AES profile of a graded NiTi film [44].	35
Figure 2-17. SEM image of the cross-section of a NiTi wire used for biomedical applications [85].	37
Figure 2-18. Depth profile of a NiTi wire taken using Auger Electron Spectroscopy [85].	37
Figure 3-1. Experimental setup of the DC magnetron sputtering chamber. The chamber contains a dual, opposing gun setup with the substrate holder positioned directly between the two guns.	40
Figure 3-2. Schematic of substrate holder in DC magnetron sputtering setup. The cover contains a window that exposes a rectangular area of the substrate.	40
Figure 3-3. Schematic of annealing setup. A cylindrical resistive heater is positioned in the center of the substrate holder. A thermocouple resting between the holder and cover monitors the substrate temperature.	41
Figure 3-4. Substrate temperature as a function of time as recorded by a thermocouple fixed between the holder and cover.	41
Figure 3-5. Power radiated from the substrate holder. Note that the power levels off at approximately 105 W.	42
Figure 3-6. Schematic of Ni <sub>47</sub> Ti <sub>53</sub> film on Ni <sub>56</sub> Ti <sub>44</sub> ribbon substrate before and after annealing.	46
Figure 3-7. Schematic of the bilayer NiTi films deposited on Si substrates. The two films were of dissimilar composition.	47
Figure 3-8. Schematic of scanning probe microscopy. A probe of some finite size is brought into "contact" with the sample and dragged around the surface [86].	48
Figure 3-9. Scanning probe microscope images of a Ni <sub>47</sub> Ti <sub>53</sub> film on a polished Ni <sub>56</sub> Ti <sub>44</sub> substrate before (left) and after (right) heat treatment.	49
Figure 3-10. Optical image of the AFM probe in contact with a buckled chromium film on polymer substrate.	50

Figure 3-11. AES depth profile of a 200 Ni <sub>47</sub> Ti <sub>53</sub> film on a Ni <sub>56</sub> Ti <sub>44</sub> substrate as deposited (horizontal lines denote 56 at. % Ni (large blue dash) and 44 at. % Ti (small red dash)). ...	51
Figure 3-12. AES depth profile of an annealed 400 nm Ni <sub>47</sub> Ti <sub>53</sub> film on a Ni <sub>56</sub> Ti <sub>44</sub> substrate (horizontal lines denote 56 at. % Ni (large blue dash) and 44 at. % Ti (small red dash)). ...	52
Figure 3-13. XRD of Ni <sub>47</sub> Ti <sub>53</sub> film on Si and Ni <sub>56</sub> Ti <sub>44</sub> substrate. Note shift in main austenite peak around 42.5 and 62 degrees.....	54
Figure 3-14. Diamond Berkovich tip with an included angle of 142 degrees [65]......	55
Figure 3-15. Load function used for indentation of surface-modified NiTi substrate. The peak load was varied from 0.1-10 mN.....	57
Figure 3-16. Typical force vs. displacement curve using the load function seen in Figure 3-15. The specimen was an annealed 400 nm Ni <sub>47</sub> Ti <sub>53</sub> film on a Ni <sub>56</sub> Ti <sub>44</sub> substrate.....	57
Figure 3-17. Loading curves for an annealed 800 nm Ni <sub>47</sub> Ti <sub>53</sub> film on a 1 μm Ni <sub>47</sub> Ti <sub>53</sub> film on a Si substrate. The uniformity of the surface allows the loading curves for each indent to line up. Loading curves for the films on the bulk NiTi substrates do not show the same uniformity due to their increased surface roughness.....	58
Figure 3-18. Optical image of microindents used as a fiducial for nanoindentation area. ....	59
Figure 3-19. (a) Experimental setup of atomic force microscope with integrated heating/cooling stage for characterization of recovery <i>in situ</i> . A close up of the highlighted area can be seen in (b). ....	61
Figure 4-1. (a) SPM image of a Ni <sub>47</sub> Ti <sub>53</sub> film on a Si substrate annealed at 525 °C for 15 minutes. Note how the grains form in self-assembled rings. (b) SPM image of a Ni <sub>47</sub> Ti <sub>53</sub> film on a Si substrate annealed at 575 °C for 40 minutes. ....	64
Figure 4-2. AFM images of a Si/1 μm Ni <sub>52</sub> Ti <sub>48</sub> /0.5 μm Ni <sub>47</sub> Ti <sub>53</sub> bilayer film taken with a damaged AFM probe. The left image (2 μm) shows oblong-shaped grains, the right image (0.5 μm) is a zoomed-in view. ....	65
Figure 4-3. 2 μm AFM image of a Au film calibration sample. ....	66
Figure 4-4. AFM images of a Si/1 μm Ni <sub>52</sub> Ti <sub>48</sub> /0.5 μm Ni <sub>47</sub> Ti <sub>53</sub> bilayer film using a new AFM probe. The left image is a 2 μm scan and the right image is a 0.5 μm zoomed-in view.....	66
Figure 4-5. AFM scan of the Ni <sub>47</sub> Ti <sub>53</sub> film on a Si substrate seen in Figure 4-1a. See Figure 4-6 for close up of highlighted area.....	68
Figure 4-6. 2 μm AFM scan of the white box in Figure 4-5. Figure 4-7 shows a close up of the highlighted area. ....	68
Figure 4-7. 0.75 μm AFM scan close up of the white box in Figure 4-6.....	69
Figure 4-8. AES depth profile of a 200 nm Ni <sub>47</sub> Ti <sub>53</sub> film on a 1600 nm Ni <sub>52</sub> Ti <sub>48</sub> film on a Si substrate as deposited (horizontal lines denote 52 at. % Ni (large blue dash) and 48 at. % Ti (small red dash)). ....	70
Figure 4-9. AES depth profile of a 200 nm Ni <sub>47</sub> Ti <sub>53</sub> film on an 800 nm Ni <sub>52</sub> Ti <sub>48</sub> film on a Si substrate after annealing (horizontal lines denote 52 at. % Ni (large blue dash) and 48 at. % Ti (small red dash)). ....	72
Figure 4-10. AES depth profile of a 500 nm Ni <sub>47</sub> Ti <sub>53</sub> film on a 1000 nm Ni <sub>52</sub> Ti <sub>48</sub> film on a Si substrate after annealing at 550 C for 2 hrs (horizontal lines denote 52 at. % Ni (large blue dash) and 48 at. % Ti (small red dash)).....	74
Figure 4-11. X-ray diffraction results of the bare Ni <sub>56</sub> Ti <sub>44</sub> substrate after the annealing process. ....	75
Figure 4-12. X-ray diffraction results of a 1600nm Ni <sub>47</sub> Ti <sub>53</sub> film on Ni <sub>56</sub> Ti <sub>44</sub> substrate before and after annealing. ....	76
Figure 4-13. Nanoindentation SPM image of a nanoindentation array on a commercial 2 μm Ni <sub>50</sub> Ti <sub>50</sub> film on a Si substrate. The relief on the surface of the films is due to the arrangement of the martensite variants. ....	78
Figure 4-14. Reduced modulus as a function of contact depth for a 2 μm Ni <sub>50</sub> Ti <sub>50</sub> film on a Si substrate. The results are compared to indentation results on a graded 400 nm Ni <sub>47</sub> Ti <sub>53</sub> film on a Ni <sub>56</sub> Ti <sub>44</sub> substrate. ....	79
Figure 4-15. SPM image of an annealed 800 nm Ni <sub>47</sub> Ti <sub>53</sub> film on a (a) polished Ni <sub>56</sub> Ti <sub>44</sub> ribbon and (b) a Si substrate. Note the presence of martensite variants and greater roughness associated with the surface of the film on the polished ribbon. ....	80

Figure 4-16. Elastic modulus as a function of contact depth for an amorphous $\text{Ni}_{47}\text{Ti}_{53}$ film on a $\text{Ni}_{56}\text{Ti}_{44}$ substrate.....	81
Figure 4-17. Elastic modulus as a function of contact depth for a $\text{Ni}_{47}\text{Ti}_{53}$ film on a $\text{Ni}_{56}\text{Ti}_{44}$ substrate that was annealed at 575 C for 40 minutes. ....	82
Figure 4-18. Elastic modulus as a function of normalized contact depth for (a) amorphous films as deposited, and (b) crystallized films after annealing. $h^*$ is the normalized contact depth given in Equation 9. Note that the self-similarity breaks for the 800 nm and 1600 nm annealed films. $h^* < 1$ corresponds to contact depths less than the film thickness. Trends in the data are indicated by dotted lines. ....	84
Figure 4-19. Hardness as a function of normalized contact depth for (a) amorphous films as deposited, and (b) crystallized films after annealing. $h^*$ is the normalized contact depth given in Equation 9. Note that the self-similarity breaks for the 800 nm and 1600 nm annealed films. $h^* < 1$ corresponds to contact depths less than the film thickness. Trends in the data are indicated by dotted lines. ....	85
Figure 4-20. Schematic of graded annealed film (a) less than 500 nm and (b) greater than 500nm. Note the presence of a third homogeneous layer in (b) that results from an annealing time insufficient for diffusing species to reach the surface of the film.....	87
Figure 4-21. Schematic of diffusion interface in graded film as a result of the annealing process. ....	89
Figure 4-22. Elastic modulus as a function of indentation depth after normalizing each film thickness using the modified self-similarity formula in Equation 16. ....	90
Figure 4-23. Schematic of the indentation of a graded and actively transforming film. ....	91
Figure 4-24. Schematic of the multilayer Cu-Ni film, which consisted of alternating 50 nm layers deposited onto a Si substrate. ....	92
Figure 4-25. Results of indentation test on a multilayer Cu-Ni film on Si substrate. The film consisted of 10 alternating 50 nm layers of Cu and Ni. The plot also includes the initial elastic distribution and the predicted indentation response.....	94
Figure 4-26. Initial distribution of martensite in the film as a result of the composition gradient..	96
Figure 4-27. Corresponding expected elastic modulus in film as a result of composition gradient. ....	96
Figure 4-28. Reduced modulus variation with respect to indentation depth determined using the modified Saha/Nix equation and the initial properties determined from the martensite volume fraction in Figure 4-26. ....	97
Figure 4-29. SPM image of an annealed 1 $\mu\text{m}$ $\text{Ni}_{47}\text{Ti}_{53}$ film on a Si (100) substrate taken using the nanoindenter. A height profile of the image was taken across the deepest portion of the indent. ....	98
Figure 4-30. Height profile taken from a SPM image of an annealed 1 $\mu\text{m}$ $\text{Ni}_{47}\text{Ti}_{53}$ film on a Si (100) substrate after various heat treatments.....	99
Figure 4-31. Recovery of initial deformation as a function of heat treatment temperature for an annealed 1 $\mu\text{m}$ $\text{Ni}_{47}\text{Ti}_{53}$ film on Si (100) substrate. The final recovery was found to be approximately 35%. ....	100
Figure 4-32. AFM scan of indent array in Au film. The scan area is 25 $\mu\text{m}$ by 25 $\mu\text{m}$ . ....	103
Figure 4-33. Recovery as a function of indent depth in a gold film for the temperature range tested for the active materials. ....	104
Figure 4-34. AFM scans of a homogeneous NiTi film in the low-temperature martensite state (left) and high-temperature austenite state (right). ....	105
Figure 4-35. AFM scans of a graded 400 nm $\text{Ni}_{47}\text{Ti}_{53}$ film on a $\text{Ni}_{56}\text{Ti}_{44}$ substrate at 300 K (left) and 350 K (right). ....	106
Figure 4-36. Maximum recovery of nanoindents observed in homogeneous film (filled) and graded film (unfilled). Data are fit to linear trends to indicate the recovery's dependence on depth. ....	106
Figure 4-37. Recovery as a function of temperature for a 100 nm indent in a 2 $\mu\text{m}$ commercial homogeneous $\text{Ni}_{50}\text{Ti}_{50}$ film on a Si substrate.....	108
Figure 4-38. Recovery as a function of temperature for a 70 nm indent in a 2 $\mu\text{m}$ commercial homogeneous $\text{Ni}_{50}\text{Ti}_{50}$ film on a Si substrate.....	108

Figure 4-39. Recovery as a function of temperature for a 100 nm indent in a graded 400 nm $\text{Ni}_{47}\text{Ti}_{53}$ film on a $\text{Ni}_{56}\text{Ti}_{44}$ substrate. ....	110
Figure 4-40. Recovery as a function of temperature for a 70 nm indent in a graded 400 nm $\text{Ni}_{47}\text{Ti}_{53}$ film on a $\text{Ni}_{56}\text{Ti}_{44}$ substrate. ....	110

## List of Acronyms

**AES:** Auger electron spectroscopy

**AFM:** Atomic force microscope (or atomic force microscopy)

**CTE:** Coefficient of thermal expansion

**DSC:** Differential scanning calorimetry

**FGM:** Functionally graded material

**ISE:** Indentation size effect

**MEMS:** Microelectromechanical system

**OFHC:** Oxygen-free high conductivity

**SMA:** Shape memory alloy

**SME:** Shape memory effect

**SPM:** Scanning probe microscopy

**XRD:** X-ray diffraction

# **1. Introduction**

## **1.1. Background**

Shape Memory Alloys (SMAs) have the unique ability to recover inelastic deformation upon being heated. The effect is due to a diffusionless first-order solid-solid martensitic transformation which consists of a low temperature martensite phase (monoclinic) and a high temperature austenite phase (cubic) [1-5]. In the form of thin films, SMAs are being developed for a variety of microelectromechanical systems (MEMS) applications. Nickel-titanium (NiTi) SMAs are popular because of their excellent mechanical properties and biocompatibility [6-11]. They have been used to fabricate actuation devices such as micropumps, microvalves and microgrippers [12].

## **1.2. Motivation for Research**

Controlling the transformation of SMA films is currently achieved by changing the composition and microstructure of a single homogeneous layer [13-16]. Most devices that implement SMA films as actuators only permit repeatable actuation behavior by applying a biasing force to a homogeneous film [17]. Our focus is to control the transformation characteristics of the films through gradient architecture. Functionally grading the composition across the film thickness produces a membrane with a gradual variation in transformation temperature that exhibits a two-way shape memory effect (SME) as-fabricated [18-21]. In this work, we demonstrate a new method for fabricating graded SMAs by modifying

the surface of a nickel-rich NiTi substrate with titanium-rich NiTi monolayers or depositing bilayer NiTi films with dissimilar compositions. Annealing these systems allows the ability to naturally control the compositional gradients and their associated nanocrystalline microstructure across the film-substrate or film-film interfaces.

The ability to accurately characterize the mechanical (i.e., hardness and elastic modulus) and transformation properties (i.e., recovery of inelastic deformation and transformation temperatures) of SMA films is important for their eventual design and implementation into micro-sized devices. Indentation has become a common tool to non-destructively characterize the mechanical properties of thin films [22-29]. Nanoindentation provides a means for determining film properties with nanometer resolution with respect to depth. The commonly used Oliver and Pharr method determines the hardness and elastic modulus of a specimen using a calibrated indenter tip area function [30]. More recently, there has been interest in studying the shape memory effect in thin films using nanoindentation [31-34].

When indentation is applied to a graded SMA film, it poses several challenges. Firstly, obtaining meaningful data through the indentation of a general film system can be difficult because substrate effects and indentation size effects (ISE) will complicate the measurement [35-38]. To minimize substrate effects, it is common practice to restrict indentations to 10% of the film thickness [39]. Beyond this point the measured properties are typically a combined response from the film and substrate. However, the methods for



determining the mechanical properties of films from indentation load-displacement curves were developed assuming the film is a homogeneous material. By definition, a functionally graded material will have properties that vary with respect to some spatial location. The indentation response at a given depth will thus be a function of the deformed material as well as the surrounding area. In addition, we have the added complication of measuring the properties of an active material. The application of a mechanical load can thus induce a phase change which will in turn affect the hardness and stiffness of the material. One focus of this work is the characterization of compositional gradients from the indentation response of graded SMA thin films.

Traditional methods for characterizing transformation properties of materials (i.e., differential scanning calorimetry) are best suited for bulk materials and the tests are generally destructive. Several studies have been dedicated to characterizing transformation temperatures at the microscale, but only for a homogeneous material [40-43]. The transformation temperatures will vary throughout the thickness of a compositionally-graded film which complicates this measurement. In this work, a new nanoscale technique was developed for characterizing the recovery of the inelastic deformation in compositionally-graded SMA films. Nanoindents of varying depth were placed in the films and the subsequent recovery was monitored using AFM with an *in situ* heating/cooling stage.

In summary, this research effort addresses three main challenges. The first challenge is to fabricate a compositionally-graded SMA thin film that

possesses an intrinsic two-way SME. Previous attempts have focused on varying the deposition conditions [18, 19, 44], but no attempts have been made to exploit the natural gradients that result from diffusion across the interface of two materials with dissimilar composition. This diffusion modification technique will be utilized in this research effort.

The second challenge is the ability to characterize the composition, crystal structure and mechanical properties of a graded and actively-transforming thin film. Nanoindentation has become a popular tool to characterize materials on the nanoscale, but the complexity of the measurement has limited its use to testing mostly homogeneous materials. This work focuses on understanding the nanoindentation response on a graded and active structure, while also using other techniques such as scanning probe microscopy (SPM), x-ray diffraction (XRD), and Auger electron spectroscopy (AES) to supplement the film characterization.

The last main challenge is characterizing the transformation properties of SMA films. Conventional techniques, such as differential scanning calorimetry (DSC), are destructive tests that are best suited for bulk materials. A few methods have been proposed to test the transformation properties of films at the microscale [40, 42, 43], but they are incapable of characterizing a graded structure, where the transformation temperature varies throughout the thickness of the film. In this work, a new nanoscale technique is developed to characterize transformations in graded SMA films using an AFM with *in situ* heating and cooling to study the recovery of deformations induced through nanoindentation.

### 1.3. Dissertation Outline

The methods used to address the research objectives mentioned above will be discussed in the following chapters. Chapter 2 reviews the basics of the SME, the processing and characterization of SMA films, as well as the techniques involved in characterizing functionally graded materials (FGMs). An effort is made to present the state of the art in each area, while pointing out the scientific and technical limitations of each topic and what this work does to address them. Chapter 3 details the experimental processes involved in fabricating the compositionally-graded SMA films in this work, as well as the experimental methods utilized to characterize their microstructure, crystal structure, composition, mechanical properties and recovery mechanisms. Chapter 4 describes the results of the characterization process, which includes methods developed to predict the extent of the graded interface, an analysis of the indentation response on actively-transforming SMA films, as well as an *in situ* nanoscale technique to characterize the recovery of inelastic deformation in SMA films. Finally, Chapter 5 discusses the scientific and technical contributions of this effort and the possible directions for future work.

## 2. Literature Review

### 2.1. Shape Memory Alloys

#### 2.1.1. Shape Memory Effect in SMAs

The shape memory effect (SME) was first discovered in a gold-cadmium alloy in 1953 [8]. A decade later, Buehler and coworkers at the Naval Ordnance Laboratory discovered the effect in a nickel-titanium alloy [6]. The material was nicknamed Nitinol (**NiTi Naval Ordnance Laboratory**) and it has become the most widely-used shape memory material. The effect is also observed in other alloys such as CuAlZn, CuAlNi, and CuSn. NiTi has become popular because of its high functionality as an engineering material. It is corrosion resistant, it has low thermal conductivity, high resistivity and good fatigue resistance [45]. NiTi is also capable of recovering strains of approximately 10% [18], with recovery stresses approaching 400 MPa [40]. They have been used in bulk form as valves, fasteners and stents [46]. The SME in NiTi is due to a solid-state phase transformation between a low temperature martensite phase and a high temperature austenite phase. The austenite phase has been described as a high-symmetry cubic CsCl (B2) type structure [47, 48]. The martensite phase is a distorted monoclinic structure with lower symmetry; the martensite crystal “variants” can thus be arranged in different orientations [49, 50].

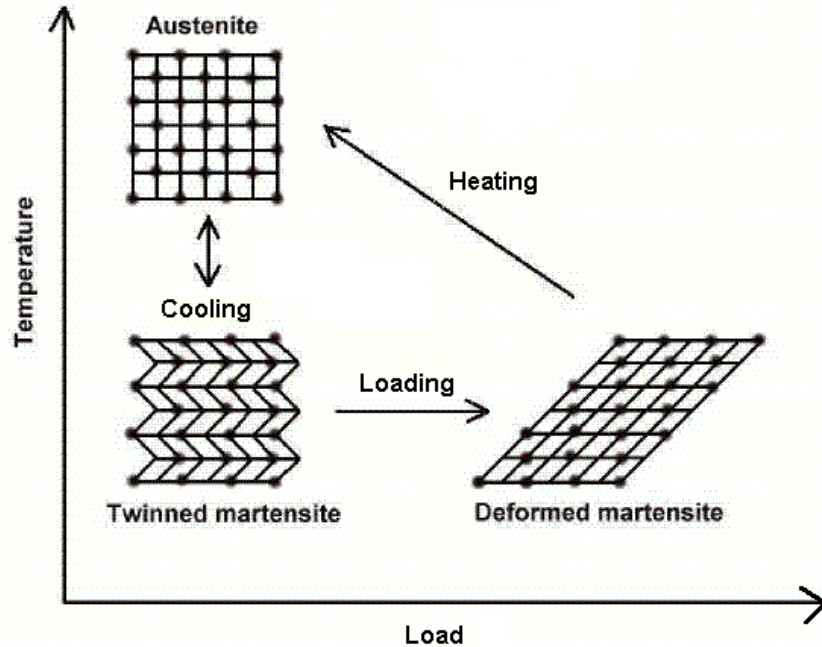


**Figure 2-1.** Solid-state phase transformation that occurs in SMAs. The effect can be seen through applied mechanical or thermal loading [51].

The martensite phase is capable of rearranging its atomic lattice structure through a coordinated shear-like distortion (see Figure 2-1). This allows the material to accommodate relatively large amounts of inelastic deformation. A stress applied to a material in the martensitic phase will produce a strain that can be recovered with subsequent load removal; this is known as pseudoelasticity. Deformation can also be recovered through the application of heat and subsequent cooling. As seen in Figure 2-1, the deformed martensite phase transforms to the high temperature austenite phase through heating and then returns to the undeformed or “twinned” martensite phase upon cooling.

SMAs are often characterized by a phase transformation hysteresis loop, like the one shown in Figure 2-2. Starting from the low temperature martensite phase, the material is heated and begins transforming at  $A_s$ , the austenite start temperature. At this point, martensite is still the prevalent phase. However, as

the temperature is increased, more and more of the martensite transforms to austenite. At  $A_f$ , the material has completely transformed to the high temperature austenite phase. When the material is cooled from the austenite phase, the material begins transforming to martensite at  $M_s$ . Note that  $M_s$  is not equal to  $A_s$ . As the material is cooled further, the low temperature phase begins to dominate, until it has completely transformed to martensite at  $M_f$ . The hysteresis associated with the transformation curves is typically defined as the temperature difference between  $A_f$  and  $M_s$  or the difference between  $A_s$  and  $M_f$ . Most NiTi films display a hysteresis of at least 30 °C, which has limited their potential as microactuators, where high frequency transformations are desirable [12].

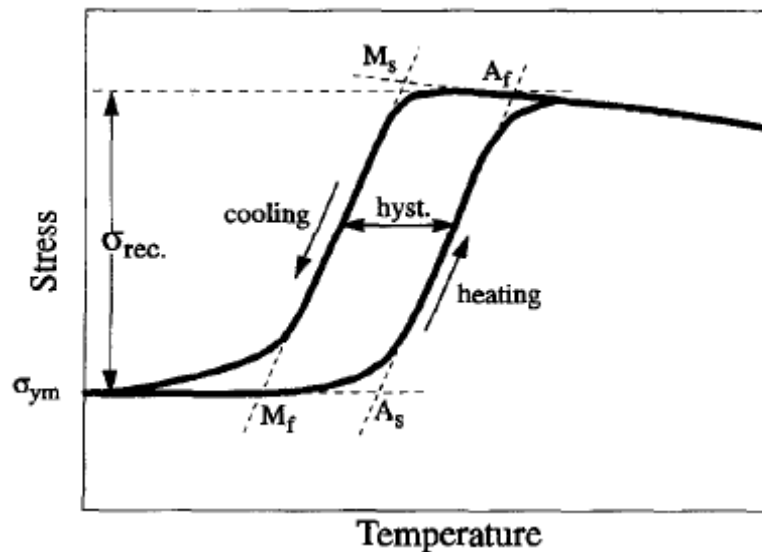


**Figure 2-2.** Typical hysteresis loop of a SMA showing the transformation temperatures, hysteresis, and recovered stress [52].

The two-way SME in SMAs is typically created in homogeneous films through a training process. Wibowo et al. produced this effect in a homogeneous near-equiatomic NiTi film by over-straining the sample in the martensite phase, beyond the limit of complete shape memory recovery, and then releasing the

load [53]. The sample was then heated above the austenite finish temperature, where it did not recover its original shape as a result of the excessive strain induced in the low temperature state. The sample was cooled below the martensite finish temperature and over-deformed once again. After this process was repeated several times, the film would exhibit two different shapes when in the high-temperature and low-temperature states.

Therefore, the two-way SME can be produced in homogeneous SMA materials, but only through a complicated training process. As the size scale of the materials decreases, the training process becomes even more difficult. The focus of this research effort is to produce a compositionally-graded film that exhibits the two-way SME as fabricated. This is achieved by varying the composition, and thus the transformation temperatures, throughout the thickness of the film. This creates internal stress in the film naturally and eliminates the need for any training.

### **2.1.2. SMAs in the Form of Thin Films**

The SME has also been demonstrated in thin films, making them attractive candidates for actuation devices in microelectromechanical systems (MEMS). With respect to microscale actuation, SMAs possess the highest known actuation force compared to other actuation modes, such as electrostatic, thermal and piezoelectric [46]. SMA films can be electrically driven using joule heating; their high surface-to-volume ratio produces high cooling rates which is ideal for a high frequency response. The NiTi system has been particularly popular for film

actuation schemes because of the relatively high work per density it can produce during recovery ( $\sim 10^7$  J/m<sup>3</sup>) [34].

NiTi films are typically deposited using sputtering techniques [32, 54-56]. The basic sputtering process consists of a bulk target (e.g. NiTi) and an opposing substrate (typically silicon or glass) positioned in an evacuated chamber [8]. A non-reactive gas, such as Argon, is pumped into the chamber, where it is then ionized. An electric field accelerates the Argon ions into the target. Atoms are then ejected from the target and deposited onto the substrate. The strength of the electric field, the gas pressure and the distance separating the target and substrate all control the rate of deposition.

The SME is very sensitive to small changes in stoichiometry, which has restricted their reliability and manufacturability in MEMS devices. The NiTi system is particularly sensitive to composition; small deviations from the equiatomic region can drastically alter the transformation temperatures. Schell et al. report that a deviation of 0.2 atomic percent from the equiatomic configuration can change the transition temperature by 25 K [16]. Unfortunately, when depositing NiTi films using sputtering techniques, the yield is often Ni-rich with respect to the original target material, making it difficult to control the final composition. Otsuka attributes this to the oxidation of Ti that occurs during the sputtering process. To compensate for the depletion of Ti, a Ti mesh can be placed over the NiTi target in order to produce films that better reflect the target material composition [53]. Although the Ti yield will be greater in this case, it has been difficult to precisely control the final composition of the sputtered film. Cho



et al. proposed a technique for precisely controlling the composition of NiTi films through a multilayer technique [57]. Instead of working with an alloy target, the authors sputtered alternating layers, tens of nanometers thick, of pure Ni and pure Ti onto a Si substrate. Subsequent heating allowed interdiffusion between the layers, producing a final film that was assumed to be homogeneous. The final stoichiometry was determined by controlling the relative thicknesses of the pure layers.

The final microstructure of an SMA film will control its ability to recover deformation. NiTi films sputter-deposited at room temperature are generally amorphous. The films must be heated above 400 °C to initiate crystallization, although the crystallization process is sensitive to the film stoichiometry. Wang et al. report that the crystallization temperature and crystallization activation energy both decrease with an increase in Ti concentration [58]. They performed a study of the crystal nucleation rate and growth velocity for near-equiatom NiTi films using the combination of high precision heating and microscopic tracking of individual crystals. During the heating process, the surface relief was observed optically as light was scattered off the crystallite boundaries. Ramirez et al. also observed the evolution of microstructure in near equiatom NiTi films using a *in situ* transmission electron microscope (TEM) heating technique [46]. The crystals were found to grow in circular shapes, while their interiors consisted of filament shaped subgrains (see Figure 2-3). The subgrains grew outwardly and radially like pine needles, their arrangement consistent with a spherulitic structure which is a sign of isotropic and rapid crystal growth. These microstructures are

often observed in polymorphic crystallization, where the composition remains the same and only the structure changes

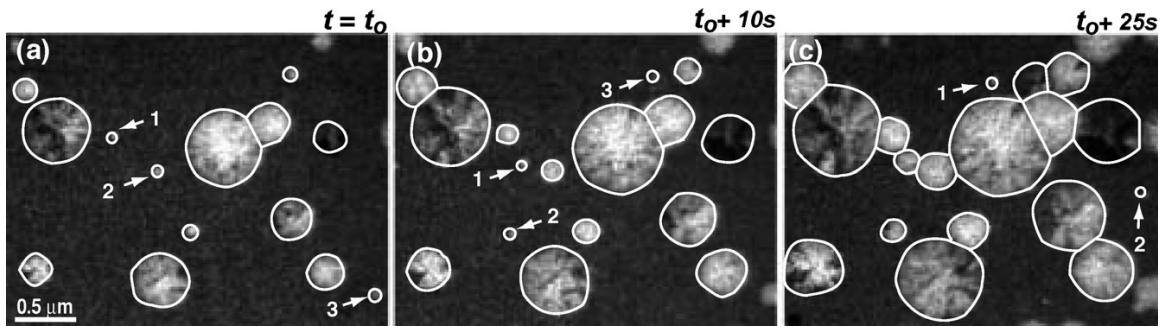


**Figure 2-3.** Series of bright-field TEM images showing the isothermal crystallization of NiTi [46].

Ramirez and coworkers were also able to observe the austenite-martensite transformation through an in-situ heating and cooling experiment (see Figure 2-4). The grain marked with an “A” is in the high temperature austenite phase. Upon cooling, the grain develops alternating dark and bright lines that indicate a twinned martensitic structure. The austenitic structure returns as the temperature is raised back above the transformation point.

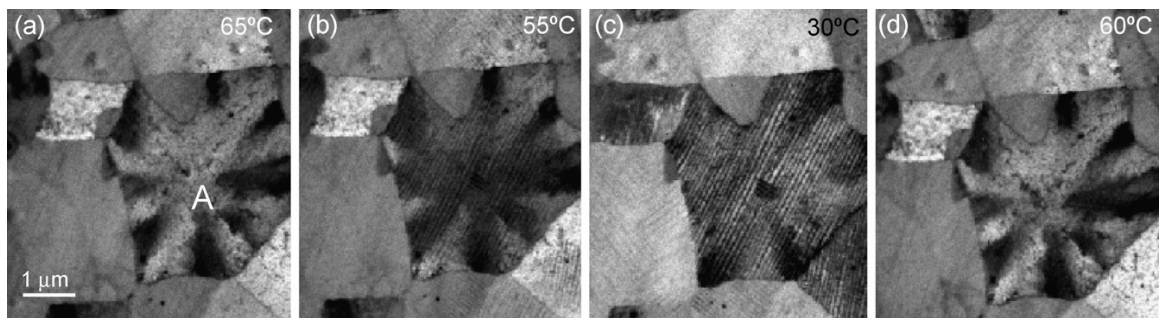


**Figure 2-4.** Optical micrograph of martensitic transformation that occurs in a NiTi thin film [46].

More recently, the SME has been observed on the nanoscale. Interestingly, these phase changes are seen in nature by the bacteriophage T4 virus, which has an outer tail sheath comprised of a protein crystal that undergoes a martensitic transformation. The lattice of the protein contracts

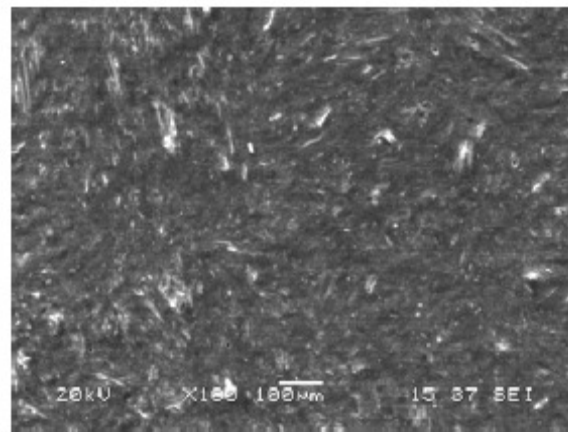
uniaxially via atomic rearrangement which provides the force necessary to drive the inner tail tube through a cell membrane of a host cell, allowing its foreign DNA to be transmitted [59].

To date, the majority of the research on SMA films has been focused on depositing homogeneous materials of a specific composition in order to achieve the maximum recovery at a certain transformation temperature. The focus of this work is to design and characterize a compositionally-graded film, one in which the transformation temperature varies throughout the thickness of the film.

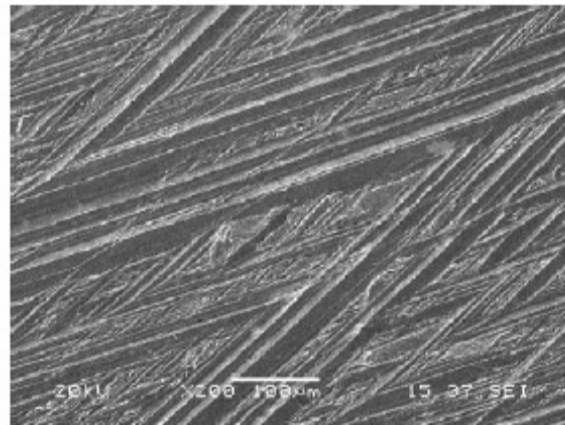
### **2.1.3. Characterizing Shape Memory Effect in Thin Films**

Recently, SMA films have gained attention as potential micro-actuators, such as microvalves and micropositioners. Accurately characterizing and controlling the transformation temperatures is critical for these devices. Traditional techniques, such as differential scanning calorimetry (DSC) (requires a few milligrams) and substrate curvature methods (typically requires a standard wafer, a few inches in size), are designed for bulk materials. He et al. observed the martensitic transformation in shape memory alloy films using an atomic force microscope with an *in situ* heating stage [42]. The purpose of their investigation was to develop methods for characterizing the transformation temperatures in thin films. They showed the transformation occur by observing the change in surface roughness associated with the martensitic transformation. In the absence of an external load, the phase transformation results in no apparent macroscopic change in the material's shape, although He et al. show that there is a microscopic change in the surface relief. The surface is relatively flat in the

high temperature austenite phase, while it becomes relatively rough in the low temperature martensite phase due to the twinned variants causing the surface relief. Figure 2-5 shows the surface relief within a SMA single crystal in the austenite and martensite phases.



(a) Austenite



(b) Twinned martensite

**Figure 2-5.** Surface of a SMA within a single crystal in the (a) high temperature austenite phase and (b) low temperature martensite phase [42].

Boterill et al. developed an approach that allows the transformation temperature in micron-sized areas of material to be accurately characterized [40]. The transformation temperatures can also be measured by monitoring the variation in electrical resistance of the material as the phase is changed. Johnson estimated the transformation temperature of a NiTi film by observing a

20-30% increase in the resistance as the sample was cooled [41, 43]. The spike in resistance was attributed to the formation of the intermediate rhombohedral (R) phase that can develop between the austenite and martensite phase. However, the electrical resistance method can be inconvenient for very small samples. He and coworkers found that their *in situ* technique was nondestructive and capable of characterizing the transformation temperatures in relatively small volumes of material. However, the above techniques are insufficient for measuring the transformation of a graded film, where the transition point varies throughout the thickness of the film. Therefore, in this work we will be pursuing new techniques for characterizing the transformation behavior of compositionally-graded SMA films.

#### **2.1.4. Characterizing Shape Memory Alloys using Nanoindentation**

Nanoindentation is a commonly used technique for characterizing mechanical properties of films because measurements can be made at nanometer depths into films that are sub-micron in thickness. The SME in thin films has also been studied recently using nanoindentation. Recovery of nanoscale deformation in NiTi thin films was first observed by Shaw et al. [34]. The films were indented in their low-temperature martensite state. After heating the films above the austenite finish temperature and subsequent cooling back to the martensite phase, the indents were scanned using atomic force microscopy (AFM) to detect the amount of recovered deformation. The authors found that smaller indents, less than 100 nm deep, recovered a much higher percentage of the initial deformation. They attribute this effect to the bluntness of the Berkovich

tip, which had a radius of curvature of approximately 100 nm. For indents less than 100 nm the indentation is more spherical in nature and thus has experienced less non-reversible plastic deformation. Conversely, indents greater than 100 nm are more pyramidal in nature as the sharpness of the Berkovich geometry dominates and the bluntness of the tip is less of a factor. This results in a very high stress region under the tip that experiences much more plastic deformation and results in less of a SME. The authors propose a simple zone model scheme (see Figure 2-6) that accounts for three different modes of deformation: a plastic zone of radius  $cpl$ , a martensitic rearrangement zone of radius  $cmr$ , and finally an elastic zone at a radius greater than  $cmr$ .

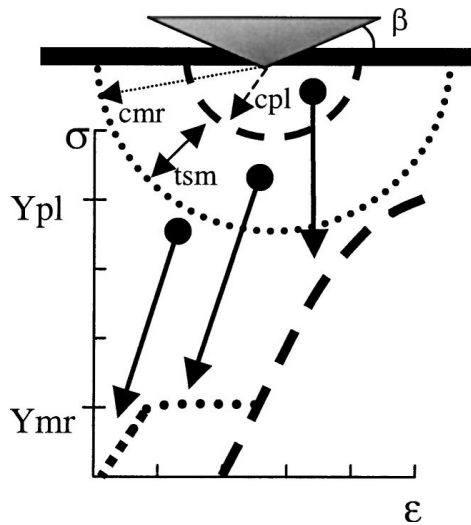


**Figure 2-6.** Zone scheme proposed by Shaw et al.: First with radius  $cpl$  deforms plastically, second zone with radius  $cmr$  deforms through martensitic rearrangement, outer zone deforms elastically [34].

The model assumes that the initial stage of the indentation is accommodated by elastic deformation, as the contact is spherical and thus the stress is more spread out. As the indentation depth increases, martensitic twin rearrangement is induced. Further indentation causes irreversible plastic

deformation. The authors estimate the radius of the hemisphere  $c$  that separates the different zones using an expression from the well-known contact mechanics book by K.L. Johnson [60]:

$$c = \frac{d}{\tan \beta} \left( \frac{E \tan \beta}{6Y[1-\nu]} + \frac{2-4\nu}{3-3\nu} \right)^{\frac{1}{3}} \quad 1$$

where  $\beta$  is the angle between the surface and indenter,  $E$  is young's modulus,  $Y$  is the yield stress,  $\nu$  is Poisson's ratio and  $d$  is the depth of indentation. Shaw et al. use equation 1 twice, once using  $Y$  as the yield stress that would occur through martensitic rearrangement and a different  $Y$  that would occur due to plastic deformation. The difference in these two radii was used to approximate the thickness of the shell of the martensitic zone  $tsm$ , the distance between the inner plastic and outer elastic zones.

This model assumes that the low-temperature state of the film is single-crystal martensite. However, most NiTi films fabricated via sputtering and post-deposition heat treatment are polycrystalline, consisting of both martensite and austenite phases [61]. Austenite has an elastic modulus that is approximately three times the elastic modulus of martensite [2, 62]; thus a polycrystalline material will have a more complicated behavior.

The SME can also occur at the nanoscale via a mechanical stress induced transformation [63]. Ma and coworkers displayed the isothermal austenite-martensite transformation by nanoindenting a NiTi film in the austenite phase (see Figure 2-7).

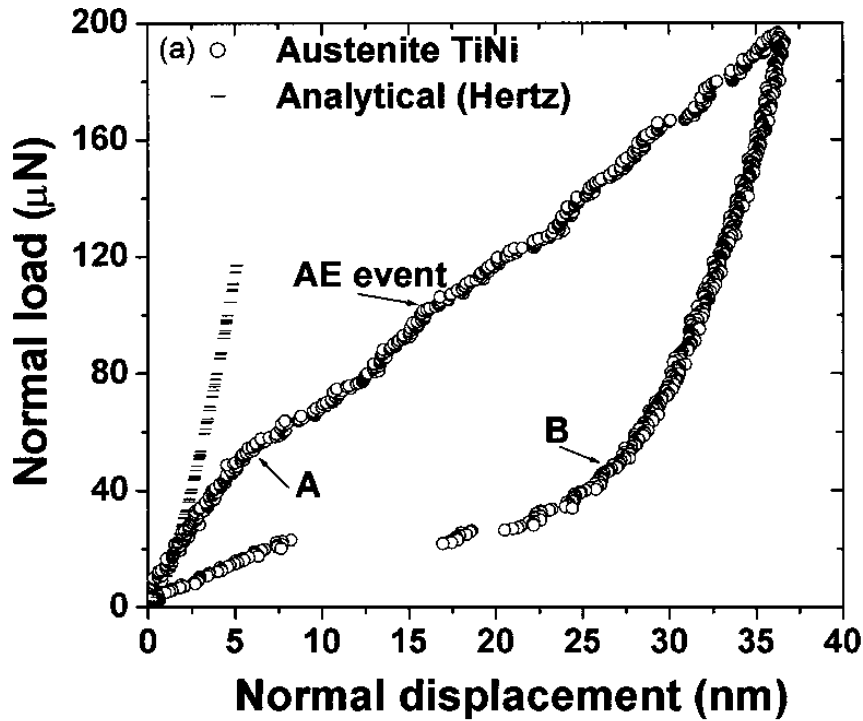


**Figure 2-7.** Loading curve showing the isothermal austenite-martensite transformation in a NiTi film [63].

As the load is increased, a critical stress is reached, denoted by point A, which causes the austenite unit cell to distort. This leads to the nucleation of the monoclinic martensite unit cells. The inherent twinning behavior and lower elastic modulus of martensite causes the slope of the loading curve to decrease. The initial portion of the unloading curve is dominated by the elastic unloading of the stress-induced martensite under the tip and the untransformed austenite outside the high stress region. As the unloading continues, another critical stress is reached, denoted by point B, which leads to the reverse transformation. The stress-induced martensite switches back to the austenite phase which is at a lower free energy. This pseudoelastic response leaves no residual impression on the surface of the film. Ma et al. note that this effect is only observed with the relatively large tips, with radii of 685 nm and 15 mm. The pseudoelastic



response was not seen using 115 nm and 240 nm tips, presumably because of the added plastic deformation that causes dislocations and not solid-state phase transformations.

Nanoindentation was used in this work to measure mechanical properties on the nanoscale as well as to induce nanoindentations into the materials to observe recovery phenomena. Other researchers have used nanoindentation on homogeneous SMAs, but never on a graded SMA. This effort is the first attempt to extract properties from a graded and active structure using nanoindentation.

## **2.2. Nanoindentation**

Nanoindentation is a popular method for determining the mechanical properties of thin films due to its ability to control indentation depth on the nanoscale. It is becoming a common method for measuring the elastic modulus and hardness of small volumes of material due to its ease of use. There are minimal sample preparation requirements, specimens can be tested several times, and different volumes of material can be examined through the appropriate choice of loading conditions and tip geometries [64]. However, the indentation response is a complicated one and must be well understood in order to extract credible results.

Nanoindentation has been possible through the development of instruments that are able to continuously measure the force and displacement during indentation. In addition, the resolution of measured force and displacement of nanoindentation systems is on the order of nanonewtons and nanometers, respectively. Figure 2-8 is a schematic of the transducer assembly

in Hysitron's Triboindentation system [65]. The transducer consists of three parallel capacitor plates; the top and bottom plate are held fixed, while the middle plate, to which the probe is connected, is held by leaf springs and is allowed to move in the vertical directions. By manipulating the voltages on each capacitor plates, the position of the tip can be precisely controlled.

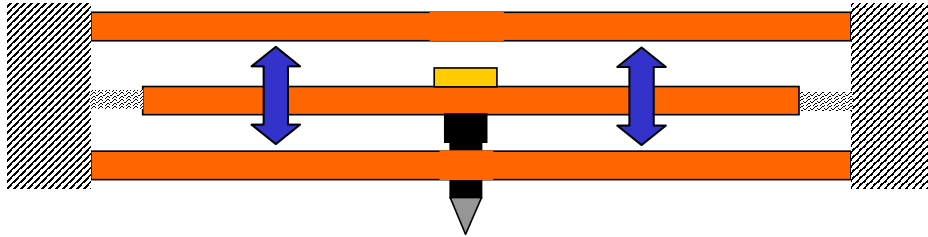


**Figure 2-8.** Transducer assembly in Hysitron's nanoindentation system [65].

In nanoindentation, a probe of known geometry is forced into a specimen, and the initial response of the material is measured as the load is removed (see Figure 2-9). The three-sided Berkovich geometry is the most popular tip for indenting bulk materials and films thicker than 100 nm.

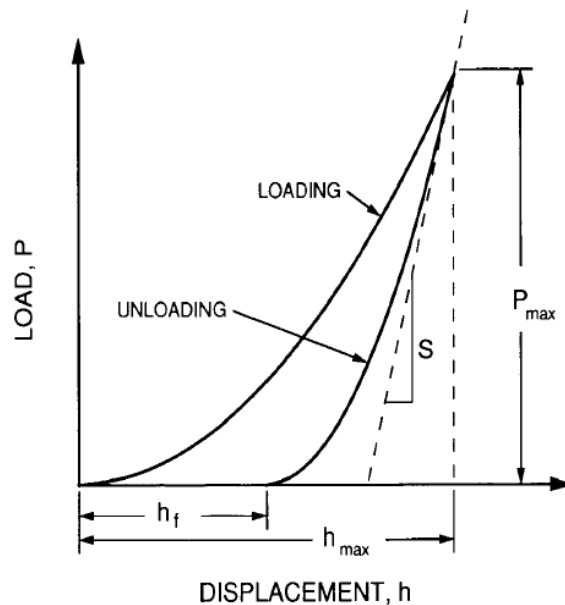


**Figure 2-9.** Typical loading curve for an elastic-plastic material [30].

The analysis of these measurements is often credited to the works of Oliver and Pharr [30]. They showed that the unloading data is well described by a simple power law relation

$$P = A(h - h_f)^m \quad 2$$

where  $P$  is the applied load,  $A$  is the contact area,  $h$  is the displacement into the material,  $h_f$  is the final depth of the indent and  $m$  is a constant [66, 67]. The value of the exponent  $m$  varies based on the geometry of the probe;  $m = 1$  for a flat cylinder,  $m = 2$  for a cone, and  $m = 1.5$  for paraboloids of revolution. The measured stiffness  $S$  of the material is found by differentiating the above expression at the beginning stage of unloading according to:

$$S = \frac{dP}{dh} = 2E_r \sqrt{\frac{A}{\pi}} \quad 3$$

where  $E_r$  is the reduced modulus. The reduced modulus accounts for the fact that the indenter itself is not completely rigid, but also mechanically deforms to some extent during the indentation process. The elastic modulus of the specimen  $E_s$  is related to the measured reduced modulus through the following expression:

$$\frac{1}{E_r} = \frac{1 - \nu_i^2}{E_i} + \frac{1 - \nu_s^2}{E_s} \quad 4$$

Here,  $E_i$  and  $\nu_i$  are the elastic modulus and Poisson's ratio of the indenter, respectively, and  $\nu_s$  is the Poisson's ratio of the specimen. The indenter is typically a very stiff material, such as diamond; in this case, the specimen's elastic modulus is very close to the measured reduced modulus. The true elastic

modulus of the specimen can be found by rearranging equations 3 and 4, provided the contact area is known. The hardness  $H$  of the material is a relatively straightforward calculation:

$$H = \frac{P_{max}}{A} \quad 5$$

where  $P_{max}$  is the peak indentation load and  $A$  is the projected contact area of the hardness impression.

The main difference between conventional indentation and nanoindentation is the use of a tip area function. The latter can produce indents that range from 0.1-1.0  $\mu\text{m}$  deep, making the contact area difficult to define. In this case, a tip area function can be used to relate the depth of penetration to the area of contact of a tip of known geometry. During the loading process, the total displacement  $h$  is a combination of the vertical distance along which contact is made  $h_c$  and the displacement of the surface at the contact perimeter  $h_s$  (see Figure 2-10).

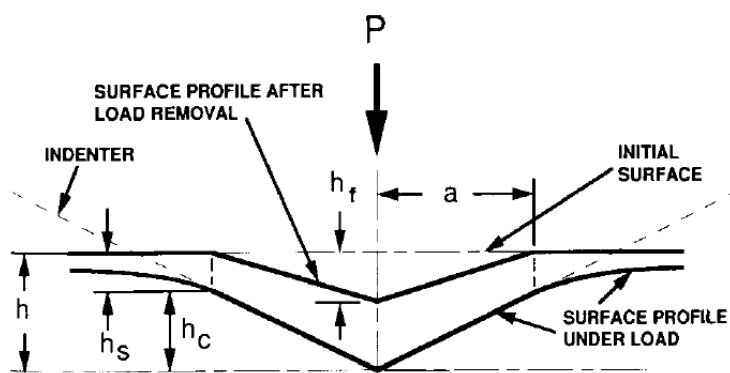


**Figure 2-10.** Schematic of the indentation with Berkovich tip and subsequent deformation of the sample surface [30].

The standard model of the indentation process takes into account the deformation that can occur with the surrounding material not directly in contact with the indenter. Oliver and Pharr showed that this deformation is also dependent on the geometry of the tip through the following relation:

$$h_c = h_{\max} - \varepsilon \cdot \frac{P_{\max}}{S} \quad 6$$

Here,  $\varepsilon$  is a constant that is dependent on the shape of the indenter;  $\varepsilon = 1$  for a flat punch, while  $\varepsilon = 0.75$  for a paraboloid of revolution. This effectively reduces the area of contact between tip and specimen (see Figure 2-11).

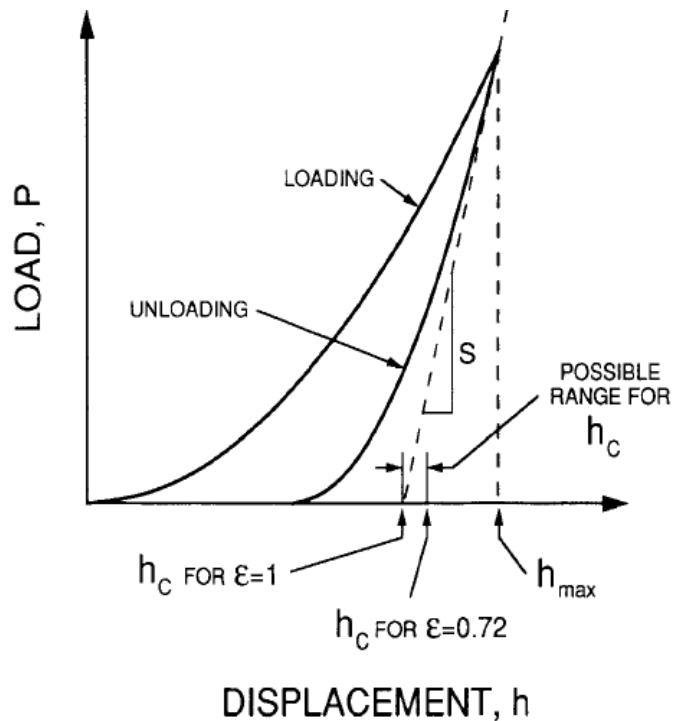


**Figure 2-11.** Determination of contact depth proposed by Oliver and Pharr [30].

The theory discussed up until now does not account for the imperfections in tip geometry that must be considered when indenting at the nanoscale. For a

tip with idealized geometry (i.e., perfect cone, perfect sphere, perfect pyramid), the projected contact area  $A$  to depth  $h_c$  relationship is given by

$$A = C_o h_c^2 \quad 7$$

where  $C_o$  is a constant that depends on the shape of the tip. A perfect Berkovich tip is described by  $C_o = 24.5$ , although real tips are never manufactured with this ideal geometry. To find the actual contact area as a function of contact depth, the tip is calibrated by indenting a homogeneous material with well known mechanical properties, such as quartz. Rearranging equation 3 and assuming mechanical properties for the reference sample, the contact area can be found at several selected contact depths. The data are fit to a sixth order polynomial of the form:

$$A = C_0 h_c^2 + C_1 h_c + C_2 h_c^{1/2} + C_3 h_c^{1/4} + C_4 h_c^{1/8} + C_5 h_c^{1/16} \quad 8$$

where  $C_1$ - $C_5$  are constants that are fit in order to describe each unique tip.

Once the contact area-contact depth relationship has been established, the function is saved in the instrument's software for subsequent indentations on a specimen of unknown mechanical properties. Depending on the relative hardness of tip and specimen, the area function will need to be recalibrated from time to time to account for tip blunting.

Extracting mechanical properties from a material using nanoindentation presents several challenges. When indenting thin films, the measured response is a complex function of the elastic and plastic properties of both the film and substrate. However, the standard Oliver-Pharr method for measuring material properties from the load-displacement data was developed assuming

homogeneous materials. To correctly measure a specimen's hardness and elastic modulus, an accurate determination of the contact area is required. When indenting a soft film on a relatively hard substrate, the specimen will tend to "pile up" along the sides of the indenter. This will cause the contact area to be underestimated and thus the hardness will tend to be overestimated. On the other hand, when indenting a hard film on a relatively soft substrate, the specimen will tend to "sink in." The contact area will be overestimated, causing an underestimate of the hardness. The elastic modulus measurement has the added complication of long range stress fields. To extract properties of just the film, it is common practice to restrict the indentation depth to less than 10% of the film thickness.

Saha et al. developed a method for decoupling the indentation response of the film with that of the substrate [37]. They studied the effects of soft films on hard substrates and then hard films on soft substrates. Figure 2-12 displays the indentation data for 500 nm thick aluminum films on sapphire, silicon, glass and aluminum substrates. The data are plotted against a normalized contact depth

$$h^* = \frac{h_c}{t} \quad 9$$

where  $h_c$  is the indentation depth  $t$  is the thickness of the film.

The measured hardness of  $h^* < 1$ , contact depths less than the thickness of the film, is approximately constant and close to the hardness of bulk aluminum. As the indentation depth approaches the film/substrate interface the data begin to deviate according to the hardness of each substrate. The harder

sapphire and silicon substrates even begin to affect the measurement at indentation depths less than the thickness of the film.

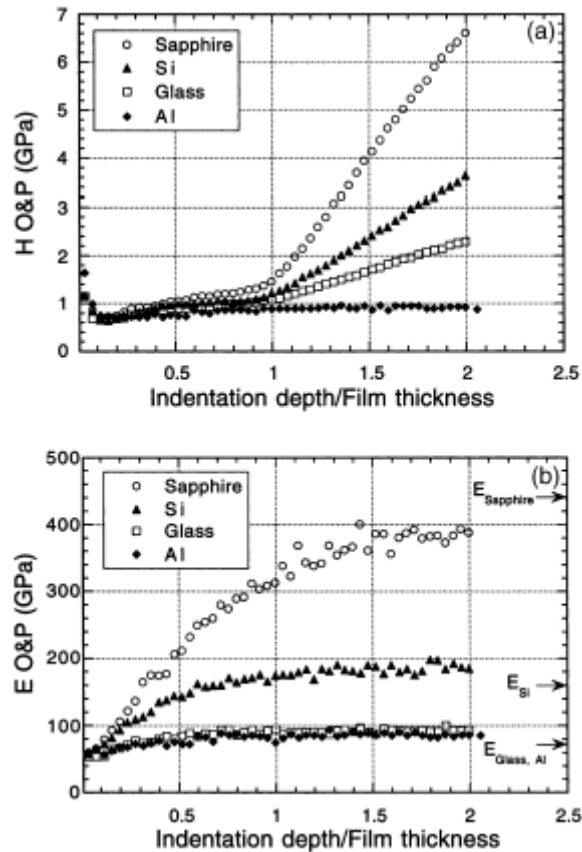


**Figure 2-12.** Hardness (a) and elastic modulus (b) of 500 nm Al film on different substrate [37].

Figure 2-12a also shows the characteristic “indentation size effect” (ISE) where for very small indents, the hardness decreases with respect to increasing indentation depth. This effect is seen in crystalline materials for indents of  $h/t < 0.05$  and is a result of strain gradient plasticity [36]. Figure 2-12b displays the elastic modulus as a function of normalized contact depth  $h^*$ . The measurement is almost immediately compromised by substrate effects, especially for the relatively stiff sapphire substrate. Compared to the hardness measurements, the elastic modulus measurements are more strongly affected by the substrate



because the elastic field under the tip is not confined to the film, but rather is a long range field that extends into the substrate. Clearly the method for measuring the elastic modulus needs to be adjusted to account for the mismatch in mechanical properties between the film and substrate. Equation 4, commonly used in the Oliver-Pharr method, was established for monolithic materials. This equation is only applicable to film-substrate systems if the film and substrate have similar elastic properties or if the film is sufficiently thick (indentation depth is less than 10% of film thickness).

Saha and coworkers attempted to account for the influence of the substrate by including an additional term into the reduced modulus equation. They modified the work of King [68] to account for the three-face geometry of the Berkovich tip. Their modified reduced modulus equation was used to predict the elastic response of a homogeneous, non-active film on an elastically mismatched substrate:

$$\frac{1}{E_r} = \frac{1-\nu_i^2}{E_i} + \frac{1-\nu_f^2}{E_f} \left( 1 - e^{\frac{-\alpha d}{a}} \right) + \frac{1-\nu_s^2}{E_s} \left( e^{\frac{-\alpha d}{a}} \right) \quad 10$$

Here,  $d$  is the thickness of the film below the tip,  $a$  is the square root of the projected contact area, and  $\alpha$  is a scaling parameter that is a function of  $a/d$  (see Figure 2-13). The  $(t - h)$  term is labeled ' $d$ ' in this work to avoid ambiguity. This analysis permits the measurement of the film at contact depths up  $0.5t$ , a substantial increase beyond the  $0.1t$  limit that is commonly used.

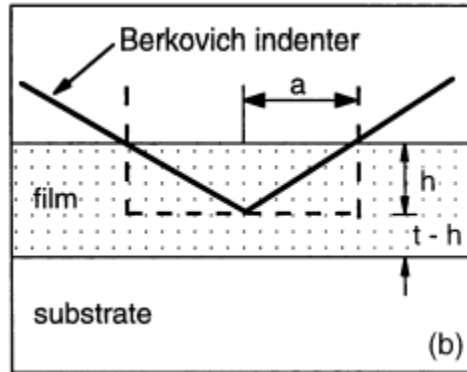


**Figure 2-13.** Schematic of the Berkovich tip penetrating into a film on substrate. The parameter  $\alpha$  corrects for the fact that the tip is not a flat punch [37].

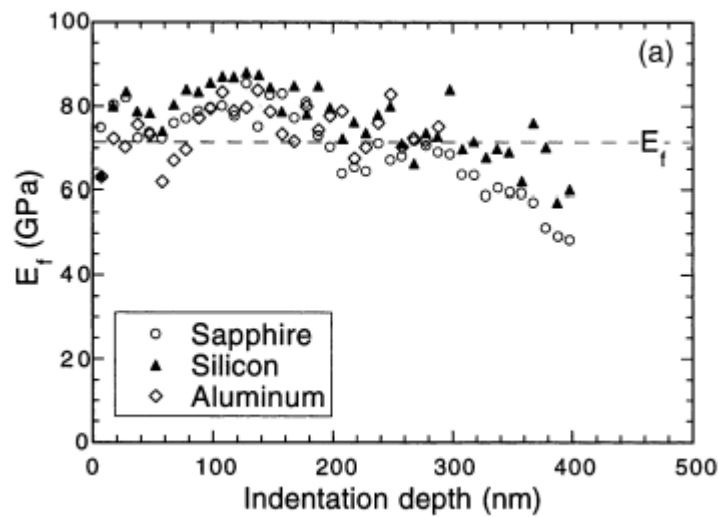


**Figure 2-14.** Elastic modulus of 500 nm Al film on different substrates using modified reduced modulus formula proposed by saha et al. [37].

Figure 2-14 shows the elastic modulus data of an aluminum film on sapphire, silicon and aluminum substrates using equation 10. The prediction describes the expected film modulus reasonably well for contact depths less than 50% of the film thickness. They attribute the deviation for the rest of the range to the fact that the King model is based on a flat punch, whereas their tests were performed with the more complex geometry associated with the Berkovich tip.

Nanoindentation is a powerful tool for extracting the hardness and elastic modulus of a sample on the nanoscale. In the case of a film, the measurement is a complex response to the properties of the film and substrate. Saha and Nix addressed this problem for the case of a non-active, homogeneous film on a non-active homogeneous substrate. However, this work is insufficient for a graded material that is capable of changing crystal structures, and thus mechanical properties, during indentation. This research effort addresses the indentation response of a film that is both graded and actively changing its property distribution.

### **2.3. Functionally Graded Materials**

A Functionally Graded Material (FGM) is a material whose properties vary with respect to some spatial location [69-75]. FGMs are being developed for a variety of electrical, optical and mechanical applications. Tian and coworkers are developing compositionally-graded Barium-Strontium-Titanate (BST) films for dielectric and optical applications [76]. BST is used in dielectric capacitors and non-volatile memory applications; they are attractive in the form of thin films because the size and weight of the devices are greatly reduced. The graded BST films contain internal stresses and polarization gradients which are shown to improve the tunability of the device.

In Freund's analysis of mismatch strain in heterogeneous thin films, he discusses epitaxial semiconductor materials designed with a continuous compositional gradient throughout the thickness of the film [77]. These graded films are designed to provide a transition in the lattice parameter from one

material to another to minimize the tendency for the formation of dislocations and other defects. Freund studied general graded film systems with elastic mismatch strains through the thickness direction which could result from thermal expansion mismatch, chemical reactions with volume or phase changes, or microstructural evolution. The internal or residual stresses associated with these compositional gradients provide the driving force for various modes of failure; therefore, methods for measuring this stress and controlling its effects are of great interest.

Kruft et al. fabricated functionally graded metal-ceramic composites that were designed for armor applications [78]. The outer surface consisted of pure alumina, a hard, thermally resistant material designed to blunt or break apart a projectile. The inner surface consisted of pure nickel, a relatively tough and ductile material designed to absorb energy. Starting from the pure alumina layer, subsequent layers contained increasing amounts of nickel. The gradual variation in relative amounts of metal and ceramic in successive layers prevented large changes in the coefficient of thermal expansion at each interface; this allowed the material to be processed virtually free of cracks.

In this work, the idea of controlling internal stress distributions via a FGM was applied to SMA films in order to produce the two-way SME as fabricated. By varying the transformation temperatures throughout the thickness of the film, it is possible to create the internal stress distribution needed to produce the effect.

### **2.3.1. Indirect Characterization of Gradients in Materials: *Point Loading***

One method for characterizing gradients in materials is through an indirect measurement. For example, in large composition gradients (milliscale to macroscale) it is possible to section specimens and measure properties associated with the composition, such as the density using pycnometry [79]. The accuracy of these methods is somewhat limited since they will require analysis and assumptions to relate properties to the composition. However, their ease of use has made them the most generally accepted approaches in the FGM community.

One particular method that enables non-destructive characterization of property gradients in materials with small composition gradients (nanoscale to microscale) is the use of point loads. Giannakopoulos and Suresh were the first to attempt characterization of mechanical properties in graded materials subjected to point loads [80]. Their work has had application in a wide range of scientific areas, for example: advanced coatings for structural components to protect against thermal and tribological damage, penetration of armor materials consisting of hard outer surfaces and tough inner surfaces by projectiles, and even geotechnical analyses for the settlement of foundations on deposits of clay, rocks and soils. The authors developed solutions to the stress and displacement fields to elastically-graded solids that were subjected to point loading. First they considered the case where the Young's modulus  $E$  varied as a function of depth according to a simple power law (see Figure 2-15):

$$E = E_0 z^k \quad \text{for } 0 < k < 1 \quad 11$$

This model has been used to describe dense clay and sand earth deposits where the stiffness at the surface is relatively low and increases continuously with respect to depth.

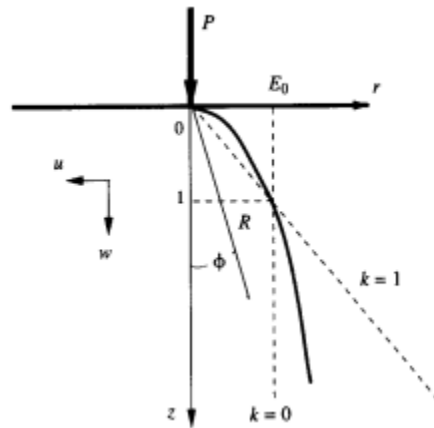


**Figure 2-15.** Variation of elastic modulus with respect to depth according to a simple power law [80].

Assuming spherical coordinates, as seen in Figure 2-15, and radial symmetry, the lone principal stress can be described as

$$\sigma_{RR} = \frac{C \cdot \cos(\phi)^{\frac{1}{\nu}-1}}{R^2} \quad 12$$

where  $C$  is a constant and  $\nu$  is Poisson's ratio which is related to the  $k$  chosen to describe the power law. The corresponding strains and displacements can then be found. An example of this case is a structural engineering material with compositionally-graded metal-ceramic layers, such as the Ni-alumina system discussed earlier. Here the variation of Young's modulus can be approximated by  $E=84.9z^{0.216}$ , with  $z$  in microns and  $E$  in GPa, with the free surface taken as the compliant pure Ni region and  $\nu$  assumed to be 0.3 throughout the composite.

While this work sufficiently describes continuously graded materials whose properties do not change during the indentation process and whose behavior is predominantly elastic, it does not predict the behavior of the continuously-graded SMA films in this work which will be both inelastic with actively-transforming crystal structures.

### **2.3.2. Direct Characterization of Gradients in Thin Films: *Auger Electron Spectroscopy***

Point loads can potentially provide indirect characterization of compositional gradients through their mechanical response; however, it is also desirable to obtain a direct measurement of the compositional gradient. In large compositional gradients (milliscale to macroscale), it is possible to section specimens from within the gradient and destructively obtain the composition through techniques such as thermogravimetric analysis [81]. However, for smaller compositional gradients (nanoscale to microscale) it is necessary to use techniques that can characterize the material at these length scales. These techniques are mostly limited to the use of conventional radiation (XRD or spectroscopy) or electrons (SEM/TEM), while even techniques like XRD provide a bulk measurement at the microscale (e.g., crystal structure of a micron-thick thin film).

Auger Electron Spectroscopy (AES) has been one of the most popular surface analytical tools to provide information on the elemental composition of the first atomic layers of a solid [82, 83]. The technique is based on the emission of low energy electrons (10-2,000 keV), known as auger electrons, from atoms

with a hole in an inner shell during a relaxation process. The hole in the inner shell is most often created using an electronic or photonic impact. An excited atom with a hole in one of its inner shells will tend to relax to reach a more energetically-favorable state. The auger process occurs when the hole in the inner shell is filled by an electron from an outer shell. The remaining energy is transferred to an electron in another outer shell, which is ejected with a kinetic energy that is characteristic of the atomic energy levels involved in the process. The kinetic energy of the released electron is dependent upon the binding energy of the electron in the particular shell of the excited atom; this information can be used to determine the chemical make-up of the atom. The intensity of the auger electron signal is used to quantify the elemental concentrations in the first few surface layers.

The AES technique has the ability to sample the first few atomic layers of a sample. When used in conjunction with a method of removing the atomic layers from the surface, depth profiling becomes possible. This application of AES is widespread in the study of thin film electronic devices, coatings and corrosion layers [84]. One popular method of peeling away surface layers is through sputtering, where ions impart their kinetic energy to surface atoms as they collide into the sample. If the imparted energy exceeds the binding energy of the targeted material, material is sputtered from the surface. This technique is also used to clean the surface of a sample by removing the layers rich in contaminants.



Martins and coworkers used AES to profile the surface of compositionally-graded SMA films [19, 44]. They fabricated graded NiTi films by deliberately varying the Ni/Ti ratio during the sputtering process. They produced films with a gradual change in composition, crystalline structures, transformation temperatures and residual stress through the film thickness. The graded films were deposited by co-sputtering from two magnetron guns, one containing a Ni<sub>49</sub>Ti<sub>51</sub> target and the other containing a Ti target. The sputtering power of the magnetron containing the NiTi target was held constant at 40 W, while the power of the magnetron holding the pure Ti target was varied from 0-30 W. With this setup, Martins et al. were able to produce equiatomic NiTi films by running the Ti target at 8 W. It should be noted that this result was the focus of their earlier study where the experimental setup was used to balance the well-known Ti-deficient yield in sputtering from a NiTi target. Figure 2-16 shows the AES depth profile of a 420 nm graded film deposited onto a Si substrate.

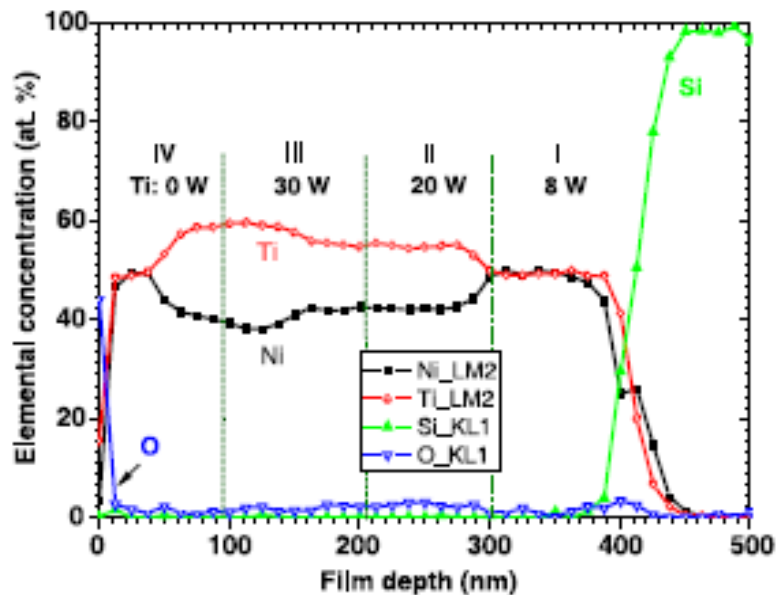


**Figure 2-16.** AES profile of a graded NiTi film [44].

The substrate is on the right of the plot and the film is grown from right to left. The first 100 nm (section I) was deposited with the Ti target run at 8 W, which produced a film near the equiatomic composition. The Ti target power was increased for sections II and III, resulting in an increase in the Ti composition. The Ti target power was turned off for the last 100 nm of the deposition, resulting in a decrease in the Ti composition. The composition gradient in the film produced a variation in the transformation temperature with respect to depth. The transformation temperature would be expected to increase from the section I to section III because of the increasing Ti concentration. The transformation temperature would be expected to decrease from the section III to section IV, as the film concentration varies from Ti-rich to equiatomic. The limitation to this technique is that in order to obtain the SME, the films must be heated above 400 °C to initiate crystallization. This will produce diffusion across the film-film interfaces, reducing the extent of the graded region.

Clarke et. al used AES depth profiling to study corrosion on the surface of NiTi wires used in the medical device industry [85]. Medical devices containing NiTi depend on a layer of titanium dioxide on the surface to prevent Ni from seeping into the body, which has known toxicological effects. Figure 2-17 shows the cross-section of the wire. The depth profiling was done from left to right on the image. The results of the profiling can be seen in Figure 2-18.

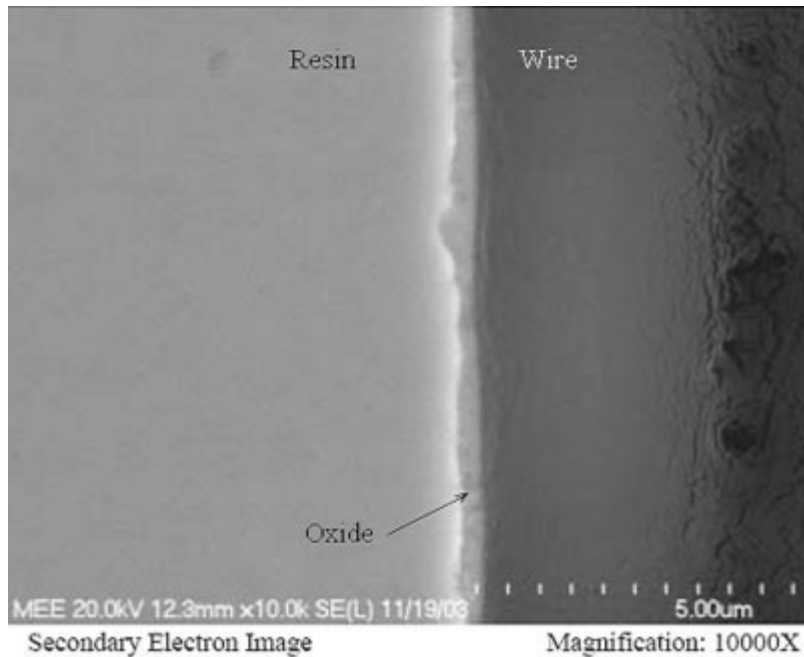


**Figure 2-17.** SEM image of the cross-section of a NiTi wire used for biomedical applications [85].

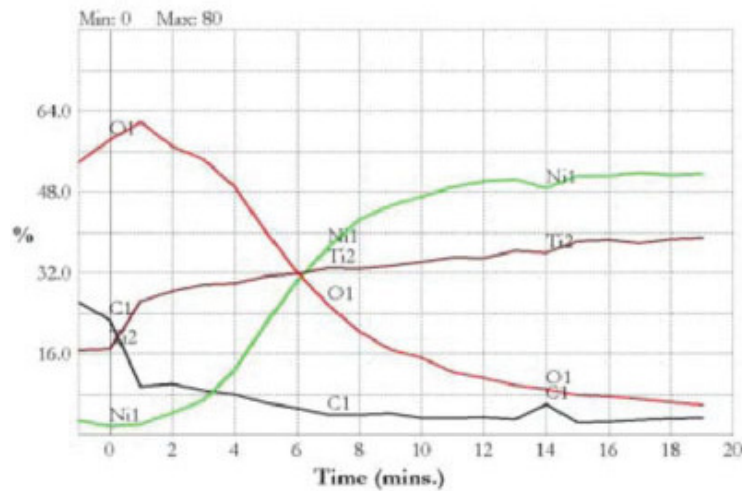


**Figure 2-18.** Depth profile of a NiTi wire taken using Auger Electron Spectroscopy [85].

The horizontal axis in Figure 2-18 highlights one of the difficulties associated with AES depth profiling. The authors chose to use time instead of distance as a reference, due to the difficulties associated with calibrating the depth profile. If a sample is composed of different chemical species with dissimilar binding energies, the species will be removed at different rates during

the sputtering process. This will introduce error into the measurement and limit the certainty of a quantitative analysis. A common approach is to assume the sputtering rate is that of a well-known material, such as silicon dioxide.

For this work, AES will be investigated as to its potential for directly determining the composition gradient in a thin film. Furthermore, the ability to detect the gradient as a function of depth will be needed to compare with the indirect approach.

## **3. Experimental Methods**

### **3.1. Graded Shape Memory Alloy Thin Film Preparation**

#### **3.1.1. Sputter Deposition Setup**

Films were prepared using the DC magnetron sputtering setup seen in Figure 3-1. The sputtering system consists of opposing guns configured in a one foot diameter cylindrical chamber. Each gun contained the desired target material to be deposited. Shields were placed in front of each gun to prevent cross-contamination from the opposing gun. The substrate holder was suspended from the top of the chamber, directly between the two guns. The substrate was secured on the face of a holder, a 6 cm x 3 cm x 1 cm block of oxygen-free high conductivity (OFHC) copper, as seen in Figure 3-2. The substrate was pinned between the block and a 0.25 cm thick plate of OFHC Cu, which was fastened to the large face of the substrate holder. A 2 cm x 1 cm rectangular hole was cut out from the center of the plate, exposing an area on the substrate of similar dimensions, while the remaining portion of the substrate was masked.

A heat treatment was generally required to crystallize the sputtered films. The specimens were heated immediately following the deposition process, before they could be exposed to air. A cylindrical heater (Watlow 100 W Firerod, St. Louis, MO) was positioned in a cavity that ran through the center of the substrate holder (see Figure 3-3). The OFHC copper was chosen as the holder material because of its good thermal conductivity. A thermocouple was placed

between the holder and cover, adjacent to the substrate, so that the temperature could be monitored.

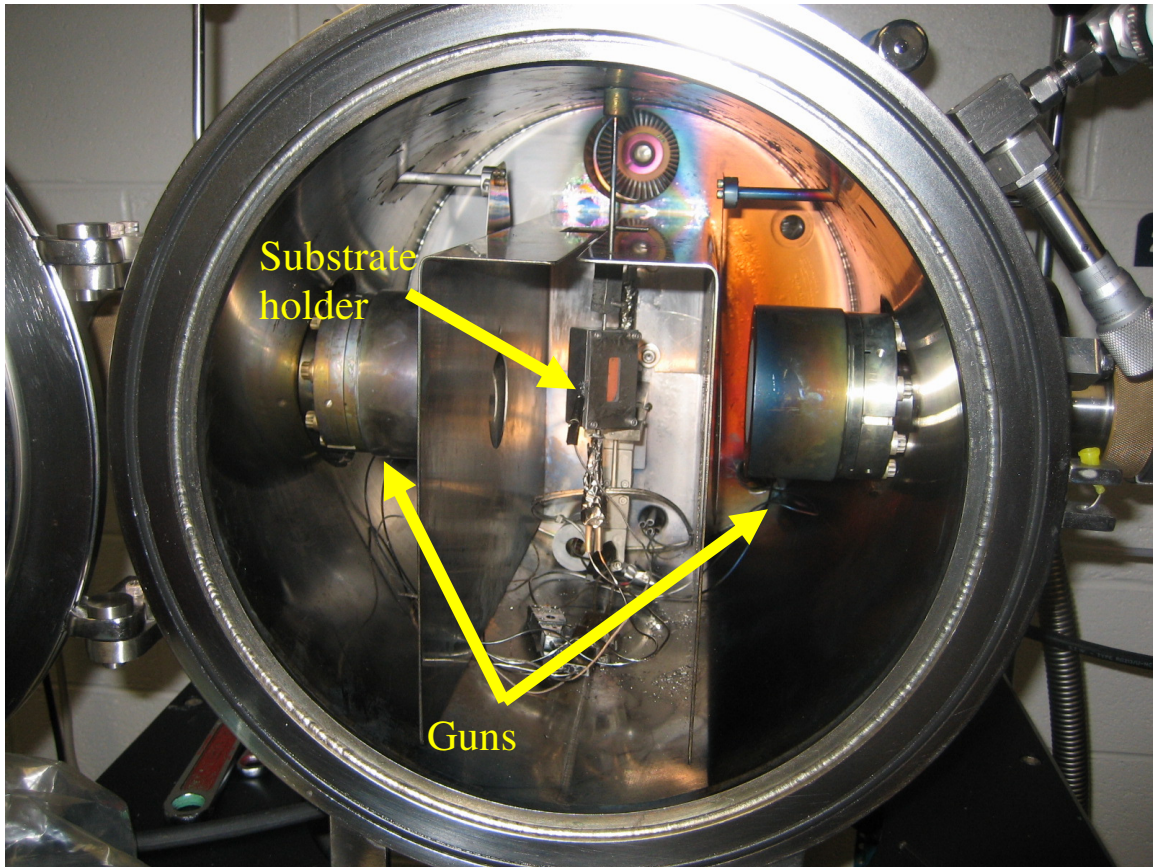


**Figure 3-1.** Experimental setup of the DC magnetron sputtering chamber. The chamber contains a dual, opposing gun setup with the substrate holder positioned directly between the two guns.

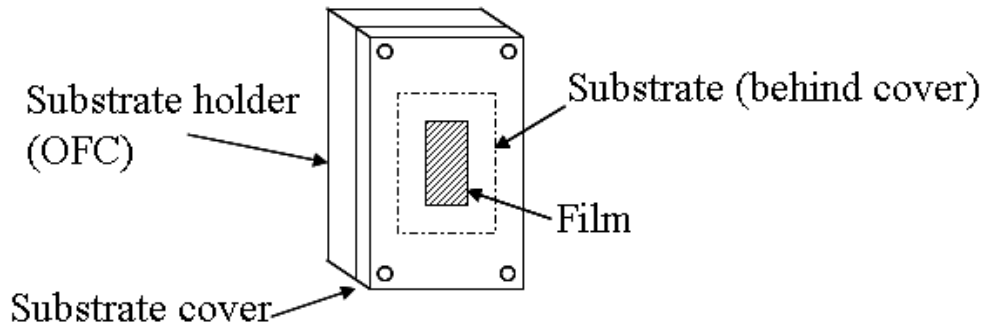


**Figure 3-2.** Schematic of substrate holder in DC magnetron sputtering setup. The cover contains a window that exposes a rectangular area of the substrate.

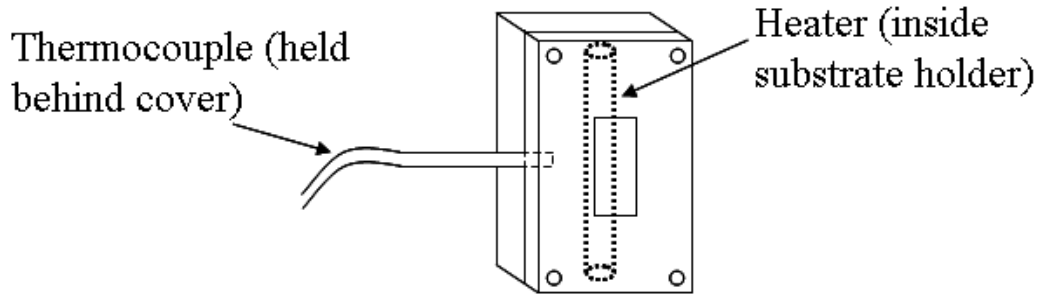


**Figure 3-3.** Schematic of annealing setup. A cylindrical resistive heater is positioned in the center of the substrate holder. A thermocouple resting between the holder and cover monitors the substrate temperature.

Radiation from the substrate holder limited the temperature of the annealing process. As discussed in the literature review, the films must be heated upwards of 500 °C in order to be crystallized. For initial experiments, the substrate was not able to reach this temperature threshold, apparently due to substrate radiation. To test the power radiated from the substrate, the temperature was monitored as a function of time. As seen in Figure 3-4, the temperature levels off around 470 °C.

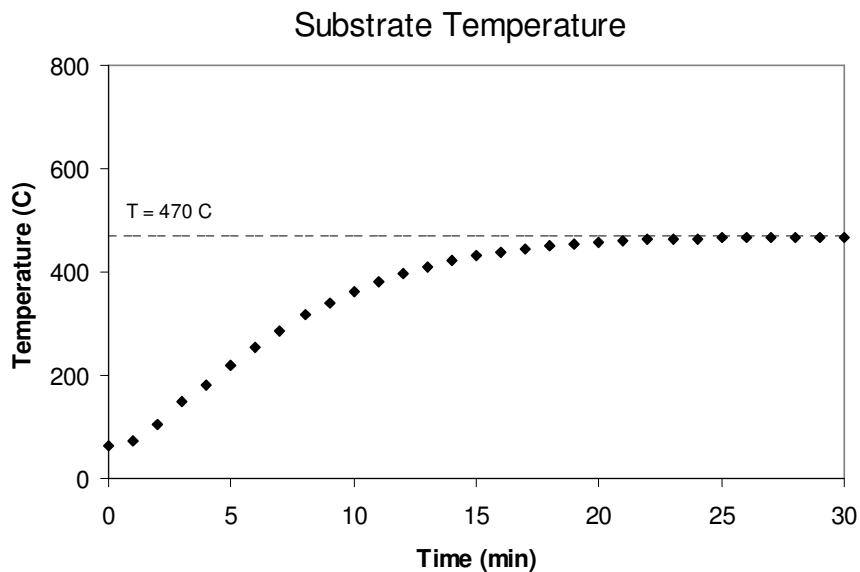


**Figure 3-4.** Substrate temperature as a function of time as recorded by a thermocouple fixed between the holder and cover.

The power  $P$  radiated by the substrate is given by the Stefan-Boltzmann Law:

$$P = \varepsilon A \sigma T^4 \quad 13$$

where  $\varepsilon$  is the emissivity,  $A$  is the surface area,  $\sigma$  is the Stefan-Boltzmann constant and  $T$  is the temperature. Based on the dimensions of the substrate and the emissivity of the surface of the substrate, the power as a function of time could be calculated (see Figure 3-5).

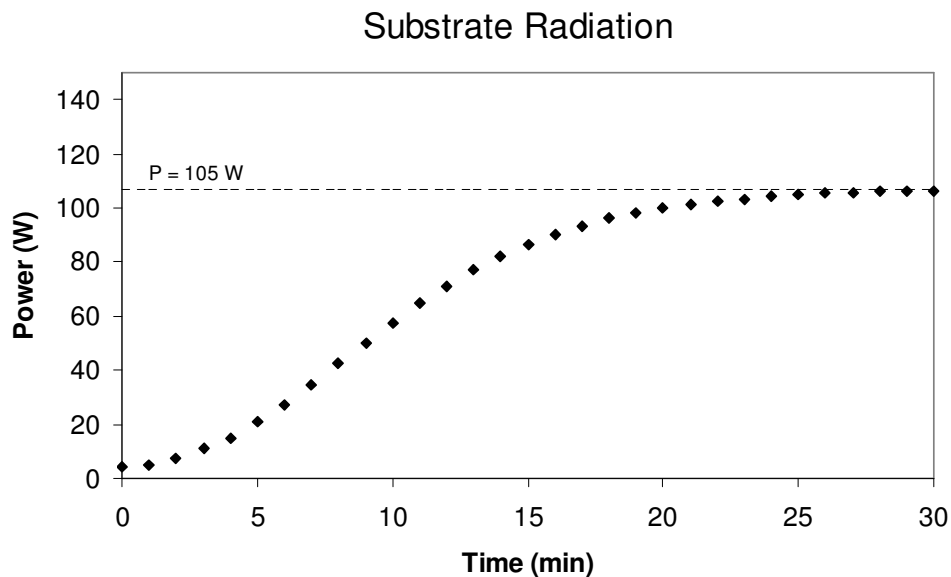


**Figure 3-5.** Power radiated from the substrate holder. Note that the power levels off at approximately 105 W.

The power appears to level off around 105 W, while the maximum power of the heater is approximately 100 W. This implies that the substrate holder is acting like an ideal black body and hotter surface temperatures would not be possible. In order to limit the radiation, the emissivity of the holder had to be reduced. The holder at the time of this experiment was covered with Ni, Ti, and NiTi films from past sputtering experiments; the films were even peeling away



from the substrate holder in several spots. This increased the surface area of the holder and also increased the emissivity constant of the surface. These problems were mitigated by mechanically polishing the substrate holder down to the original Cu surface. The polished substrate holder allowed subsequent heat treatments of 600 °C. From that point on, the substrate holder was polished after every few sputtering depositions.

Once the excessive radiation problem was solved, specimens were prepared using the following procedure. The experiment began by sealing the chamber and pumping out the air until a vacuum of approximately  $1.0 \times 10^{-6}$  Torr ( $1.3 \times 10^{-4}$  Pa) was achieved. This generally took a couple of hours depending on the seal of the main door and the seal between the chamber and the two guns. It should be noted that this pumping time can be decreased by about 50% by applying vacuum grease to each seal and baking the chamber overnight at 80 °C. Once the desired base pressure was reached, Argon (99.99%) was pumped into the chamber until reaching a pressure of 2-3 mTorr. The sputtering process was initiated by powering the gun to approximately 180 W. The targets were generally sputtered onto the shield for the first 10 minutes so that the guns could heat up and the equilibrium yield could be established. Films were deposited by removing the shield and allowing the target material to be sputtered onto the substrate. The deposition rate was varied by controlling the sputtering pressure, target power, and the distance between the gun and substrate. The deposition rate at a given set of these parameters was established by performing profilometry on a reference sample.

The following table is a list of specimens that were fabricated in this work. The table excludes the samples that were prepared but have not been characterized. A list of those samples can be found in the Appendix.

**Table I**

Date	Specimen	Heat Treatment	Tests on Sample
05.06.2006	800 nm Ni <sub>47</sub> Ti <sub>53</sub> on Si (100)	30 min @ 400 °C	NI
05.25.2006	1 μm Ni <sub>47</sub> Ti <sub>53</sub> on Si (100)	none	NI
06.06.2006	1 μm Ni <sub>47</sub> Ti <sub>53</sub> on Si (100)	30 min @ 475 °C	NI
06.19.2006	600 nm Ti on 1 μm Ni <sub>47</sub> Ti <sub>53</sub> on Si (100)	20 min @ 450 °C	AFM, NI
06.21.2006	500 nm Ti on 1 μm Ni <sub>47</sub> Ti <sub>53</sub> on Si (100)	none	AFM, NI
06.27.2006	800 nm Ni <sub>47</sub> Ti <sub>53</sub> on Si (100)	40 min @ 550 °C	NI
06.29.2006	800 nm Ni <sub>47</sub> Ti <sub>53</sub> on Si (100)	none	NI
07.06.2006	800 nm Ni <sub>47</sub> Ti <sub>53</sub> on Si (100)	15 min @ 500 °C	NI
07.14.2006	800 nm Ni <sub>47</sub> Ti <sub>53</sub> on Si (100)	20 min @ 500 °C	AFM, NI
07.17.2006	1.6 μm Ni <sub>47</sub> Ti <sub>53</sub> on Si (100)	15 min @ 525 °C	XRD, AFM, NI
07.18.2006	500 nm Ti on 1.5 μm Ni <sub>47</sub> Ti <sub>53</sub> on Si (100)	30 min @ 500 °C	NI
08.07.2006	1.5 μm Ni <sub>47</sub> Ti <sub>53</sub> on Ni <sub>56</sub> Ti <sub>44</sub> substrate	15 min @ 550 °C	XRD, NI
08.08.2006	1.5 μm Ni <sub>47</sub> Ti <sub>53</sub> on Ni <sub>56</sub> Ti <sub>44</sub> substrate	none	AFM, NI
08.11.2006	1.5 μm Ni <sub>47</sub> Ti <sub>53</sub> on Ni <sub>56</sub> Ti <sub>44</sub> substrate	10 min @ 500 °C	AFM, NI
08.15.2006	1.5 μm Ni <sub>47</sub> Ti <sub>53</sub> on Ni <sub>56</sub> Ti <sub>44</sub> substrate	15 min @ 550 °C	NI
08.17.2006	3 μm Ni <sub>47</sub> Ti <sub>53</sub> on Ni <sub>56</sub> Ti <sub>44</sub> substrate	none	NI
11.14.2006	1.5 μm Ni on Si (100)	none	NI
11.29.2006	1.5 μm Ni on Ni <sub>56</sub> Ti <sub>44</sub> substrate	none	NI
12.01.2006	1.5 μm Ni on glass substrate	none	NI
12.04.2006	1.5 μm Ni <sub>47</sub> Ti <sub>53</sub> on glass substrate	none	NI
12.20.2006	1.5 μm Ni <sub>47</sub> Ti <sub>53</sub> on Ni <sub>56</sub> Ti <sub>44</sub> substrate	none	NI
12.21.2006	1.5 μm Ni <sub>47</sub> Ti <sub>53</sub> on glass substrate	30 min @ 450 °C	XRD, NI
01.05.2007	1.5 μm Ni <sub>47</sub> Ti <sub>53</sub> on Si (100)	30 min @ 575 °C	XRD, NI
02.08.2007	200 nm Ni <sub>47</sub> Ti <sub>53</sub> on Ni <sub>56</sub> Ti <sub>44</sub> substrate	none	NI
02.12.2007	100 nm Ni <sub>47</sub> Ti <sub>53</sub> on Ni <sub>56</sub> Ti <sub>44</sub> substrate	none	AFM, NI
02.16.2007	400 nm Ni <sub>47</sub> Ti <sub>53</sub> on Ni <sub>56</sub> Ti <sub>44</sub> substrate	40 min @ 575 °C	XRD, NI, AES, REC
03.22.2007	400 nm Ni <sub>47</sub> Ti <sub>53</sub> on Ni <sub>56</sub> Ti <sub>44</sub> substrate	none	NI
03.27.2007	200 nm Ni <sub>47</sub> Ti <sub>53</sub> on Ni <sub>56</sub> Ti <sub>44</sub> substrate	none	NI
03.29.2007	200 nm Ni <sub>47</sub> Ti <sub>53</sub> on Ni <sub>56</sub> Ti <sub>44</sub> substrate	40 min @ 575 °C	NI, AES
04.06.2007	Annealed bare Ni <sub>56</sub> Ti <sub>44</sub> substrate	40 min @ 575 °C	NI
04.10.2007	800 nm Ni <sub>47</sub> Ti <sub>53</sub> on Ni <sub>56</sub> Ti <sub>44</sub> substrate	40 min @ 575 °C	AFM, NI, REC
04.12.2007	800 nm Ni <sub>47</sub> Ti <sub>53</sub> on Ni <sub>56</sub> Ti <sub>44</sub> substrate	none	NI
04.14.2007	1.6 μm Ni <sub>47</sub> Ti <sub>53</sub> on Ni <sub>56</sub> Ti <sub>44</sub> substrate	none	NI
04.20.2007	1.6 μm Ni <sub>47</sub> Ti <sub>53</sub> on Ni <sub>56</sub> Ti <sub>44</sub> substrate	40 min @ 575 °C	XRD, NI
05.14.2007	800 nm Ni <sub>47</sub> Ti <sub>53</sub> on annealed Ni <sub>56</sub> Ti <sub>44</sub>	none	XRD, NI
05.14.2007	800 nm Ni <sub>47</sub> Ti <sub>53</sub> on Ni <sub>56</sub> Ti <sub>44</sub> substrate	none	NI
08.31.2007	1.5 μm Ni <sub>50</sub> Ti <sub>50</sub> on Si (100)	60 min @ 520 °C	XRD, AFM, NI
12.07.2007	1.5 μm Ni <sub>47</sub> Ti <sub>53</sub> on Si (100)	30 min @ 525 °C	XRD, AFM, NI
04.04.2008	1.5 μm Ni <sub>50</sub> Ti <sub>50</sub> on Si (100)	60 min @ 500 °C	AFM, NI, REC
04.28.2008	500 nm Ni <sub>52</sub> Ti <sub>48</sub> on 1.5 μm Ni <sub>50</sub> Ti <sub>50</sub> on Si	none	XRD, AFM, NI
05.06.2008	750 nm Ni <sub>52</sub> Ti <sub>48</sub> on Si (100)	15 min @ 540 °C	AFM, NI

05.12.2008	750 nm Ni <sub>52</sub> Ti <sub>48</sub> on Si (100)	30 min @ 550 °C	AFM, NI
05.13.2008	1 μm Ni <sub>50</sub> Ti <sub>50</sub> on Si (100)	30 min @ 550 °C	AFM, NI
05.14.2008	1 μm Ni <sub>50</sub> Ti <sub>50</sub> on glass substrate	30 min @ 525 °C	AFM, NI, REC
05.18.2008	1 μm Ni <sub>50</sub> Ti <sub>50</sub> on glass substrate	60 min @ 525 °C	NI
05.20.2008	500 nm Ni <sub>52</sub> Ti <sub>48</sub> on 1 μm Ni <sub>50</sub> Ti <sub>50</sub> on Si	60 min @ 525 °C	AFM, NI
05.23.2008	200 nm Ni <sub>47</sub> Ti <sub>53</sub> on 1.6 μm Ni <sub>52</sub> Ti <sub>48</sub> on Si	none	AES, AFM, NI
05.23.2008	200 nm Ni <sub>47</sub> Ti <sub>53</sub> on 800 Ni <sub>52</sub> Ti <sub>48</sub> on Si	60 min @ 535 °C	AES, AFM, NI, REC

**Table 1.** List of specimens fabricated and tested in this research effort. A list of specimens not characterized in this work can be found in the Appendix. (AES = Auger electron spectroscopy, AFM = atomic force microscopy, NI = nanoindentation, XRD = x-ray diffraction, REC = recovery of inelastic deformation test)

### 3.1.2. NiTi films on NiTi Ribbon Substrates

The modification of the surface of a Ni<sub>56</sub>Ti<sub>44</sub> (at. %) substrate (1mm thick, Memry Co., Bethel, CT) was a study of particular interest because it established the graded film fabrication process to be followed in subsequent studies. Prior to deposition, the Ni<sub>56</sub>Ti<sub>44</sub> substrates were mechanically polished down to 50 nm and cleaned with ethanol. A Ni<sub>47</sub>Ti<sub>53</sub> target was chosen for the film composition to provide a concentration gradient between the film and substrate. The substrates were held approximately 7 mm from the target. A base pressure of  $1.0 \times 10^{-6}$  Torr ( $1.3 \times 10^{-4}$  Pa) was achieved; the sputtering pressure ranged from 2.0-3.0 mTorr in argon with a target power of 180 W. Before deposition onto the substrate, the target was pre-sputtered onto a shield for 30 minutes to reach sputtering equilibrium. A deposition rate of approximately 1 nm/s was used as determined by profilometry on a reference sample.

The films in this study ranged from 0.2-1.6 μm thick, and were produced both with and without a post-deposition heat treatment (see Figure 3-6).

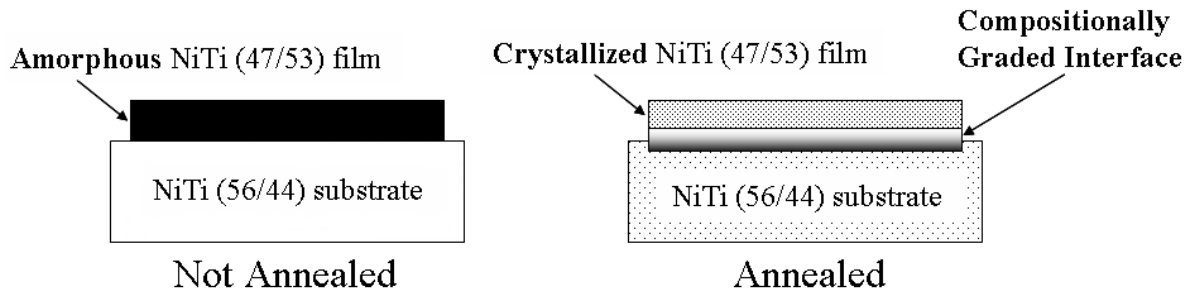


**Figure 3-6.** Schematic of  $\text{Ni}_{47}\text{Ti}_{53}$  film on  $\text{Ni}_{56}\text{Ti}_{44}$  ribbon substrate before and after annealing.

The films chosen for the heat treatment were annealed immediately following the deposition using substrate heating. The films were heated at a rate of  $8\text{ }^{\circ}\text{C}/\text{min}$ , held at  $575\text{ }^{\circ}\text{C}$  for 40 minutes and then allowed to cool to room temperature at a rate of  $3\text{ }^{\circ}\text{C}/\text{min}$ . The pressure was kept less than  $5.0 \times 10^{-6}$  Torr during the annealing process in order to prevent precipitates from forming. The annealing conditions were sufficient to initiate the crystallization process. Diffusion across the film-substrate interface was also expected to occur due to a concentration gradient. The characterization and subsequent results associated with this case study will be revisited in the corresponding sections.

### 3.1.3. Bilayer NiTi films on Single Crystal Si Substrate

The procedure developed for the single film on NiTi substrate was slightly modified for the fabrication of a bilayer film. Prior to deposition, the substrates were cleaned with ethanol. A single NiTi layer was then sputtered onto an oxidized silicon (100) substrate. After the first deposition, a NiTi film of a slightly different composition was deposited onto the first layer (see Figure 3-7).

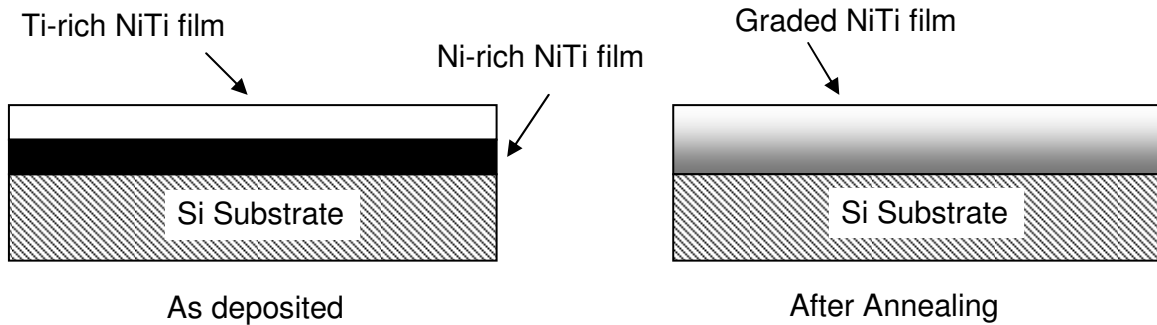


**Figure 3-7.** Schematic of the bilayer NiTi films deposited on Si substrates. The two films were of dissimilar composition.

Annealing the specimens produced diffusion across the film-film interfaces, and to a lesser extent, the film-substrate interface. This method was used to create  $\text{Si}/\text{Ni}_{47}\text{Ti}_{53}/\text{Ni}_{52}\text{Ti}_{48}$ ,  $\text{Si}/\text{Ni}_{52}\text{Ti}_{48}/\text{Ni}_{47}\text{Ti}_{53}$  bilayers of varying thickness.

## 3.2. Direct SMA Film Characterization

### 3.2.1. Scanning Probe Microscopy for Microstructural Analysis

The surface of the films was studied using scanning probe microscopy (SPM) using an atomic force microscope (AFM) and the nanoindenter. The basic principle behind SPM can be seen in Figure 3-8 [86]. A probe of some finite size is brought into contact with the surface of the sample. A force between the probe and sample is maintained as the tip is scanned across the surface. Depending on the application and specific instrument, this force “setpoint” can be attractive or repulsive. The size and geometry of the tip determines the resolution of the image. As shown in Figure 3-8, the tip size limits the ability of the probe to trace the abrupt step on the sample. For the nanoindenter, a Berkovitch tip is used with a radius of 150 nm, while the AFM uses a micromachined silicon cantilever with a

tip radius of 10 nm (an order of magnitude smaller). The scan speed also affects the quality of the image. If the scan speed is too fast, the tip does not have the time to properly trace the specimen surface, resulting in a smeared image.

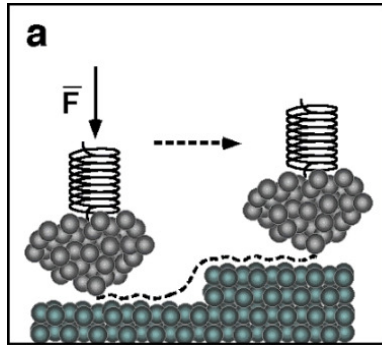


**Figure 3-8.** Schematic of scanning probe microscopy. A probe of some finite size is brought into “contact” with the sample and dragged around the surface [86].

### 3.2.2. Nanoindentation SPM on Surface Modified NiTi Substrates

Imaging the topography of the films revealed the effects of annealing. Figure 3-9 displays the changes in topography that occur in a 1.6  $\mu\text{m}$   $\text{Ni}_{47}\text{Ti}_{53}$  film on a  $\text{Ni}_{56}\text{Ti}_{44}$  substrate as a result of annealing. The samples were imaged with the nanoindenter, using the 150 nm Berkovich probe. The setpoint between the probe and sample surface was kept at 2  $\mu\text{N}$  for the duration of the scan. The scans were performed at a rate of 0.25 Hz, producing a 256 x 256 digital image in approximately 17 min.

As deposited, the NiTi films are amorphous and the surface topography is relatively uniform. Annealing the films above 525  $^{\circ}\text{C}$  initiates the crystallization process. The films were annealed through substrate heating in vacuum as described in the experimental processing section.

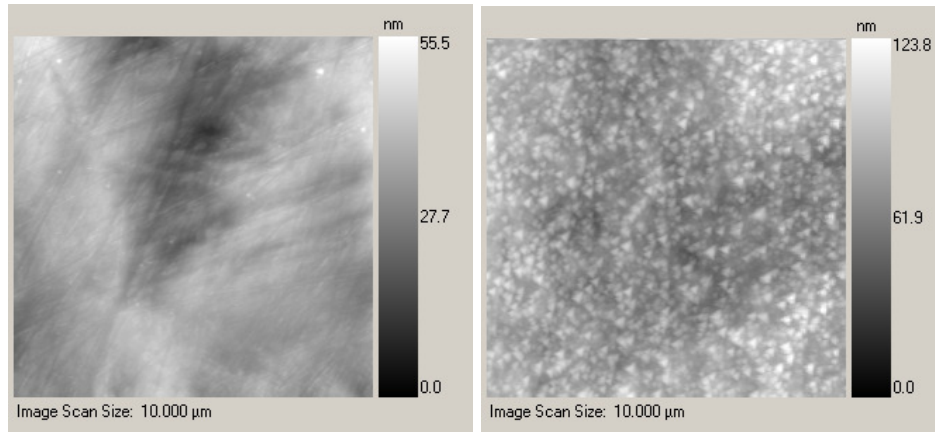


**Figure 3-9.** Scanning probe microscope images of a  $\text{Ni}_{47}\text{Ti}_{53}$  film on a polished  $\text{Ni}_{56}\text{Ti}_{44}$  substrate before (left) and after (right) heat treatment.

The annealing process appears to produce 150 nm grains in the film, but as will be shown in section 4.1.1.1, this is an artifact of the measurement. The true size of the grains, as determined through AFM, is approximately 50 nm. The resolution of the image is limited by the size of the tip, which has a radius of curvature of approximately 150 nm. The resulting grains look triangular-shaped, but this is also an artifact of the imaging process. Features on the sample surface with sizes approaching that of the tip radius will be altered to match the size and geometry of the tip. The samples were imaged before testing the mechanical properties, to ensure that the indentation would not take place on a defect, such as a crack. SPM with higher resolution than the nanoindentation scans were performed using AFM.

### **3.2.3. Atomic Force Microscopy**

AFM tests were performed at Sandia National Laboratories in Livermore, CA. The surface morphology of the NiTi films was studied using a Nano 1 atomic force microscope (Pacific Nanotechnology, Santa Clara, CA). The scans were

performed in tapping (intermittent contact) mode, where the cantilever is vibrated near the sample surface using a piezoelectric ceramic motor. Variations in the surface topography cause the amplitude and phase of the vibrations to change, which can be transformed into a digital image. An optical microscope allowed the AFM probe to be placed over micro-sized areas of interest as seen in Figure 3-10.

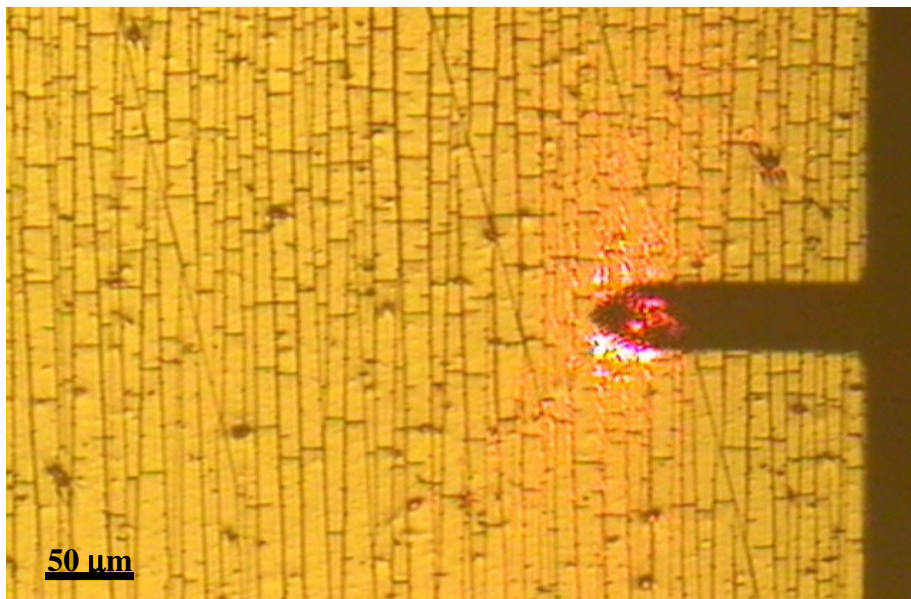


**Figure 3-10.** Optical image of the AFM probe in contact with a buckled chromium film on polymer substrate.

#### **3.2.4. Depth Profiling using Auger Electron Spectroscopy**

Compositional depth profiles in the graded films were characterized using Auger Electron Spectroscopy (AES). The Auger system used was a Physical Electronics Model 680 with typical e-beam parameters of 5.0 keV 20 nA rastered over a 200 μm x 200 μm area. The baseline vacuum for the system was approximately  $5 \times 10^{-10}$  Torr. A linear-least-squares fit was applied to all Auger data to reduce noise and reduce peak interference. Sputter Auger profiling was



done using a 2 keV 800 nA Ar<sup>+</sup> ion beam at a 45° angle of incidence. The sputter rate was for a silicon oxide standard and should be used for comparison only. The surface was milled using 2 keV Argon ions.

Figure 3-11 is an example of a depth profile on a SMA film as deposited. The specimen is a 200 nm Ni<sub>47</sub>Ti<sub>53</sub> film on a Ni<sub>56</sub>Ti<sub>44</sub> substrate. Figure 3-12 is an example of a depth profile on an annealed SMA film. The specimen tested was a 400 nm Ni<sub>47</sub>Ti<sub>53</sub> film on a Ni<sub>56</sub>Ti<sub>44</sub> substrate that heated for 40 min at 575 °C. A compositional gradient is present over the first 200 nm of the annealed film. Note that oxygen and carbon impurities are present in both the annealed and unannealed films.

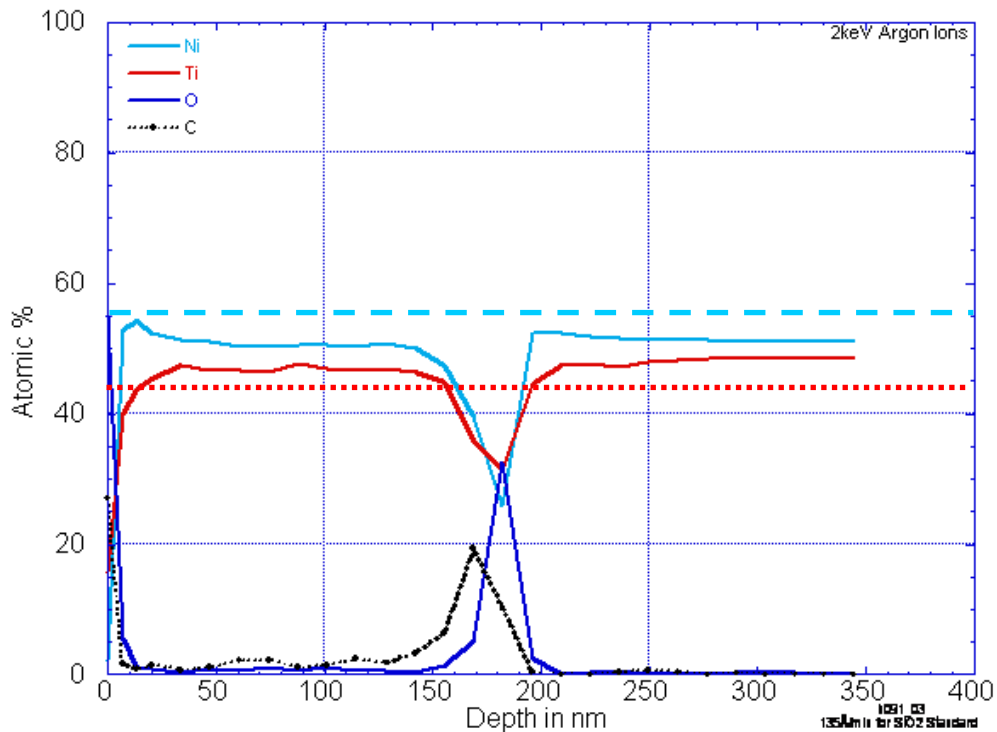


**Figure 3-11.** AES depth profile of a 200 Ni<sub>47</sub>Ti<sub>53</sub> film on a Ni<sub>56</sub>Ti<sub>44</sub> substrate as deposited (horizontal lines denote 56 at. % Ni (large blue dash) and 44 at. % Ti (small red dash)).

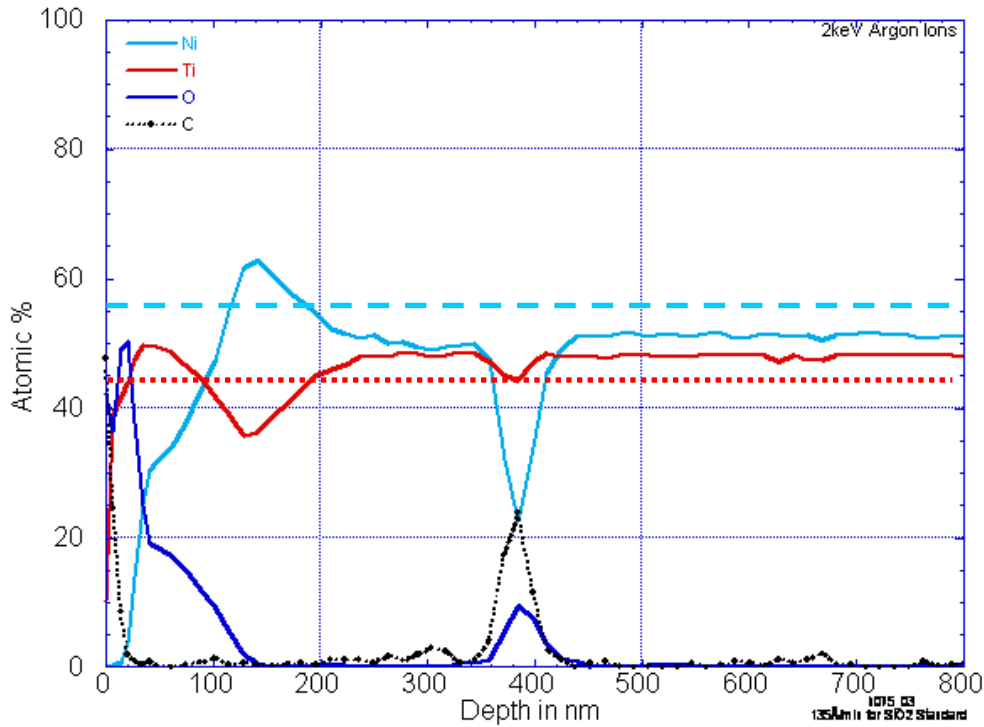


**Figure 3-12.** AES depth profile of an annealed 400 nm  $\text{Ni}_{47}\text{Ti}_{53}$  film on a  $\text{Ni}_{56}\text{Ti}_{44}$  substrate (horizontal lines denote 56 at. % Ni (large blue dash) and 44 at. % Ti (small red dash)).

### 3.2.5. X-ray diffraction for Crystal Structure Analysis

The crystal structure of the graded films was analyzed using x-ray diffraction. Diffraction studies were carried out at the x-ray crystallographic center at the University of Maryland that employs a Bruker C2 Discover powder diffractometer with GADDS technology. The beam consists of  $\text{CuK}\alpha$  radiation, designed in a parallel beam geometry that allows micrometer sized areas to be probed. The setup includes a video microscope with red laser alignment that allows for precise sample positioning. A hot stage is available so that *in-situ* heating characterization is also possible.

Depending on the crystal structure of the sample, certain diffraction angles will produce a more intense signal. The position and relative intensity of the

resulting peaks can be indexed to provide detailed information about the crystal structure of the material. However, indexing diffraction peaks can be challenging, even for homogeneous films. Any residual stress present in the film can distort the crystal structure produce a resulting shift in the peaks [87]. This problem is encountered when annealing a film-substrate system, where there is a mismatch in the coefficient of thermal expansions (CTE).

### **3.2.5.1 XRD of NiTi film on NiTi Substrate**

The residual stress issue was seen in the diffraction studies of the  $\text{Ni}_{47}\text{Ti}_{53}$  films. Figure 3-13 displays the results of XRD on a  $1.6 \mu\text{m}$   $\text{Ni}_{47}\text{Ti}_{53}$  film on a silicon substrate and a  $1.6 \mu\text{m}$   $\text{Ni}_{47}\text{Ti}_{53}$  film on a  $\text{Ni}_{56}\text{Ti}_{44}$  substrate. For the film on the  $\text{Ni}_{56}\text{Ti}_{44}$  substrate, the main peak that is observed at approximately  $2\theta = 42.5$  degrees and the smaller peak observed at approximately 61.5 degrees were indexed as the B2 cubic austenite phase. However, the peaks are slightly shifted when the film on Si substrate is considered, which is attributed to the CTE mismatch. Residual stresses can also be formed in the films during the deposition process and before any intentional (substrates will heat up to  $100 \text{ }^\circ\text{C}$  during deposition) heat treatment [88, 89]. The CTE of NiTi in the austenite phase is  $11 \times 10^{-6} \text{ }^\circ\text{C}^{-1}$  and  $6 \times 10^{-6} \text{ }^\circ\text{C}^{-1}$  in the martensite phase, while the CTE of the silicon substrate is  $2.5 \times 10^{-6} \text{ }^\circ\text{C}^{-1}$  at room temperature [53].

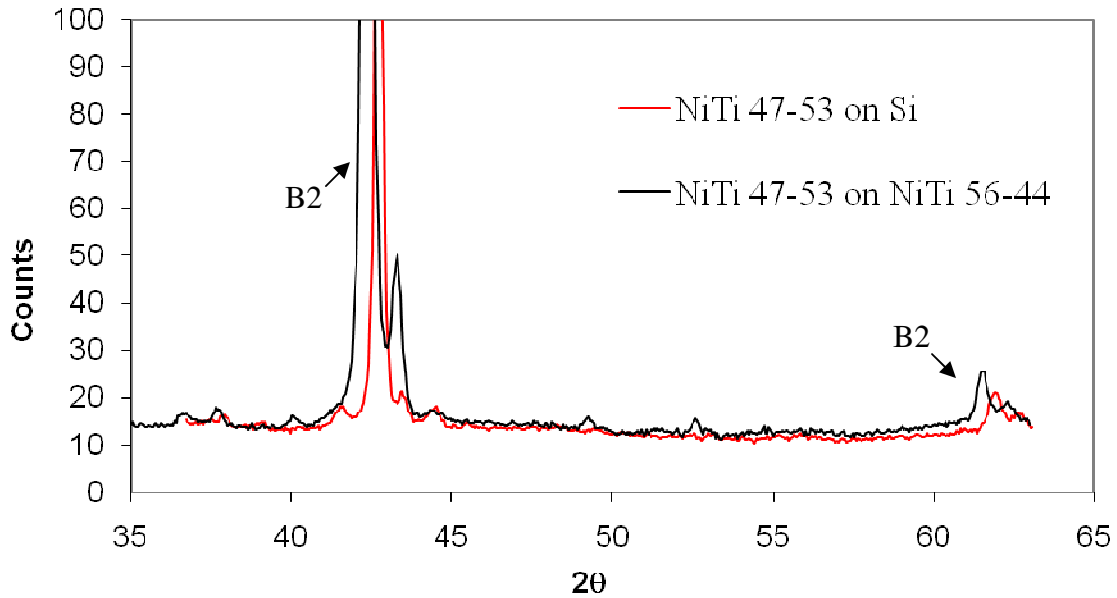


**Figure 3-13.** XRD of  $\text{Ni}_{47}\text{Ti}_{53}$  film on Si and  $\text{Ni}_{56}\text{Ti}_{44}$  substrate. Note shift in main austenite peak around 42.5 and 62 degrees.

The martensite peaks are located at  $2\theta$  angles of 1-2 degrees on either side of the main austenite peaks [53]. Therefore, peaks due to the formation of new crystal structures must be decoupled from the peak shifts.

Characterizing the crystal of structure of a graded film will also be complicated because of the nature of the diffraction measurement. Depending on the intensity of the radiation, the diffraction pattern that is observed is a bulk response from tens of thousands of crystal planes into the surface of the specimen. The diffraction response from a graded film will thus be a complex function of the variations in the composition or crystal structure with respect to depth. Therefore, the approach taken in this study will be to compare relative intensities of diffraction peaks between films of varying thickness and composition.

### 3.3. Indirect SMA Film Characterization

#### 3.3.1. Nanoindentation for Nanomechanical Property Analysis

The nanomechanical properties of the films were determined at various depths into the film to indirectly characterize the compositional-gradient. The tests were performed using a Hysitron Triboindenter Nanoindentation system (Hysitron Co., Minneapolis, MN). The tip used was a diamond Berkovich probe, with a radius of curvature of approximately 150 nm and an included angle of 142 degrees (see Figure 3-14).

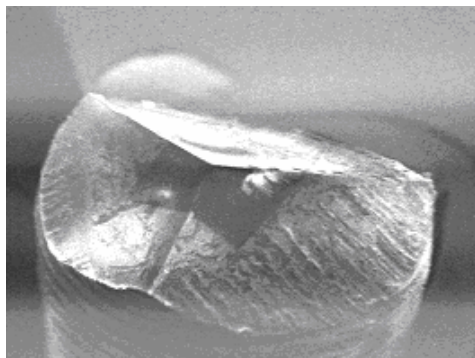


**Figure 3-14.** Diamond Berkovich tip with an included angle of 142 degrees [65].

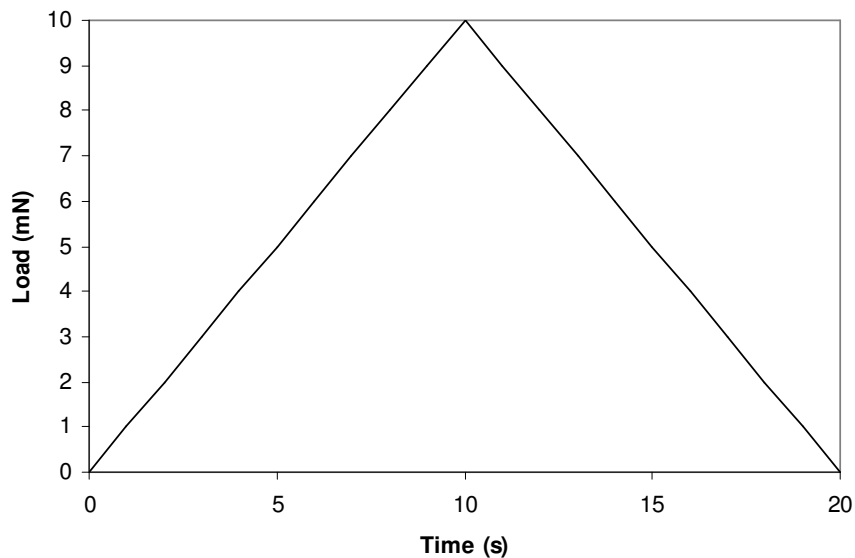
The tip size and geometry limits the contact depth of the indentations because the maximum applied force is predefined. For the NiTi system, this depth occurs around 300 nm, although an extra 50-100 nm can be realized once the films are crystallized. Fused quartz was used as a calibration sample because it possesses well-known mechanical properties. The tip-shape calibration was accomplished by making several indents in the quartz calibration sample. The indentations covered a wide range of contact depths so that the calibration would be consistent with the range of indents on the graded films.

The elastic modulus and Poisson's ratio of the quartz sample was assumed to be 72 GPa and 0.17, respectively [65]. The area as a function of contact depth was then defined using equation 8. The area function was recalculated every several months to account for the blunting of the tip.

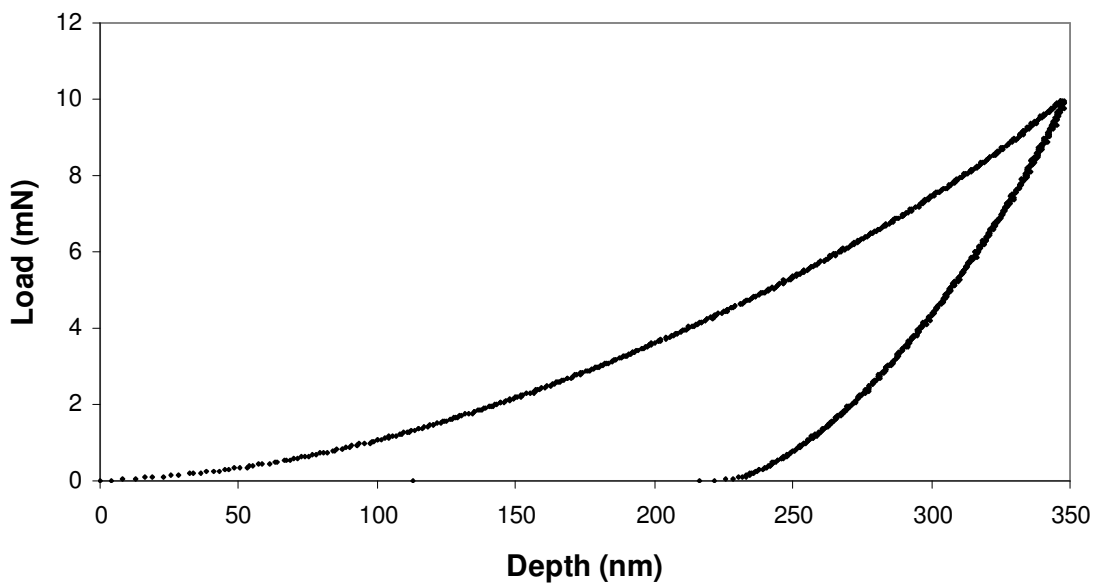
The loading function could be varied depending on the type of material to be tested. The loading rate and peak applied load are the parameters that must be defined prior to indentation. The indentation of metals is relatively straightforward because the displacement into the material can be considered time independent. When indenting polymeric samples, it is important to include a "hold-time," a segment of time with constant applied force between the loading and unloading processes, so that the material may relax before the measurement on the unloading segment is made.

### **3.3.2. Nanoindentation of NiTi film on NiTi Substrate**

An example of a typical nanoindentation test is the case of the surface-modified NiTi substrate. The goal was to test the mechanical properties of the films at various distances relative to the film-substrate interface. For the films that were annealed, this interface was no longer well defined because of the diffusion process. A 40  $\mu\text{m}$  square area was selected in the middle of each film. Sixty-four points in an 8 x 8 grid, spaced 5  $\mu\text{m}$  apart, were indented using an initial load of 0.1 mN. The peak load of each successive indent was increased by approximately 0.15 mN with a final load of 10 mN, while maintaining a constant loading rate of 1 mN/s (see Figure 3-15).



**Figure 3-15.** Load function used for indentation of surface-modified NiTi substrate. The peak load was varied from 0.1-10 mN.



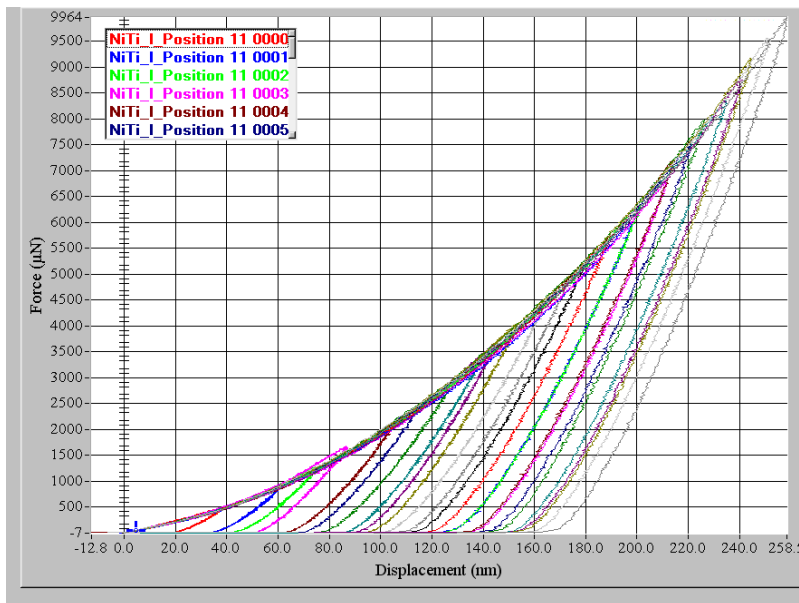
**Figure 3-16.** Typical force vs. displacement curve using the load function seen in Figure 3-15. The specimen was an annealed 400 nm  $\text{Ni}_{47}\text{Ti}_{53}$  film on a  $\text{Ni}_{56}\text{Ti}_{44}$  substrate.

Figure 3-16 is an example of a typical force-displacement curve obtained via nanoindentation using the load function seen in Figure 3-15. The specimen in this case was an annealed 400 nm  $\text{Ni}_{47}\text{Ti}_{53}$  film on a  $\text{Ni}_{56}\text{Ti}_{44}$  substrate. A bare portion of the substrate that had been masked during deposition was indented in

the same manner before and after heat treatment so that the baseline behavior of the substrate could be established.

### 3.3.3. Nanoindentation of NiTi Bilayer Films on Si Substrates

The nanoindentation procedure used for testing the graded films on the bulk NiTi substrates was repeated for the indentation tests on the bilayer graded NiTi films on Si substrates. In general, the bilayer films had a lower surface roughness than the films on bulk NiTi substrates. This is due to the low roughness of the Si substrate, which was determined to be approximately 5 nm using AFM. The loading curves for the indents at various spatial locations all lie along the same curve (see Figure 3-17). This caused slightly less scatter in the data for the nanoindentation tests on the graded bilayer films on Si substrates.



**Figure 3-17.** Loading curves for an annealed 800 nm  $\text{Ni}_{47}\text{Ti}_{53}$  film on a 1  $\mu\text{m}$   $\text{Ni}_{47}\text{Ti}_{53}$  film on a Si substrate. The uniformity of the surface allows the loading curves for each indent to line up. Loading curves for the films on the bulk NiTi substrates do not show the same uniformity due to their increased surface roughness.



### 3.4. Nanoscale Characterization of Shape Memory Effect

#### 3.4.1. A Posteriori Recovery of Nanoindents after Heating

A new method for characterizing the shape memory effect in the films at the nanoscale was established using the scanning probe feature of the nanoindenter to characterize recovery after heating. Micro-sized indents were first made in the film using a Vickers hardness tester. These relatively large indents (approximately 20  $\mu\text{m}$  across, as opposed to the approximately 1  $\mu\text{m}$  nanoindents) were used as a fiducial so that subsequent nanoindents could be easily found using an optical microscope (see Figure 3-18).

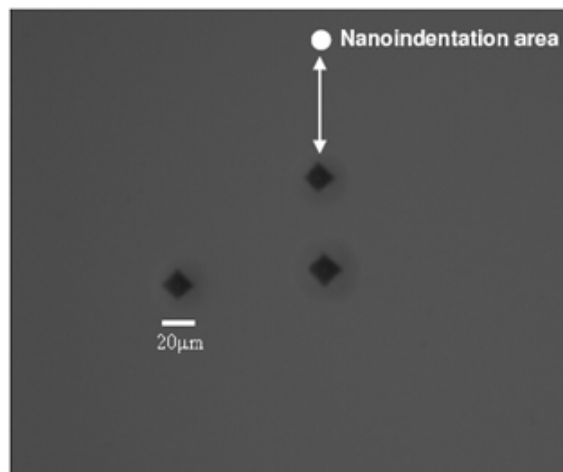


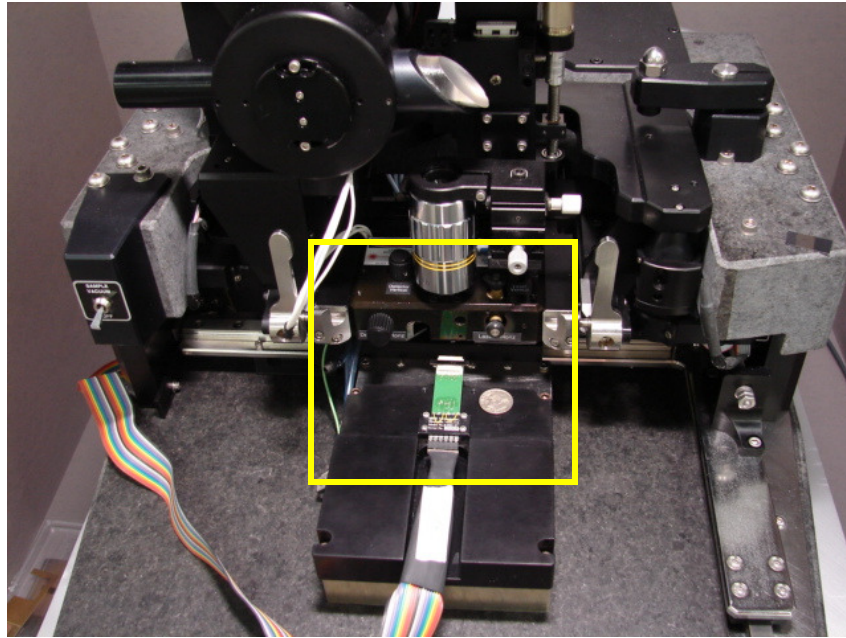
**Figure 3-18.** Optical image of microindents used as a fiducial for nanoindentation area.

An area selected for nanoindentation was located approximately 100  $\mu\text{m}$  above a featured microindent. The microindents patterned in a non-symmetric way to ensure that the nanoindentation area was unambiguous. Nanoindents were scanned using the nanoindenter and a height profile of the indent and surrounding area was obtained. The sample was then removed from the nanoindenter and heated in a furnace at 40  $^{\circ}\text{C}$  for an hour. The sample was

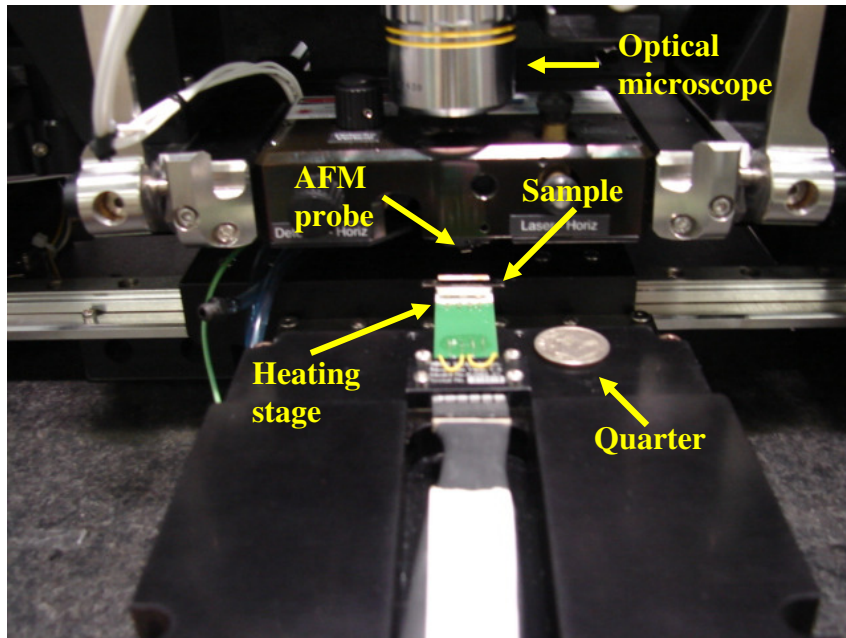
replaced in the nanoindenter and the indent of interest was found using the microindent benchmark method. The indent was re-scanned and the change in height profile was recorded. Each scan was performed at a rate of 0.25 Hz, meaning that the probe scanned a horizontal line across the image and returned back to the initial starting point in 4 seconds, before moving to the next line. This process was repeated with heat treatments of 60 °C, 80 °C, and 100 °C.

### **3.4.2. *In situ* Recovery Analysis using AFM and Heating Stage**

The previously described method using fiducials and subsequent scanning of the indents before and after heating with the nanoindenter probe was improved upon by using an atomic force microscope with an integrated heating/cooling stage. *In situ* recovery experiments were performed using a K-20 programmable heating stage (MMR Technologies Inc., Mountain View, CA). The experimental setup can be seen in Figure 3-19. Integrated into the AFM system, the stage allowed the samples to be imaged over a wide range of temperatures (300-400 K) with a high degree of accuracy and stability (  $\pm 0.1$  K). An Aerostat PC ionizing air blower (Simco) was used to mitigate the electrostatic charge buildup on the samples. The blower produced an airflow rich in positive and negative ions, thus neutralizing the sample surface.



(a)



(b)

**Figure 3-19.** (a) Experimental setup of atomic force microscope with integrated heating/cooling stage for characterization of recovery *in situ*. A close up of the highlighted area can be seen in (b).

The indent array was located using an optical microscope in conjunction with the AFM. The array was initially scanned at 300 K several times to allow the

system to equilibrate. Once stabilized, the film was heated to 310 K. The array was then rescanned a few times, allowing the scan to equilibrate. This process was repeated in 10 K temperature intervals up to 350 K. The films were imaged in 10 K cooling intervals using the same approach.

The maximum height of each indent was measured in each image. The vertical recovery was recorded at each temperature interval using the initial scan at 300 K as a reference. An indent array in a passive 2  $\mu\text{m}$  thick gold film on a silicon substrate was tested in the same manner to ensure that the observed recovery in subsequent tests on the active films was solely due to the SME and not an artifact of the AFM measurement.

## 4. Results and Discussion

### 4.1. Direct Characterization of Graded SMA Films

#### 4.1.1. Scanning Probe Characterization of Grain Structure

As deposited, the NiTi films are amorphous. An annealing process is required to crystallize the films and enable the shape memory effect. This heat treatment causes significant changes to the film appearance, both macroscopically and microscopically. Macroscopically, the films appear specular due to the uniformity of the deposition process. The annealing process causes the films to appear cloudy. This is due to the increased surface roughness which is the result of surface relief [34].

The surface microstructure was observed using nanoindentation scanning probe microscopy. Figure 4-1a shows a scan of a Ni<sub>47</sub>Ti<sub>53</sub> film annealed at 525 °C for 15 minutes. This annealing temperature is on the threshold of crystallization initialization and the time allowed for heating was insufficient for full crystal growth. As a result, the grains are just beginning to form in self-assembled rings. Figure 4-1b shows a similar film heat treated at 575 °C for approximately 40 minutes. The grains have been given almost three times more time to grow at a higher temperature; as a result, the grains are larger and cover the entire area of interest. It should be noted that the resolution of these images is again limited by the size of the berkovich tip, which has a radius of curvature of approximately 150 nm. The grains also appear to be triangular shaped, but as discussed earlier, this is an artifact that is due to the geometry of the tip.

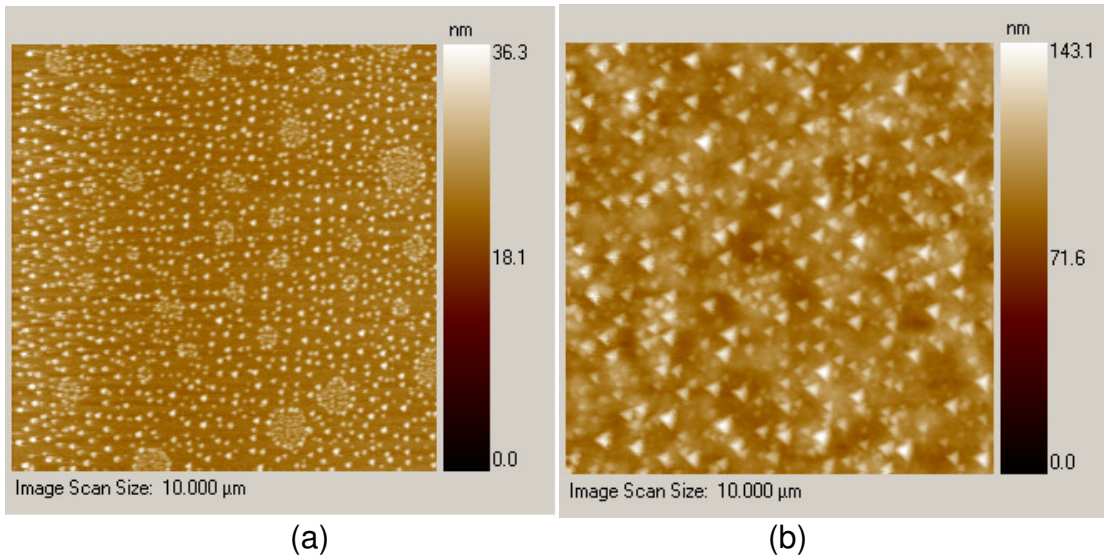


**Figure 4-1.** (a) SPM image of a  $\text{Ni}_{47}\text{Ti}_{53}$  film on a Si substrate annealed at 525 °C for 15 minutes. Note how the grains form in self-assembled rings. (b) SPM image of a  $\text{Ni}_{47}\text{Ti}_{53}$  film on a Si substrate annealed at 575 °C for 40 minutes.

#### 4.1.1.1 Atomic Force Microscopy of Film Microstructure

As discussed in section 3.2.2, the scanning probe microscopy of the films using the nanoindenter is limited by size of the Berkovich tip. A tip radius of 150 nm limits the scan resolution to approximately 150 nm. In addition, the non-symmetrical geometry of the Berkovich tip results in artificial topographic features, e.g. the previously mentioned triangular grains in Figure 4-1(b). The resolution of the topographic scans was improved by an order of magnitude by using an AFM with a tip radius of approximately 10 nm.

The sensitivity of the AFM probe allows images to be taken with higher resolution, yet the sharper AFM tip is less robust than the nanoindenter tip which makes quality imaging more difficult. The fragility of an AFM probe makes it susceptible to damage. Imaging a relatively hard (i.e., ceramic) or relatively rough (i.e., features varying in vertical direction by more than 500 nm) can cause the tip to become blunted or the cantilever to become cracked. This results in

the potential for images containing artifacts. These problems are mitigated by running the scans in non-contact or tapping (intermittent contact) mode, where the distance between the tip and sample are great enough so that the dominating forces are attractive in nature. Figure 4-2 displays the images taken on a bilayer NiTi film on a Si substrate. The film appeared to contain oblong-shaped grains that were approximately 100-200 nm long. This unusual microstructure prompted the recalibration of the tip on a Au film standard. Tests on the calibration sample again showed the existence of the oblong features instead of the expected spherical grain structure, indicating that the AFM probe was damaged and that the oblong-shape was an artifact of this damage.

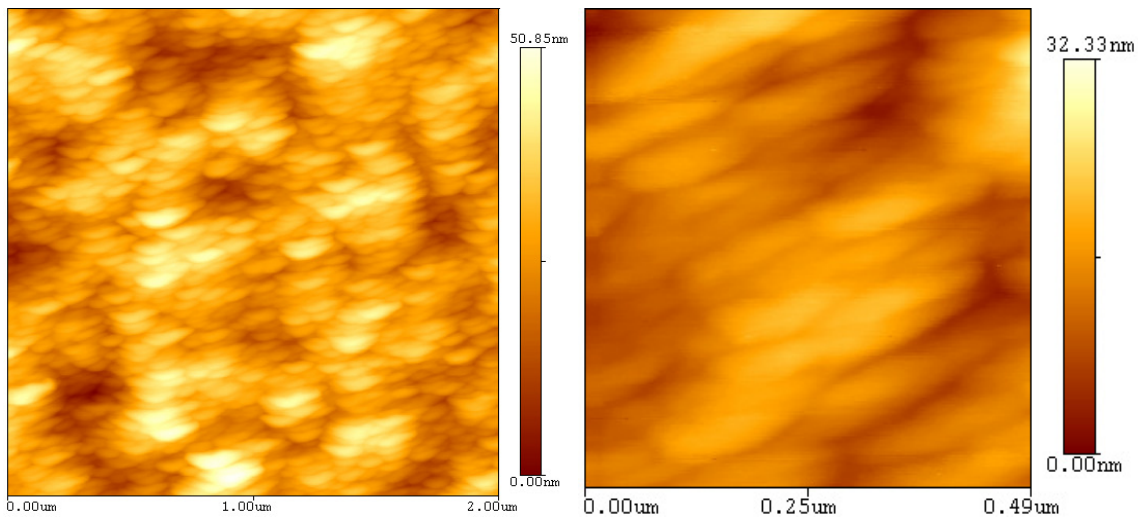


**Figure 4-2.** AFM images of a Si/1 μm Ni<sub>52</sub>Ti<sub>48</sub>/0.5 μm Ni<sub>47</sub>Ti<sub>53</sub> bilayer film taken with a damaged AFM probe. The left image (2 μm) shows oblong-shaped grains, the right image (0.5 μm) is a zoomed-in view.

Rescanning the Au standard film with a new tip showed the expected grain structure; the results can be seen in Figure 4-3.



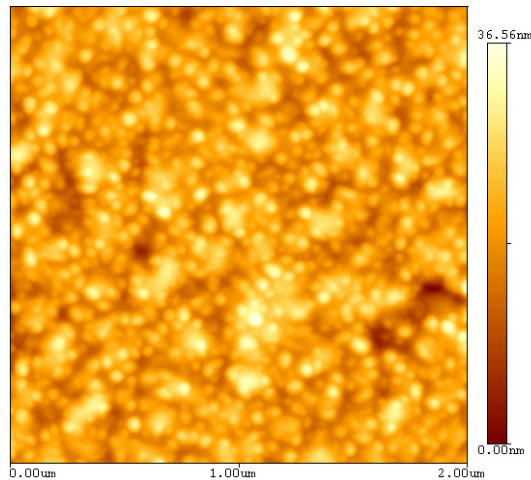


**Figure 4-3.** 2 μm AFM image of a Au film calibration sample.

Rescanning the NiTi bilayer film with the new AFM probe revealed a much different and expected microstructure (see Figure 4-4). The images show approximately 50 nm spherically-shaped grains, which was consistent with scans of NiTi films processed under similar conditions. The fine grain structure of the NiTi films is likely a result of the fast annealing process.

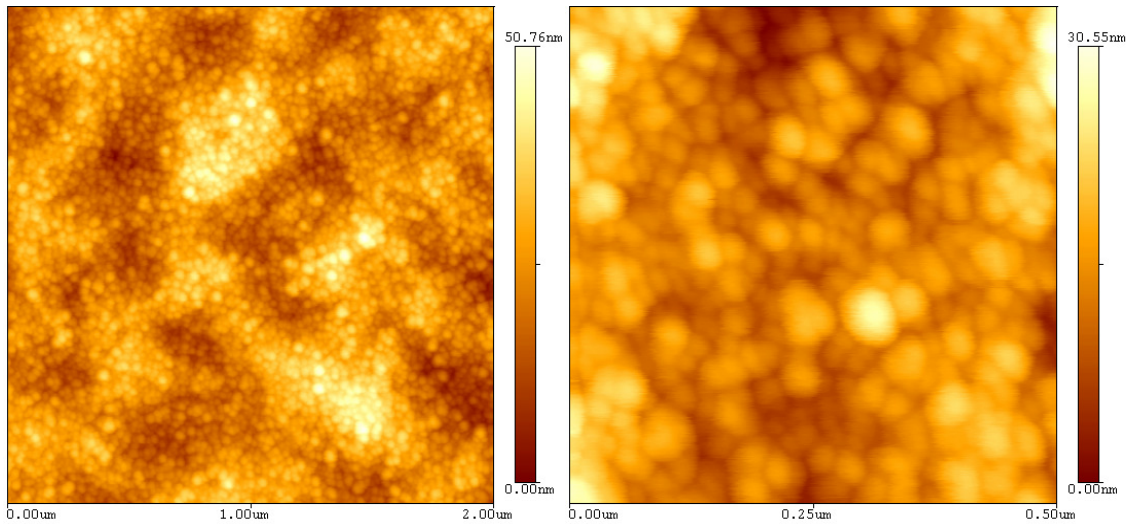


**Figure 4-4.** AFM images of a Si/1 μm Ni<sub>52</sub>Ti<sub>48</sub>/0.5 μm Ni<sub>47</sub>Ti<sub>53</sub> bilayer film using a new AFM probe. The left image is a 2 μm scan and the right image is a 0.5 μm zoomed-in view.

The main focus of the film processing technique was to create a composition gradient through diffusion. The annealing time was limited to



produce a well-defined gradient over a distance of 100-500 nm from the interface, instead of the constant composition across the interface that would result from a slower annealing process. Therefore, the samples were only held above their crystallization temperature for 30-60 min, leaving little time for the grains to grow.

The effects of the annealing time were studied in greater detail by imaging the NiTi film shown in Figure 4-1a using AFM. The result of the scan can be found in Figure 4-5. The area highlighted was observed in greater detail in Figure 4-6, and studied in even greater detail in Figure 4-7. Relatively small grains (20-50 nm) that appear in the background of the AFM scans were not picked up by the nanoindenter probe.

It can also be seen that using the sharper AFM tip removes the triangular grain shape artifacts that are seen with the Nanoindentation SPM. However, when the size of the grains are above the resolution limit of the Nanoindentation SPM (150 nm), the resulting grain size obtained with the AFM was identical. This indicated that Nanoindentation SPM is adequate for resolving the size of larger grains, but for smaller grain sizes and precise morphology characterization the AFM must be used. Since the latter case only occurs in the initial stage of the crystallization process, Nanoindentation SPM will be generally adequate for confirming the grain structure of the films.

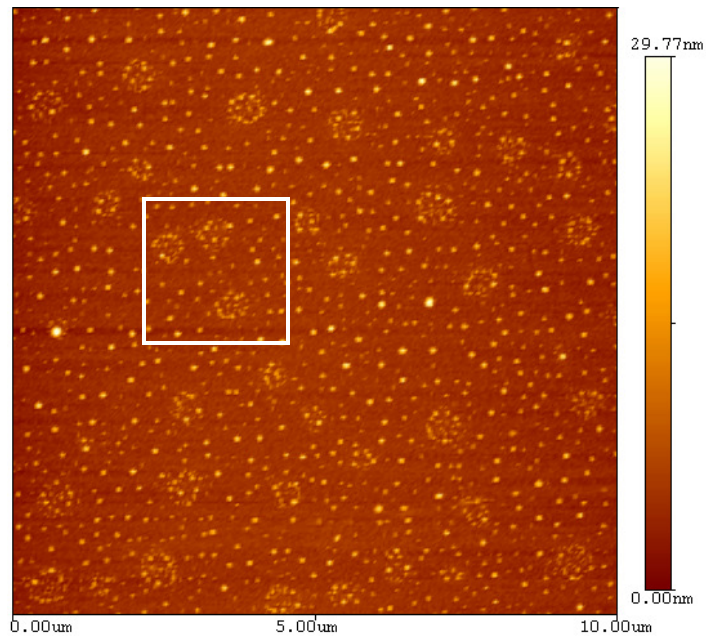


**Figure 4-5.** AFM scan of the Ni<sub>47</sub>Ti<sub>53</sub> film on a Si substrate seen in Figure 4-1a. See Figure 4-6 for close up of highlighted area.

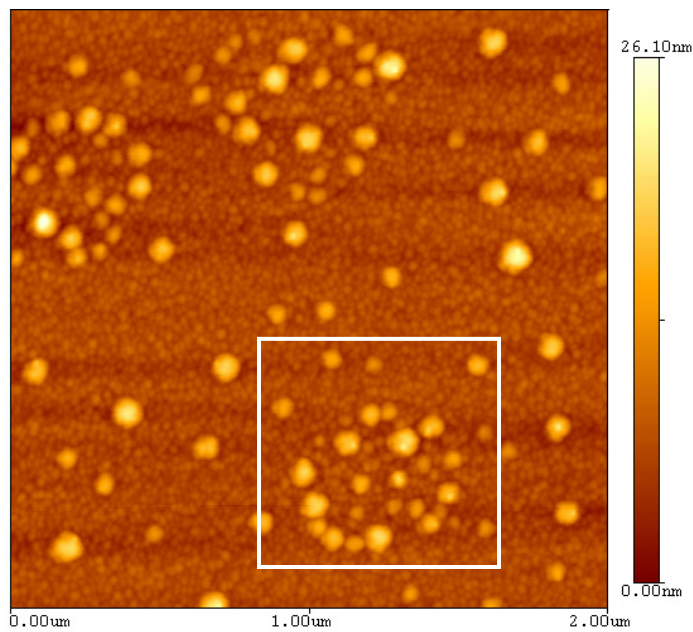


**Figure 4-6.** 2 μm AFM scan of the white box in Figure 4-5. Figure 4-7 shows a close up of the highlighted area.

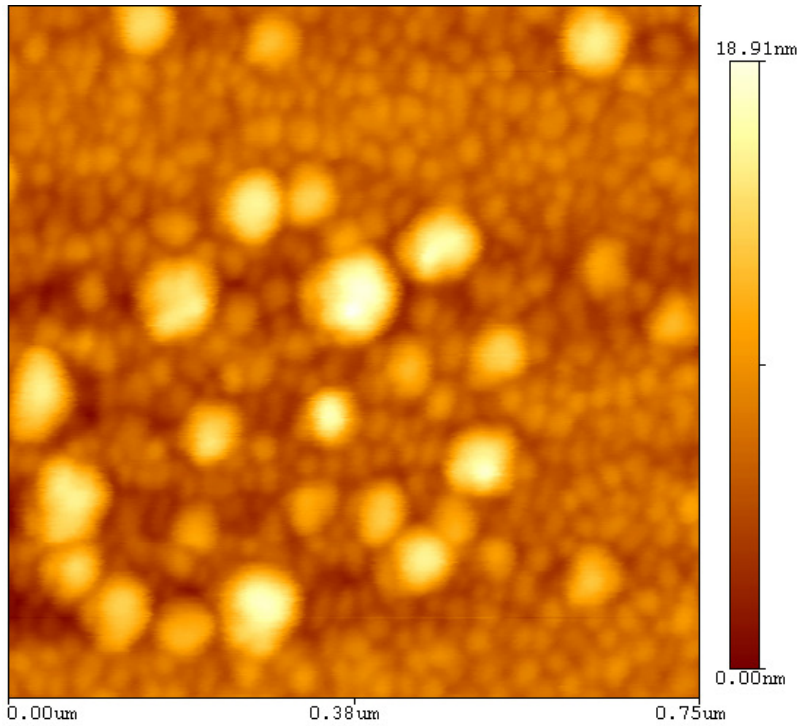


**Figure 4-7.** 0.75  $\mu\text{m}$  AFM scan close up of the white box in Figure 4-6.

#### **4.1.2. Depth Profiling of Graded Films using AES**

The ratio of Ni to Ti is a key parameter in the design of NiTi SMAs because it controls the temperature at which the martensite-to-austenite transformation occurs. The transformation temperature of equiatomic NiTi is known to be close to room temperature. However, a slight deviation in the composition can have a dramatic effect; raising the Ni content by approximately 0.2 at. % has been shown to lower the transformation temperature by as much as 25  $^{\circ}\text{C}$  [53].

The composition of NiTi films was analyzed as a function of depth into the film using AES. The results of an AES test on a NiTi bilayer film before annealing (i.e., as deposited) can be seen in Figure 4-8. Ni, Ti, C, O and Si species were detected in the test. Viewing the depth profile from left to right, a

sharp interface between the sputtered NiTi layer and the substrate can be seen at approximately 200 nm. This is the expected result, given the relatively low temperature of the substrate during deposition. A thermocouple placed on the substrate during the sputtering process showed that the film ranged from 25 °C (at onset) to 100 °C (at completion), well below the temperature required to cause any measurable diffusion across the film-film interface. The movement of the film-substrate interface can be approximated using equations 14 and 15 in section 4.2.3, with a pre-exponential factor and activation energy of  $2 \times 10^{-7} \text{ m}^2 \text{ s}^{-1}$  and  $142 \text{ kJ} \cdot \text{mol}^{-1}$ , respectively. Assuming that the temperature of the film was 373 K for the duration of the deposition process (high end of the estimate), the diffusion length of the original film-substrate interface is less than 1 nm. At a depth of approximately 2.5  $\mu\text{m}$  the Ni and Ti signals drop off, and the silicon substrate becomes the dominant chemical response.

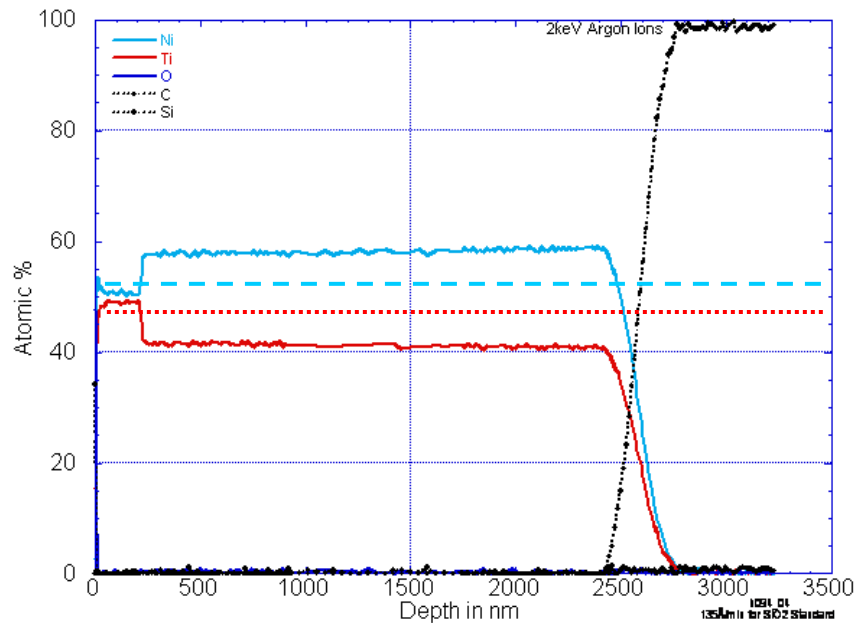


**Figure 4-8.** AES depth profile of a 200 nm  $\text{Ni}_{47}\text{Ti}_{53}$  film on a 1600 nm  $\text{Ni}_{52}\text{Ti}_{48}$  film on a Si substrate as deposited (horizontal lines denote 52 at. % Ni (large blue dash) and 48 at. % Ti (small red dash)).

The sharp interface between the films before annealing is expected, however the atomic percent measured as a function of depth was not the expected result. The results varied absolutely between 3-10% of the expected atomic percent from the sputtering targets. This could be due to the poor sputtering yield of the titanium that occurs during the deposition process, or during the profiling. The assumption of the depth profile is that the material is sputtered away at a rate similar to that of the calibrated SiO<sub>2</sub> standard, which affects both the depth and the relative composition that are reported. In addition, it is possible that the AES measurement itself is affecting the material. While the sharp interface near 200 nm is expected, the interface between the bilayer film and the Si substrate was at 2500 nm rather than the expected 1800 nm. Furthermore, the interface is not as sharp as the initial bilayer interface, with an extent of nearly 300 nm. This is not expected since the substrate is quite flat (roughness measured at 5 nm by AFM), and there should be no diffusion given the sputtering conditions used during deposition. Therefore, the AES depth profiling was used mainly as a qualitative measure of the compositional variation in this investigation.

An AES depth profile on an annealed film can be seen in Figure 4-9. The sample tested was a 200 nm Ni<sub>47</sub>Ti<sub>53</sub> film on a 800 nm Ni<sub>52</sub>Ti<sub>48</sub> substrate that was annealed at 550 °C for 30 min. As indicated previously, the actual atomic percent of the film as a function of depth can not be stated quantitatively, due to the assumption that the Ni and Ti species sputter at the same rate as the SiO<sub>2</sub> standard. In addition, the interface between the film and

Si substrate occurs at 800 nm, instead of the expected depth of 1  $\mu\text{m}$ . However, a clear difference in the AES response can be seen in the annealed film when compared to the unannealed sample. A compositional gradient can be seen over the first 150 nm of the film as a result of the diffusion process. This variation in composition near the surface of the film will cause the transformation temperature to vary as well. The transformation temperature of equiatomic NiTi is known to be close to room temperature. However, a slight deviation in the composition can have a dramatic effect; altering the composition by as little as 0.2 at. % has been shown to shift the transformation temperature by as much as 25  $^{\circ}\text{C}$  [53]. Therefore, it is expected that these graded films will display the two-way SME.

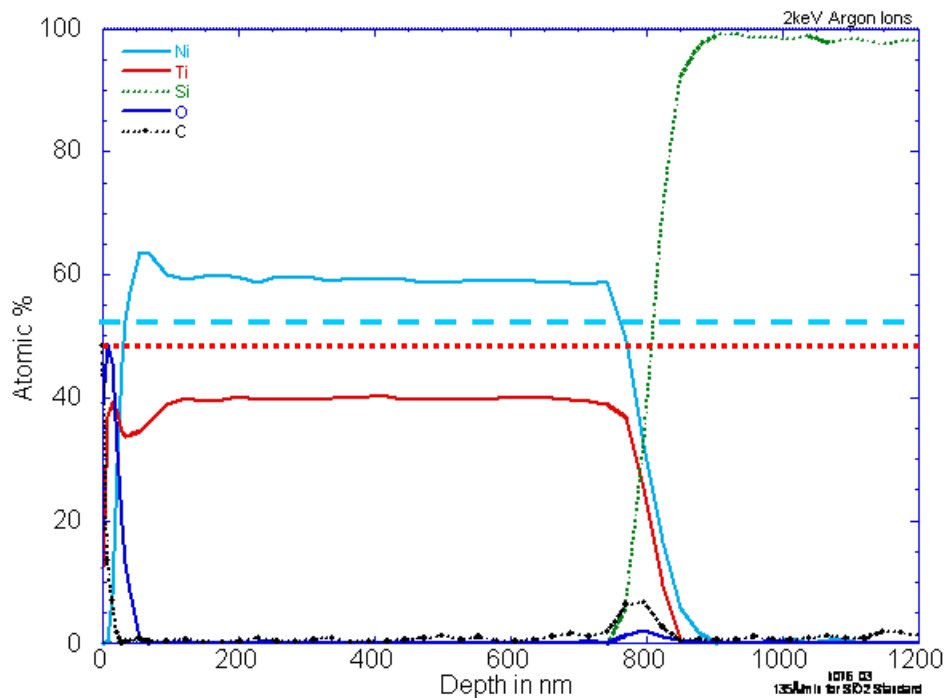


**Figure 4-9.** AES depth profile of a 200 nm  $\text{Ni}_{47}\text{Ti}_{53}$  film on an 800 nm  $\text{Ni}_{52}\text{Ti}_{48}$  film on a Si substrate after annealing (horizontal lines denote 52 at. % Ni (large blue dash) and 48 at. % Ti (small red dash)).

The impurity level in the films is significantly higher after they have been annealed. This is likely due to the outgassing of the heater during the annealing process. This is important because impurities will reduce or prevent the SME in the films. The impurities also cause the films to lose ductility which can decrease their effectiveness as an actuation due to the difficulties associated with handling and manipulating a brittle material. However, the impurity level in the annealed films can be reduced by cleaning the substrates with ethanol prior to deposition and maintaining a clean sputtering chamber. In addition, the annealing time should be limited in order to limit the distance that the impurities can diffuse into the film. It is also important to point out that at the film-substrate interface, the extent of the variation is almost identical to the unannealed specimen. Therefore, this is some indication that this variation is not due to diffusion, but rather some artifact of the measurement process.

Figure 4-10 shows an AES profile of a bilayer film that was subject to a relatively long annealing process. While most of the films prepared in this study were annealed for 30-40 min, the bilayer film shown in the figure below was annealed for over 2 hr. As a result, the film showed a relatively complex AES response. Gradients in the atomic percent of Ni and Ti are present, which is the desired result; however, the impurity levels are much higher than the films annealed for 30-40 min. In addition, the Si substrate appears to have diffused close to 1  $\mu\text{m}$  into the film. As a result, this film was extremely brittle and came free from the substrate after repeated handling. Thus, the annealing time will be

limited in order to maintain film quality, which will also limit the gradient architectures that can be formed using the diffusion modification method.

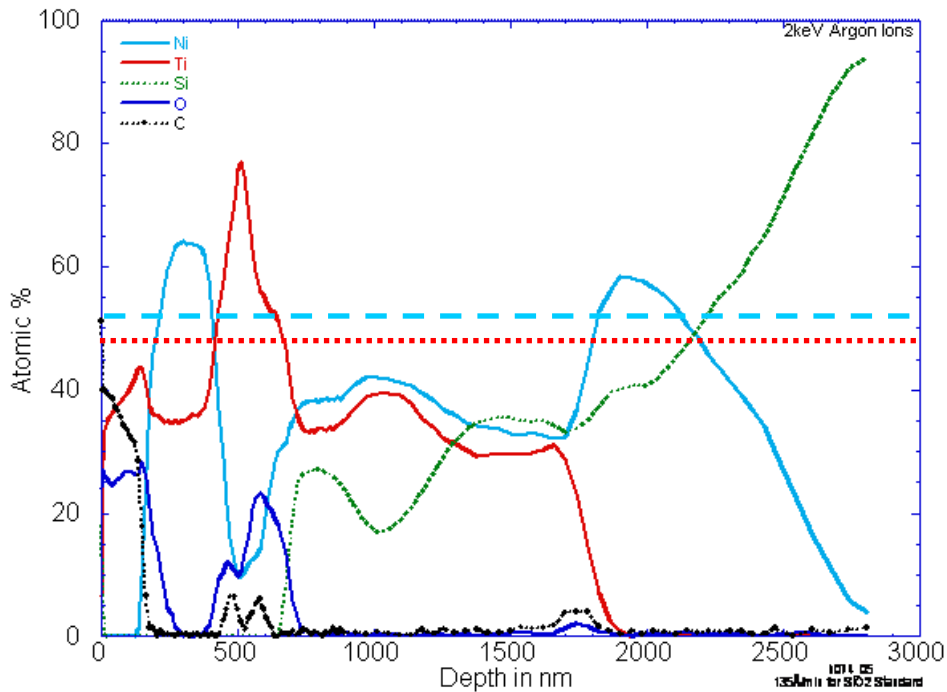


**Figure 4-10.** AES depth profile of a 500 nm  $\text{Ni}_{47}\text{Ti}_{53}$  film on a 1000 nm  $\text{Ni}_{52}\text{Ti}_{48}$  film on a Si substrate after annealing at 550 C for 2 hrs (horizontal lines denote 52 at. % Ni (large blue dash) and 48 at. % Ti (small red dash)).

### 4.1.3. XRD Characterization of Crystal Structure

The crystal structure of the films was examined using X-ray diffraction (Powder Diffractometer, Bruker D8 Advance with GADDS, chemistry department at the University of Maryland). Tests on the untreated  $\text{Ni}_{56}\text{Ti}_{44}$  substrate revealed an amorphous structure. The annealed substrate was found to be polycrystalline, consisting of small amounts of monoclinic martensite with primarily cubic austenite phases (Figure 4-11). For comparison, XRD tests on the silicon substrate revealed a single crystal response.



As deposited the films are amorphous, as seen by the broad peak in Figure 4-12. After the annealing process, the film-substrate system shows an increased austenite peak as well as two new small martensite peaks. A film deposited onto a Si (100) wafer under the same sputtering and annealing conditions showed a similar XRD response.

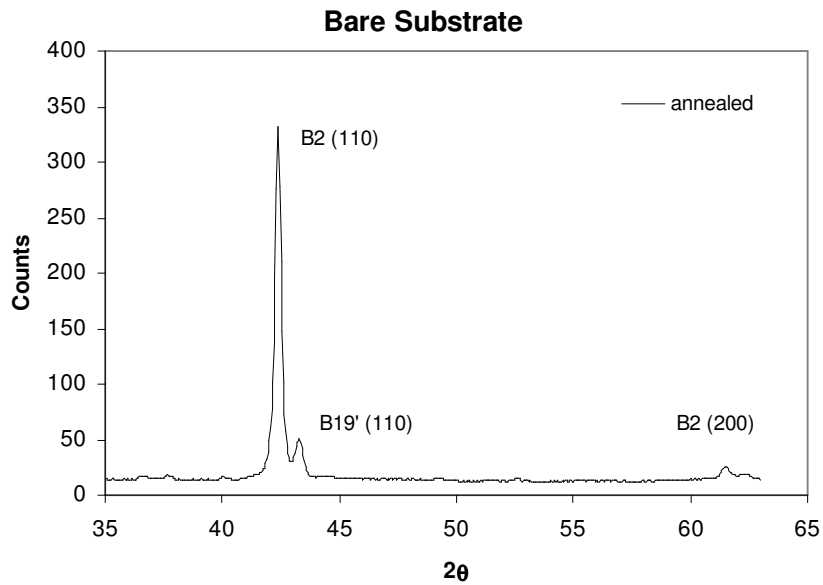


**Figure 4-11.** X-ray diffraction results of the bare Ni<sub>56</sub>Ti<sub>44</sub> substrate after the annealing process.

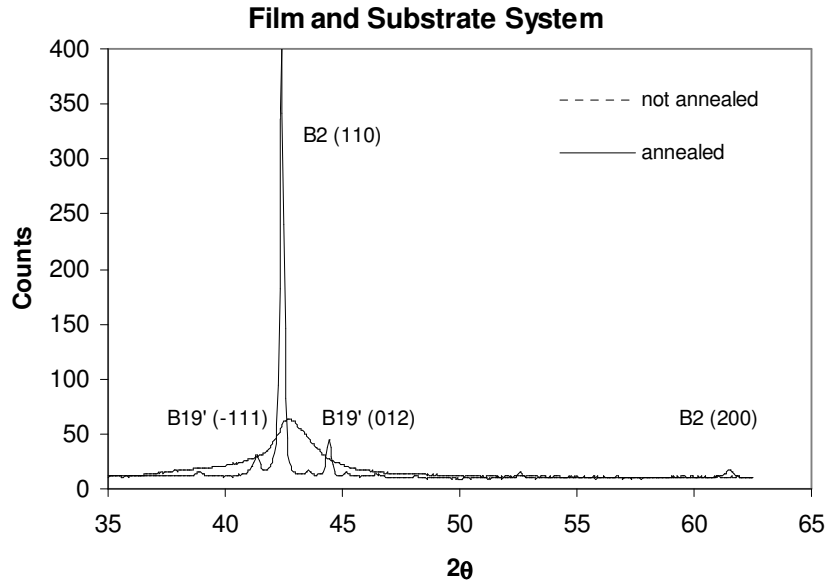


**Figure 4-12.** X-ray diffraction results of a 1600nm  $\text{Ni}_{47}\text{Ti}_{53}$  film on  $\text{Ni}_{56}\text{Ti}_{44}$  substrate before and after annealing.

The presence of increased austenite at the surface of the film suggests less martensitic rearrangement when subject to applied stress. Therefore, we expect the shape memory effect to be relatively small at the austenite-rich film surface and increasing as we approach the film-substrate interface. As discussed in XRD experimental section, the presence of residual stresses in the films can complicate the diffraction response. A strain on a given crystal will distort the lattice to some extent and produce a resulting shift in the diffraction peaks. Several of the established austenite and martensite peaks fall within a range of  $2\theta$  equal to 3-4 degrees, thus a shifted peak due to a strained lattice could easily be mistaken for an altogether different crystal peak. However, the XRD results show that both the film and substrate are highly austenitic. There is an increase in the amount of martensite in the substrates, but the relative amount is small. In addition, the diffusion process is expected to relieve some of the

stress, as the abrupt interface between film and substrate is replaced by a gradual graded layer.

As mentioned in the experimental section, XRD will only provide a bulk response to the crystal structure in the films. This is particularly important for the case of a graded structure, where the crystal structure varies as a function of depth. The majority of the films processed in this study consisted primarily of the austenite phase, the expected result for Ti-rich films at room temperature. However, the graded region was expected to pass through the equiatomic elemental composition where the martensite phase is present at room temperature. AES of the NiTi films showed a gradient in composition that passes through this region, although the exact depth at which the equiatomic composition occurred could not be pinpointed due to limitations of the depth profiling.

## **4.2. Indirect Characterization of SMA Films using Nanoindentation**

### **4.2.1. Nanoindentation of Homogeneous SMA Films on Si Substrates**

The mechanical properties of a commercially-available (TiNi alloy co., Oakland, CA) 2  $\mu\text{m}$  thick  $\text{Ni}_{50}\text{Ti}_{50}$  film on a Si substrate were tested using a Hysitron Nanoindentation system. The films were in the martensite phase at room temperature [34]. The peak load was varied, while maintaining a constant loading rate, at different spatial locations within a 20  $\mu\text{m}$  square site on the film. This allowed the mechanical properties to be measured at various contact depths. Figure 4-13 shows a SPM image of the indent array taken using the

nanoindenter. The relief on the surface is due to the arrangement of the martensite variants. As will be shown in section 4.4.2.2, the surface relief disappears as the film is heated to the high-temperature austenite phase.

Figure 4-14 displays the results of the nanoindentation test on the commercial  $\text{Ni}_{50}\text{Ti}_{50}$  film. The reduced modulus as a function of contact depth is fairly constant. The scatter in the data can be attributed to the surface relief of the martensite variants. The constant modulus as a function of indent depth is the expected result for a homogeneous film, where the contact depths are less than 10% of the film thickness. It should be noted that the maximum indentation depth is on the border of the 10% rule and that deeper indents would be expected to begin showing a stiffer response as the Si substrate ( $E \sim 170$  GPa) is approached [37].

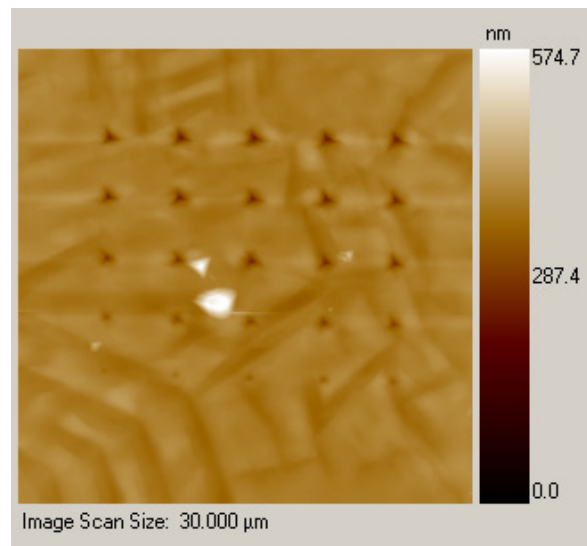


**Figure 4-13.** Nanoindentation SPM image of a nanoindentation array on a commercial  $2 \mu\text{m}$   $\text{Ni}_{50}\text{Ti}_{50}$  film on a Si substrate. The relief on the surface of the films is due to the arrangement of the martensite variants.

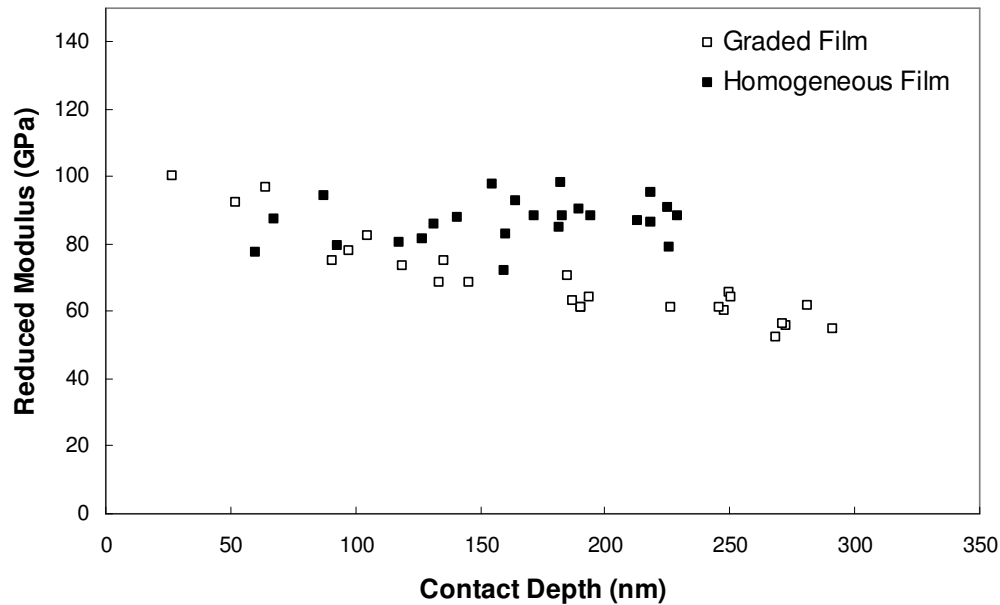


**Figure 4-14.** Reduced modulus as a function of contact depth for a 2  $\mu\text{m}$   $\text{Ni}_{50}\text{Ti}_{50}$  film on a Si substrate. The results are compared to indentation results on a graded 400 nm  $\text{Ni}_{47}\text{Ti}_{53}$  film on a  $\text{Ni}_{56}\text{Ti}_{44}$  substrate.

For comparison, the results of a test on a graded 400 nm  $\text{Ni}_{47}\text{Ti}_{53}$  film on a  $\text{Ni}_{56}\text{Ti}_{44}$  substrate is also included in Figure 4-14. The modulus of the graded film decreases as the indentation depth increases. This is a combined result of a gradient in mechanical properties in the film, substrate effects and mechanically induced phase transformations that occur during indentation. This relatively complex result will be discussed in detail in the following sections devoted to nanoindentation of graded SMA films.

#### 4.2.2. Nanoindentation of Graded SMA Films on NiTi Substrates

The hardness and elastic modulus of the films, at various depths relative to the film-substrate interface, were measured using nanoindentation. A 40  $\mu\text{m}$  x 40  $\mu\text{m}$  area located near the center of the film was first imaged using SPM to ensure that the measurements were made on a relatively flat area. Indents were

made in an 8 x 8 grid, increasing the peak load for each successive measurement, as described in the experimental nanoindentation section. Figure 4-15a show an SPM images of a  $\text{Ni}_{47}\text{Ti}_{53}$  film on a polished  $\text{Ni}_{56}\text{Ti}_{44}$  substrate, after the indentation process. The roughness of the film is slightly higher than the films sputtered onto the silicon substrate ( $\sim 40$  nm) (Figure 4-15b), due to the limitations of the mechanical polish ( $\sim 50$  nm versus the initial  $\sim 5$  nm roughness of the Si substrate). There is also evidence of the martensite variants seen in the commercial film. As a result, the data will be more scattered in the former case because a number of the indents will be on the side of a relative hill or valley.

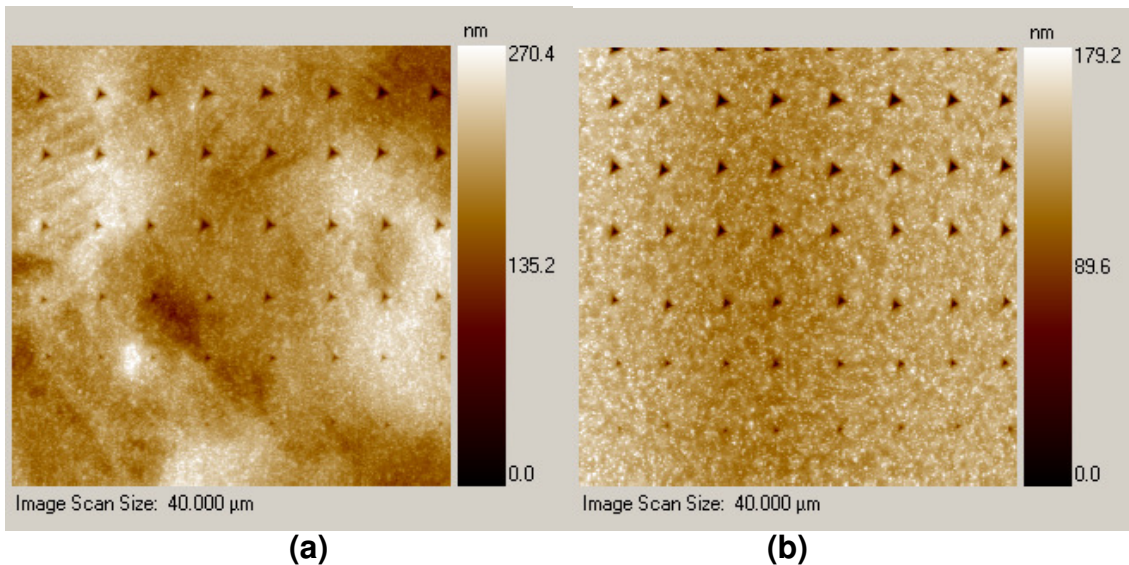


**Figure 4-15.** SPM image of an annealed 800 nm  $\text{Ni}_{47}\text{Ti}_{53}$  film on a (a) polished  $\text{Ni}_{56}\text{Ti}_{44}$  ribbon and (b) a Si substrate. Note the presence of martensite variants and greater roughness associated with the surface of the film on the polished ribbon.

To determine the elastic modulus of the films, equation 4 was used. The Poisson's ratio of the film and tip were assumed to be 0.3 and 0.07, respectively, while the modulus of the tip was assumed to be 1141 GPa [65]. The elastic modulus as a function of contact depth can be seen in Figure 4-16 for amorphous films of varying thickness. Figure 4-17 displays the results for films

annealed at 575 °C for 40 min. The graded films show a more compliant response as the indentation depth increases. This is due to substrate effects as well as the variations in the composition, crystal structure and thus the mechanical properties of the film. As for the unannealed (amorphous) films, the trend of decreasing elastic modulus with increasing indentation depth is likely due to substrate effects alone. However, the data appear to show a related response, suggesting that the measurement on films of varying thickness may be self-similar. The distance to the film-substrate interface is the fundamental difference between the films of varying thickness. This information will be used in the subsequent sections to characterize the extent of the graded interface via the thickness-normalized parameter,  $h^*$ , previously defined in equation 9.

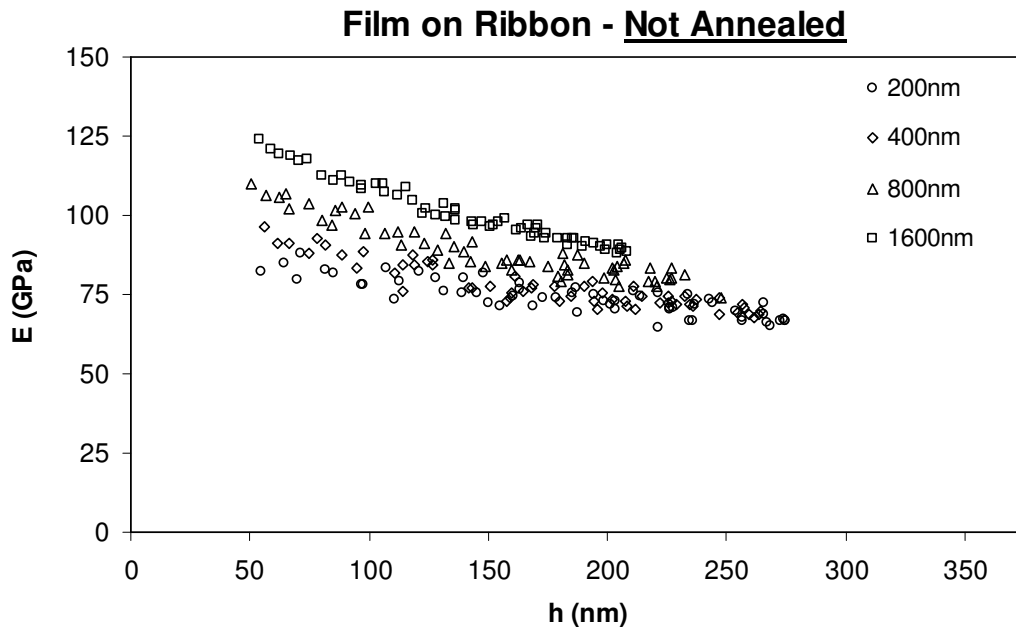


**Figure 4-16.** Elastic modulus as a function of contact depth for an amorphous  $\text{Ni}_{47}\text{Ti}_{53}$  film on a  $\text{Ni}_{56}\text{Ti}_{44}$  substrate.

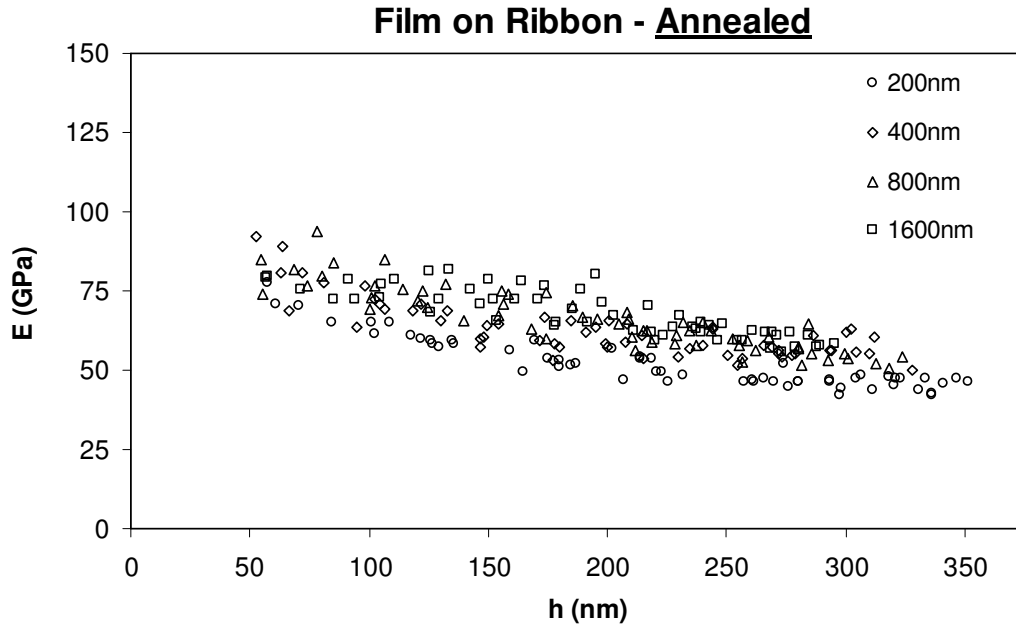


**Figure 4-17.** Elastic modulus as a function of contact depth for a  $\text{Ni}_{47}\text{Ti}_{53}$  film on a  $\text{Ni}_{56}\text{Ti}_{44}$  substrate that was annealed at 575 C for 40 minutes.

#### 4.2.3. Characterization of Graded Interface of Modified NiTi Substrate

The diffusion interface of graded SMA films was characterized by studying the indentation response of  $\text{Ni}_{56}\text{Ti}_{44}$  substrates modified with  $\text{Ni}_{47}\text{Ti}_{53}$  films. Figure 4-18 and Figure 4-19 display the results of the nanoindentation tests on films of varying thickness for the samples before annealing and after annealing. The elastic modulus and hardness are plotted as a function of normalized contact depth,  $h^*$ , according to equation 9. Here  $h_c$  is the contact depth of indentation and  $t$  is the film thickness before annealing. All of the films become more compliant as the indentation depth increases and substrate contributions become more prevalent. The trend is less severe in the annealed case due to the lesser elastic modulus mismatch between the crystallized film and substrate.



The challenge in interpreting the indentation curves is to differentiate the indentation behavior of the film from that of the substrate. It is anticipated that an austenite-rich film will be stiffer than the substrate because the austenite phase is 2-3 times stiffer than the martensite phase. Annealing the substrate also causes the elastic moduli to drop by approximately 10 GPa due to the recrystallization of the highly stressed structure in the as-received substrate. The heat treatment also causes the average hardness of the bare substrate to decrease by approximately 1 GPa over the same range of contact depths. The hardness decreases with respect to increasing indentation depth which is likely due to both indentation size effects and substrate effects.

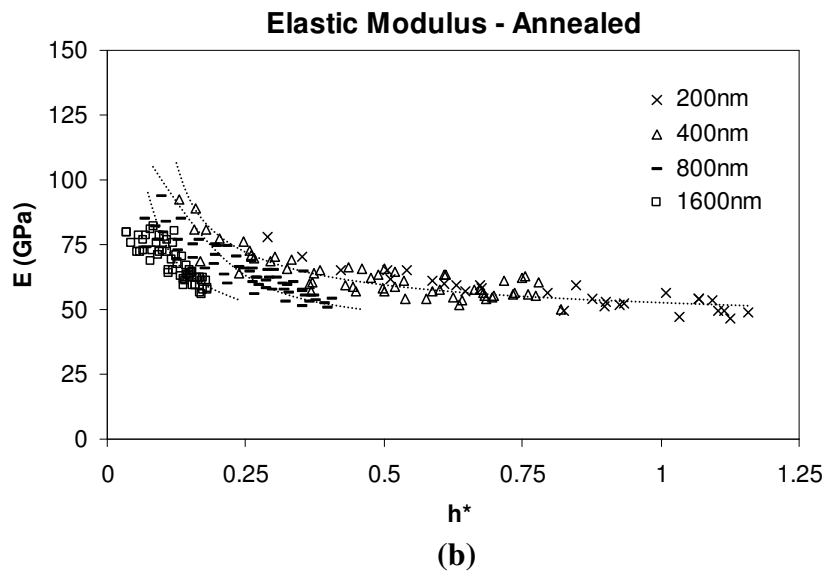
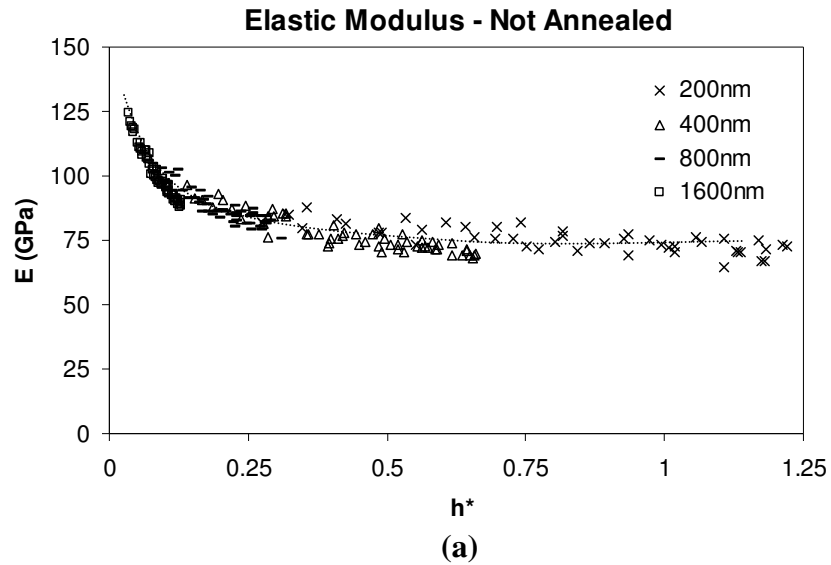


**Figure 4-18.** Elastic modulus as a function of normalized contact depth for (a) amorphous films as deposited, and (b) crystallized films after annealing.  $h^*$  is the normalized contact depth given in Equation 9. Note that the self-similarity breaks for the 800 nm and 1600 nm annealed films.  $h^* < 1$  corresponds to contact depths less than the film thickness. Trends in the data are indicated by dotted lines.

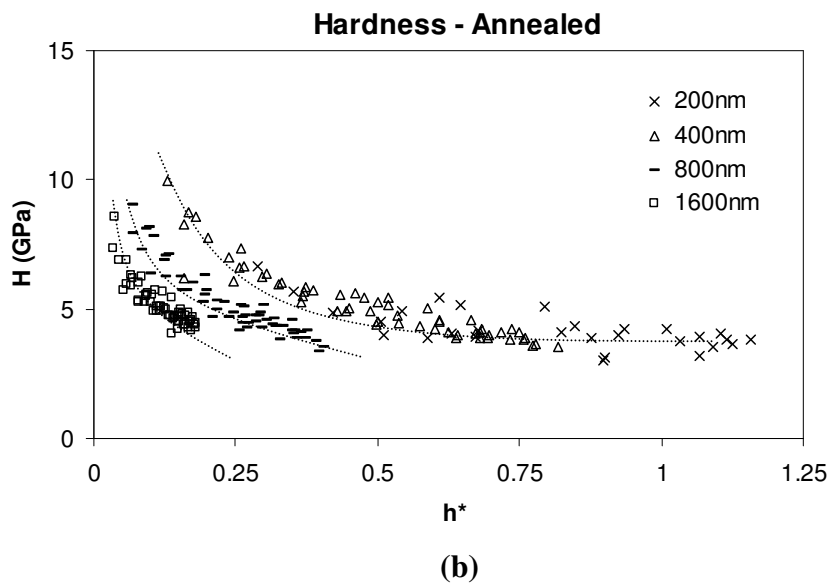
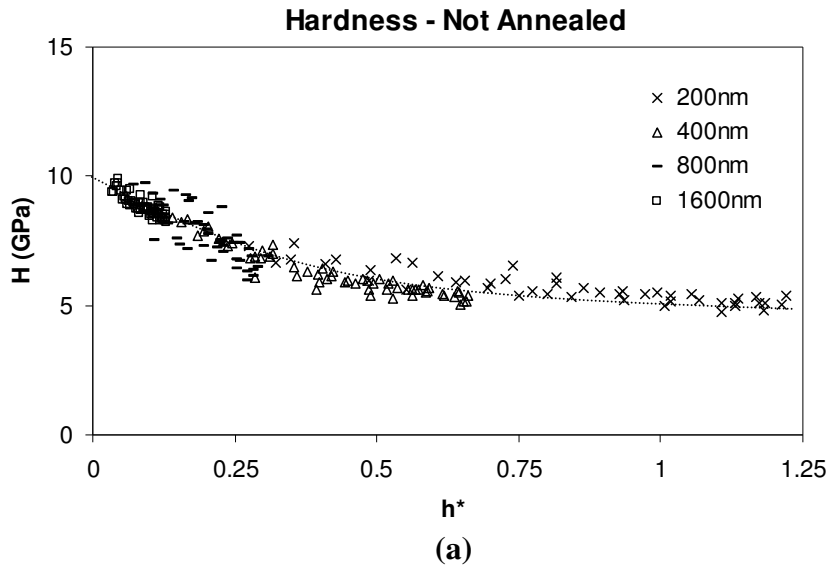


**Figure 4-19.** Hardness as a function of normalized contact depth for (a) amorphous films as deposited, and (b) crystallized films after annealing.  $h^*$  is the normalized contact depth given in Equation 9. Note that the self-similarity breaks for the 800 nm and 1600 nm annealed films.  $h^* < 1$  corresponds to contact depths less than the film thickness. Trends in the data are indicated by dotted lines.

Residual stresses due to the inhomogeneity that exists between the film and substrate may also complicate the indentation response by modifying the resistance of the material to deformation [90, 91]. However, the effect is

estimated to be well below the plateau stress level for martensite and austenite due to similarities in the properties and composition of the film and substrate [13]. As discussed earlier, the diffusion process is also anticipated to reduce the level of residual stress even further as an equilibrium state is approached via the compositional gradient.

Before heat treatment, the data from the films of varying thickness all lie along the same curve. The hardness and elastic modulus data for all non-annealed films are self-similar because the measurements are a response from two layer systems (amorphous film and bulk substrate). After heat treatment, the 200 nm and 400 nm films fall along the same curve but this self-similarity deviates for the two thicker films. This can be attributed to the creation of a third layer at the surface of the film that is stiffer and harder than the substrate (Figure 4-20). The time allowed for annealing is insufficient for the diffusing species from the substrate to reach the surface of the 800 nm and 1600 nm films. This effectively creates a three-layer system consisting of the bulk substrate, an intermediate graded layer, followed by a homogeneous crystallized layer [92].

A diffusion coefficient  $D$  can be estimated using dimensional analysis with the characteristic length as the approximate thickness at which the self-similarity of the annealed films deviate ( $l \approx 500$  nm) and the characteristic time as the annealing time at the maximum temperature ( $t \approx 2500$  s)

$$D = \frac{l^2}{t} = 1 \times 10^{-16} \frac{m^2}{s} \quad 14$$

This value is consistent with reported diffusion coefficients for similar NiTi systems [93-96]. Assuming an Arrhenius relationship,

$$D = D_o \exp\left(\frac{-Q}{k_B T}\right) = 3.7 \times 10^{-16} \frac{m^2}{s} \quad 15$$

Here we use the pre-exponential factor  $D_o = 2 \times 10^{-7} \text{ m}^2 \text{ s}^{-1}$  and the activation energy  $Q = 142 \text{ kJ} \cdot \text{mol}^{-1}$  reported by Bastin *et al.*, where  $k_B$  is the Boltzmann constant ( $1.38 \times 10^{-23} \text{ J} \cdot \text{K}^{-1}$ ) and  $T$  is the annealing temperature (850 K).

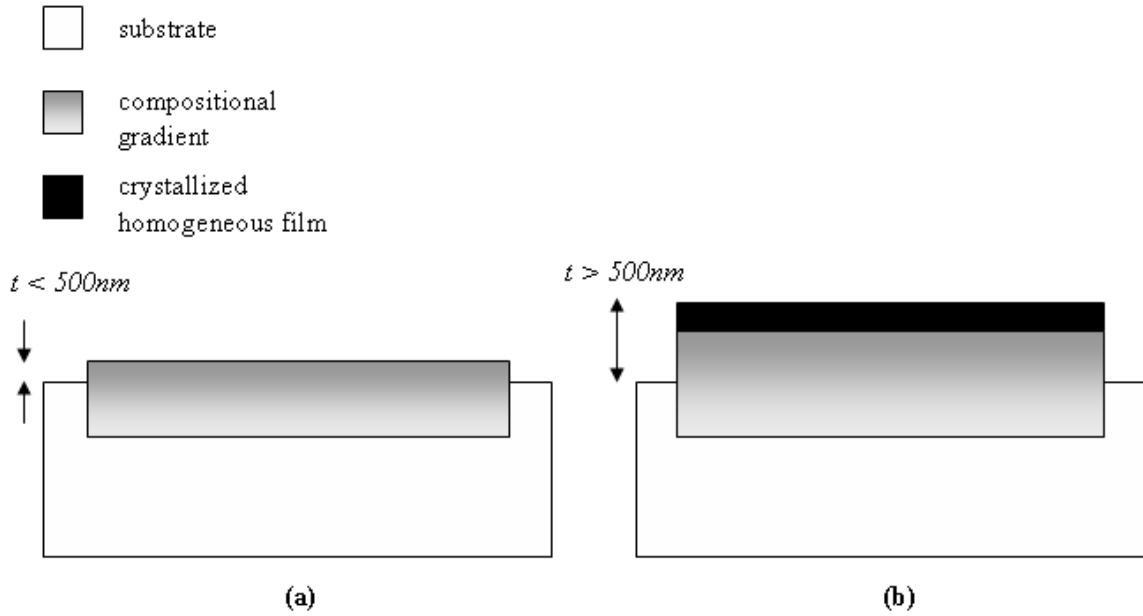


**Figure 4-20.** Schematic of graded annealed film (a) less than 500 nm and (b) greater than 500 nm. Note the presence of a third homogeneous layer in (b) that results from an annealing time insufficient for diffusing species to reach the surface of the film.

This result highlights the strength of the diffusion modification technique developed in this work to process graded SMA films. A film is deposited onto another film or onto a bulk surface of a dissimilar elemental composition. The film thickness and annealing parameters (time and temperature) will control the characteristics of the graded interface resulting from the diffusion process. In this way, films can be designed with specific gradients, tailored for a specific

application. The diffusion interface can then be characterized using the nanoindentation technique described above.

### **4.3. Modeling of Nanoindentation Response in Graded SMA Films**

#### **4.3.1. Determining the Extent of the Composition Gradient due to Diffusion Modification**

The self-similarity of the indentation response of the films was modified to model gradient effects in order to characterize the extent of the graded interface [97]. However, the response itself is a complicated function of the gradient in mechanical properties, substrate effects and mechanically induced phase transformations. In order to better understand the similarity of a two-layer system, the scaling law was modified to account for the movement of the film-substrate interface due to diffusion as follows:

$$h^* = (h_c + \gamma^*(t - d_2))/(t + d_1) \quad 16$$

where  $d_1$  is a shift factor for the thickness that is related to the diffusion of the film-substrate interface into the substrate,  $d_2$  is a shift factor for the indentation depth related to the diffusion of the film-substrate interface into the film (see Figure 4-21).  $\gamma$  is a coefficient that scales the relative contribution of the unmodified portion of the film,  $t - d_2$ , to the indentation response.

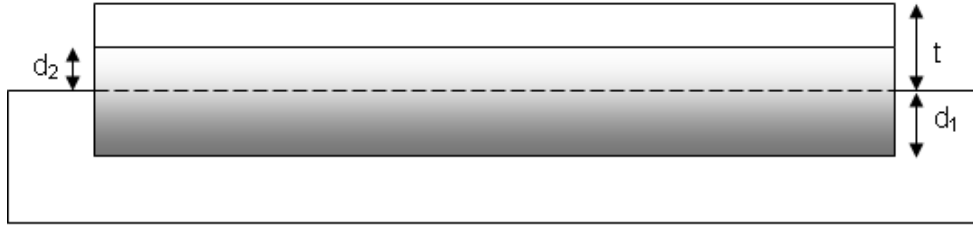


**Figure 4-21.** Schematic of diffusion interface in graded film as a result of the annealing process.

The results obtained from the modified form of the scaling law in equation 16 for the annealed films can be seen in Figure 4-22 using a shift factor  $d_1$  of 1000 nm, a shift factor  $d_2$  of 600 nm and a scaling factor  $\gamma$  of 0.1 that “collapses” the data onto a single curve.  $d_1$  and  $d_2$  are not equal due to the different rates of diffusion of Ni-rich NiTi into Ti-rich NiTi in relation to the diffusion of a Ti-rich NiTi into Ni-rich NiTi. The shift factor  $d_2$  provided a quantitative way to characterize the graded interface.

The curve in Figure 4-22 can be described using a power law, which tends toward a substrate modulus of 38 GPA. The power-law fit describes the effects of the compositional gradient on the nanoindentation behavior of the SMA films when the film-substrate interface propagates 1000 nm into the substrate. The self-similarity principle permits the mechanical properties of the graded SMAs to be resolved further into substrate, beyond the contact depth of the indenter probe.

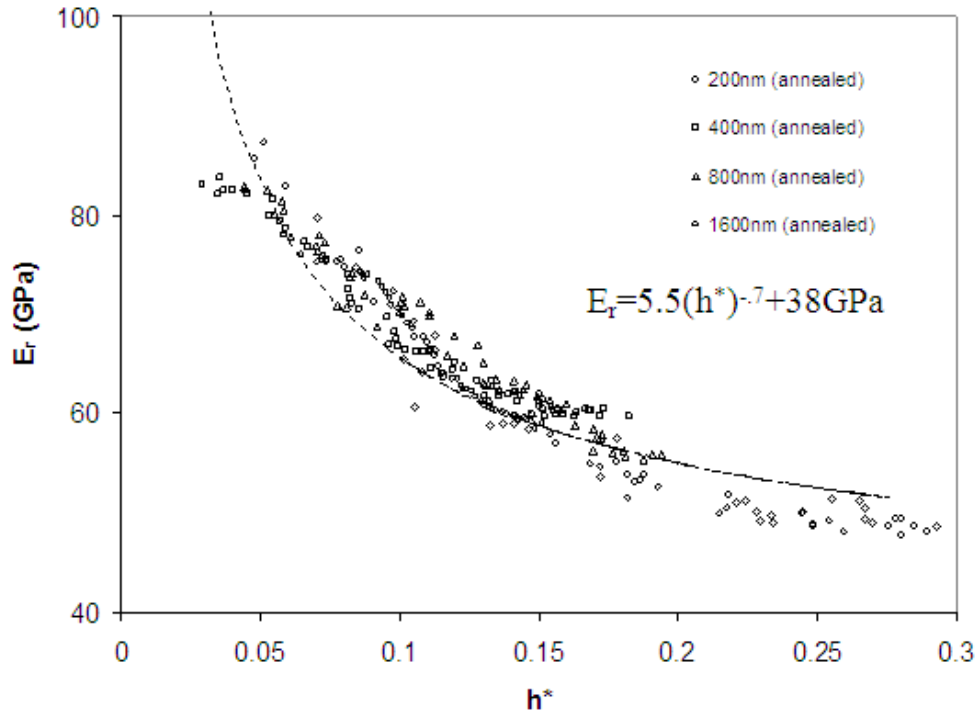


**Figure 4-22.** Elastic modulus as a function of indentation depth after normalizing each film thickness using the modified self-similarity formula in Equation 16.

#### 4.3.2. Predicting the Nanoindentation Response on Graded Films

While the modified scaling principle is capable of relating the diffusion modification for films of varying thickness, it does not predict the nanoindentation response due to the compositional gradient. For that, it is necessary to perform a more detailed analysis that accounts for the combined response of the gradient in properties of the film as well as the properties of the substrate. Saha and Nix developed a model that was used to predict the elastic response of a homogeneous, non-active film on an elastically mismatched substrate (see Equation 10). This analysis permits the measurement of the film at contact depths up to  $0.5t$ , a substantial increase beyond the  $0.1t$  limit that is commonly used. To apply Equation 10, constant properties are assumed throughout the



thickness of the film. In the case of a graded film, the properties must be considered at each point below the tip. In addition, the austenite phase may undergo an isothermal transformation underneath the tip upon being subjected to a critical stress. This is important because the measurement is taken during unloading, at which point the elastic properties have been changed from their initial state.

The Saha/Nix analysis was modified to account for a graded and active structure. In order to use Equation 10, it was necessary to determine the extent of the transformed film. From previous research, the indentation of a homogeneous phase-transforming film can be divided into a transformed region and an untransformed region using Equation 1 [34]. Within the transformed region, the modulus of the film is expected to be equivalent to the transformed phase, while outside this region it is determined by the property gradient in the film (see Figure 4-23).

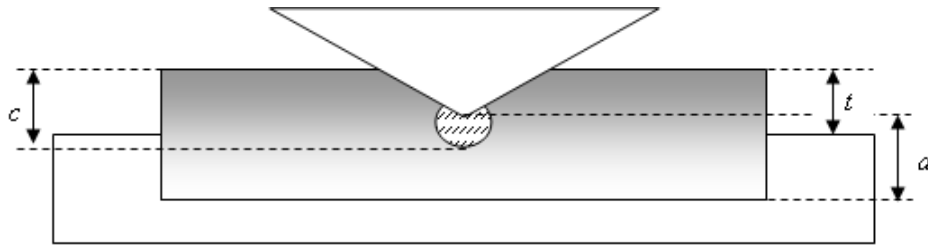


**Figure 4-23.** Schematic of the indentation of a graded and actively transforming film.

The elastic indentation behavior of the bare substrates and graded films were described by taking,

$$\frac{d}{dz} \left( \frac{1}{E_r} \right) = (1 - \nu_f^2) \cdot \left( \frac{1}{E_s} - \frac{1}{E_f} \right) \cdot \frac{d}{dz} \left( e^{\frac{-\alpha(d-h)}{a}} \right) \quad 17$$

and then integrating from the substrate as follows,

$$\frac{1}{E_r(h)} = \int_d^h (1 - \nu_f^2) \cdot \left( \frac{1}{E_r(z')} - \frac{1}{E_f(z')} \right) \cdot \frac{d}{dz} \left( e^{\frac{-\alpha(d-h)}{a}} \right) dz' + \frac{1}{E_r(d)} \quad 18$$

As stated previously, the properties of the film between the indenter and the transformation interface,  $c$ , are taken to be that of the transformed phase, while the properties between the interface and the interface between the film and substrate are those associated with the gradient microstructure. For simplicity, the analysis is applied in one-dimension, normal to the surface of the film.

The analysis was first verified by applying equation 18 to a passive (i.e., no phase transformations occur under the tip during loading) copper-nickel multilayer film on a silicon substrate. The specimen consisted of 10 alternating layers of Cu and Ni, beginning with a Cu layer, with each film approximately 50 nm thick (see Figure 4-24).

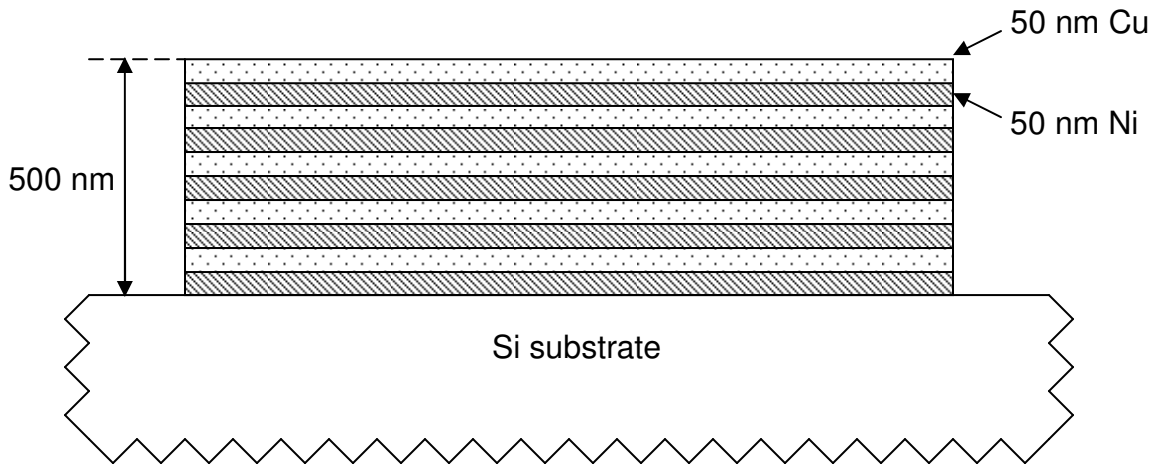


**Figure 4-24.** Schematic of the multilayer Cu-Ni film, which consisted of alternating 50 nm layers deposited onto a Si substrate.

The Cu-Ni system was chosen because the elastic properties between the two materials are sufficiently different to cause the indentation response to vary

as a function of depth. To predict the indentation response, an elastic modulus of 135 GPa and 210 GPa were used for the Cu and Ni layers, respectively, while an elastic modulus of 170 GPa was used for the Si substrate [98, 99]. Infinitely sharp interfaces were assumed to exist between the layers since a negligible amount of diffusion was expected to occur at room temperature (temperature at which the films were processed). The specimen was indented in the same manner as the approach taken for the graded films, with the peak load varying at different spatial locations while maintaining a constant loading rate.

The results of the nanoindentation test, the initial elastic distribution and the predicted elastic response can be seen in Figure 4-25. The initial indents below 50 nm are dominated by the first Cu film, but the response becomes stiffer as the contact depth increases and the first Ni film becomes more significant. The scatter in the data below 50 nm can be attributed to tip effects, which typically occur for indents less than 1/3 of the radius of curvature of the probe (150 nm berkovich tip). The response becomes more compliant as the Ni film is penetrated and the second Cu film becomes more dominant. The elastic response overall tends closer to the properties of Cu rather than Ni, because the top film was a Cu layer.

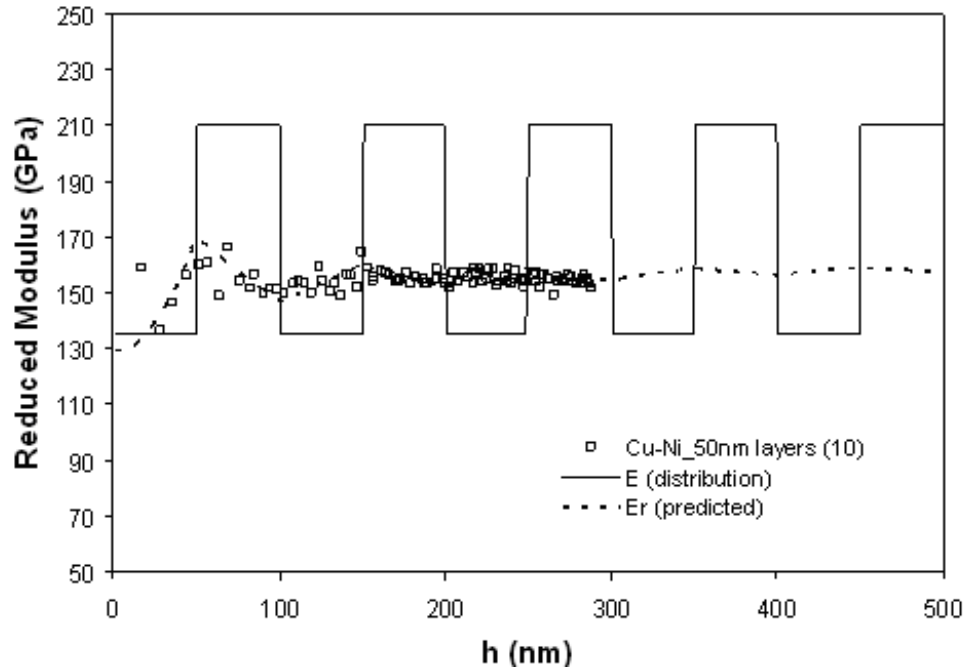


**Figure 4-25.** Results of indentation test on a multilayer Cu-Ni film on Si substrate. The film consisted of 10 alternating 50 nm layers of Cu and Ni. The plot also includes the initial elastic distribution and the predicted indentation response.

The analysis predicted the indentation response on the passive film system well, so equation 18 was then applied to the active graded SMA films. For the bare substrate, the film-substrate interface coincides with the transformation interface. A modulus of 38 GPa was used for the transformed phase, and a modulus of 75 GPa, and transformation stress of 400 MPa was used for the untransformed substrate in a partially-austenitic state. To apply Equation 17 to the graded SMA films, it was also necessary to account for the initial compositional gradient in the films. Therefore, the results from the following equation for the diffusion lengths were used to determine the compositional gradient on either side of the initial interface using the classical diffusion solution for a bi-material interface:

$$\frac{C(x) - C_o}{C_s - C_o} = 1 - \operatorname{erf}\left(\frac{x}{2\sqrt{D \cdot \tau}}\right) \quad 19$$

Here,  $C_s$  is the average composition at the interface,  $C_o$  is the composition away from the boundary at distance  $x$  from the initial interface,  $D$  is the diffusion coefficient on the side of the interface at the annealing temperature  $T$ , and  $\tau$  is the annealing time. A previous study indicated that the diffusion rate was similar to other NiTi systems that assume an Arrhenius relationship with a coefficient of  $2 \times 10^{-7} \text{ m}^2 \text{ s}^{-1}$  and activation energy of  $142 \text{ kJ} \cdot \text{mol}^{-1}$ . The results are consistent with the shift factors used in Equation 16.

Using the composition gradient from Equation 19, it is then possible to utilize the relationship between films with homogeneous compositions and the annealed structure of the homogeneous films to determine the initial variation of the untransformed modulus,  $E$ , with respect to depth,  $z$ , and martensite volume fraction,  $\xi$ , via a classical Rule-of-Mixtures Formulation [100]:

$$E(\xi(z)) = E_A + \xi(z)(E_M - E_A) \quad 20$$

where  $E_A$  is the modulus of austenite, and  $E_M$  is the modulus of martensite. The resulting initial variation of the martensite volume fraction with film depth after annealing can be seen in Figure 4-26, while the corresponding elastic modulus distribution calculated from Equation 20 can be seen in Figure 4-27.

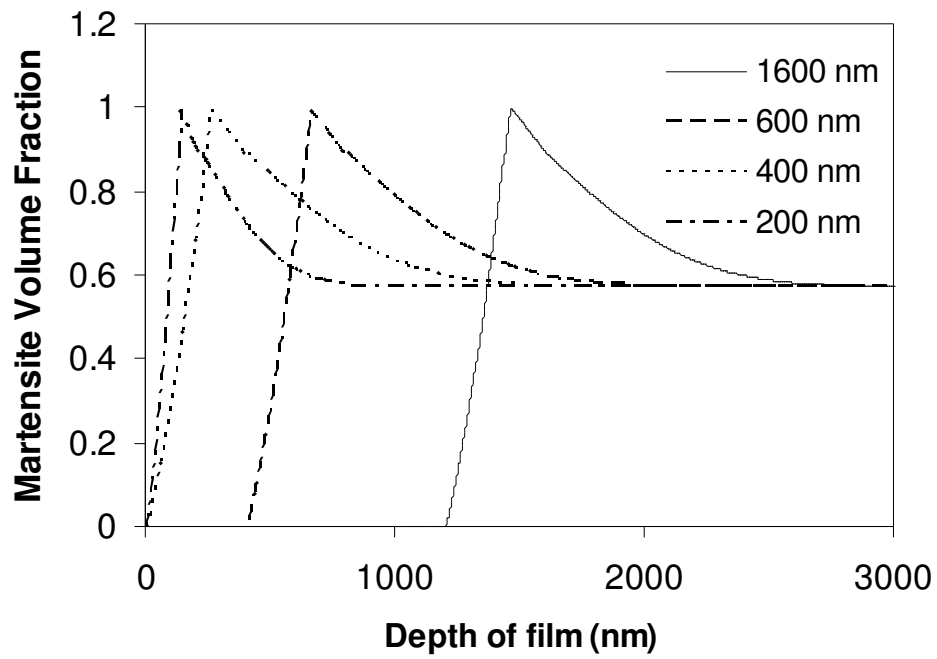


**Figure 4-26.** Initial distribution of martensite in the film as a result of the composition gradient.

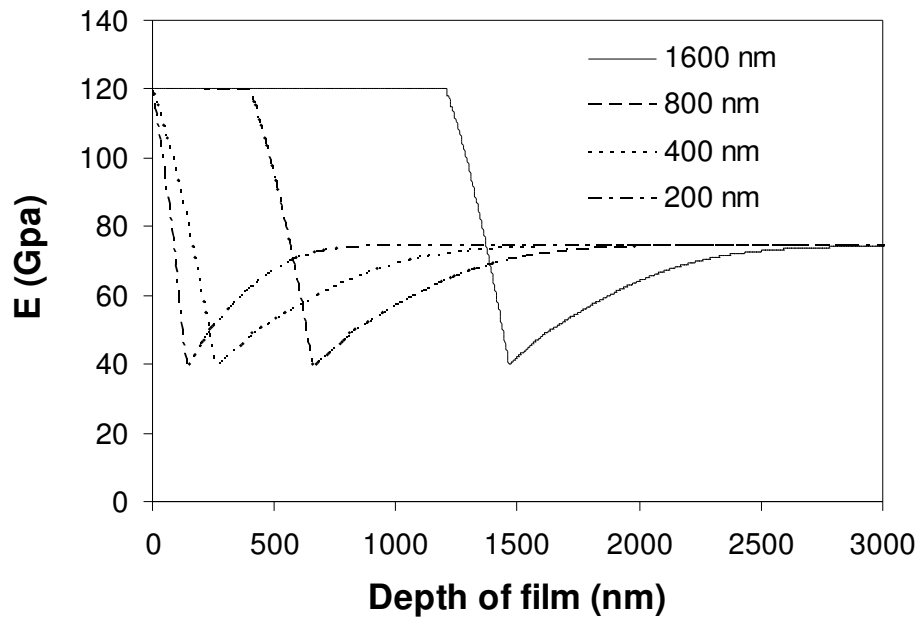


**Figure 4-27.** Corresponding expected elastic modulus in film as a result of composition gradient.

A similar prediction can also be made for the transformation stress. The predicted reduced modulus as a function of contact depth can be seen in Figure

4-28. Note that the untransformed phase of the film is stiffer than the substrate, corresponding to a value of 120 GPa, the modulus associated with the fully austenitic state, and also indicates that the substrate is not fully austenitic. The transformation properties of the homogeneous films were also found to have a dependence on the martensite volume fraction similar to those reported for NiTi thin films by LExcellent *et al* [101]. The predicted fits using Equation 18 correlated well with the experimental data.

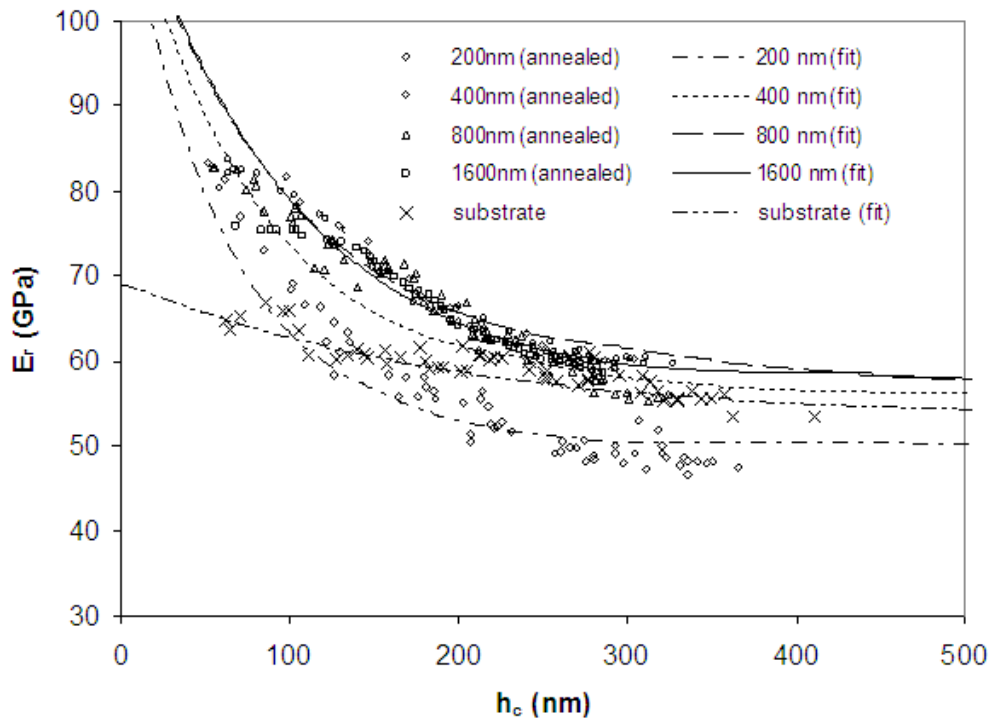


**Figure 4-28.** Reduced modulus variation with respect to indentation depth determined using the modified Saha/Nix equation and the initial properties determined from the martensite volume fraction in Figure 4-26.

## 4.4. Characterizing Recovery of Deformation in SMA Films

### 4.4.1. *A posteriori* Nanoindentation SPM characterization of recovery after heating: Characterizing one-way SME

To explore the effects of self-assembled material gradients on the film's SME, the recovery of deformation from indentation was characterized *a posteriori* after heating [34]. Figure 4-29 shows an indent targeted for shape memory measurements. The sample tested was an annealed 1  $\mu\text{m}$   $\text{Ni}_{47}\text{Ti}_{53}$  film on a Si (100) substrate. A height profile was taken across the deepest section of the Berkovich indent.

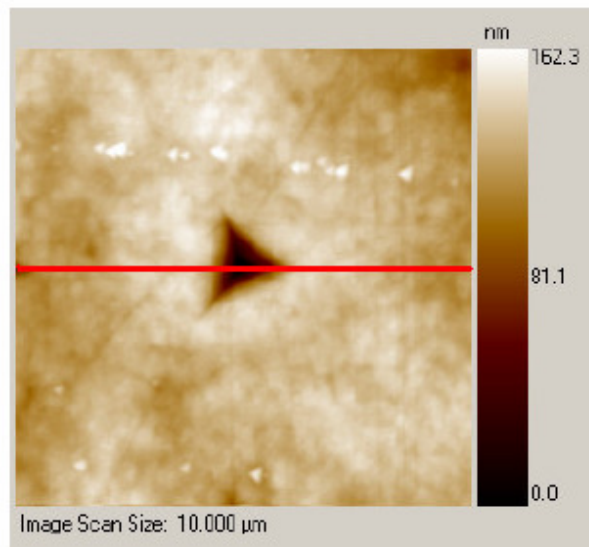


**Figure 4-29.** SPM image of an annealed 1  $\mu\text{m}$   $\text{Ni}_{47}\text{Ti}_{53}$  film on a Si (100) substrate taken using the nanoindenter. A height profile of the image was taken across the deepest portion of the indent.

The sample was heated in a furnace, replaced in the nanoindenter, and rescanned. The same line across the deepest portion of the indent was again targeted and the change in the height profile was observed. The results for the various heat treatments can be seen in Figure 4-30.



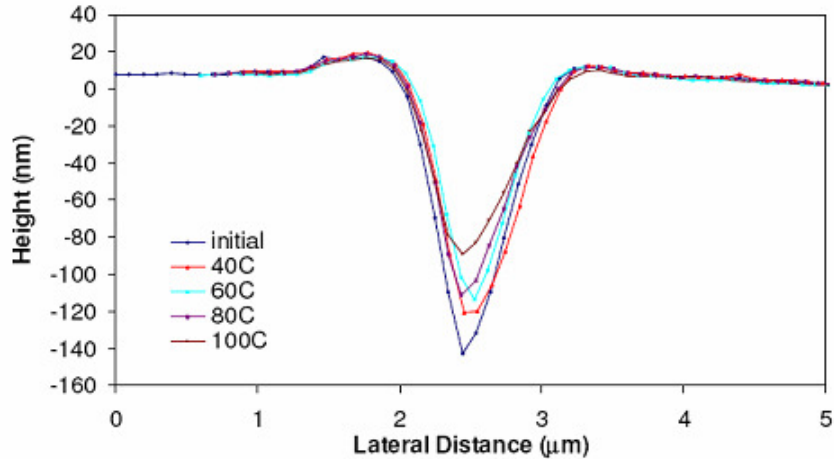


**Figure 4-30.** Height profile taken from a SPM image of an annealed 1  $\mu\text{m}$   $\text{Ni}_{47}\text{Ti}_{53}$  film on a Si (100) substrate after various heat treatments.

Note that the units on horizontal and vertical axes are not the same. The actual indent is significantly shallower than it appears in the figure. The data are displayed in this way to emphasize the change in the maximum depth of the indent. The recovery of deformation  $R$  was established by calculating the change in the average height relative to the initial indent  $\Delta h$ , and then dividing by the average height of the initial indent  $h_i$ .

$$R = \frac{\Delta h}{h_i} \quad (21)$$

The average height of the indent refers to the vertical distance between bottom of the indent and the average height of the right and left corners of the top of the indent. Changes in the horizontal aspects of the indent were neglected. A summary of the recovery measurements for the various heat treatments can be seen in Figure 4-31.

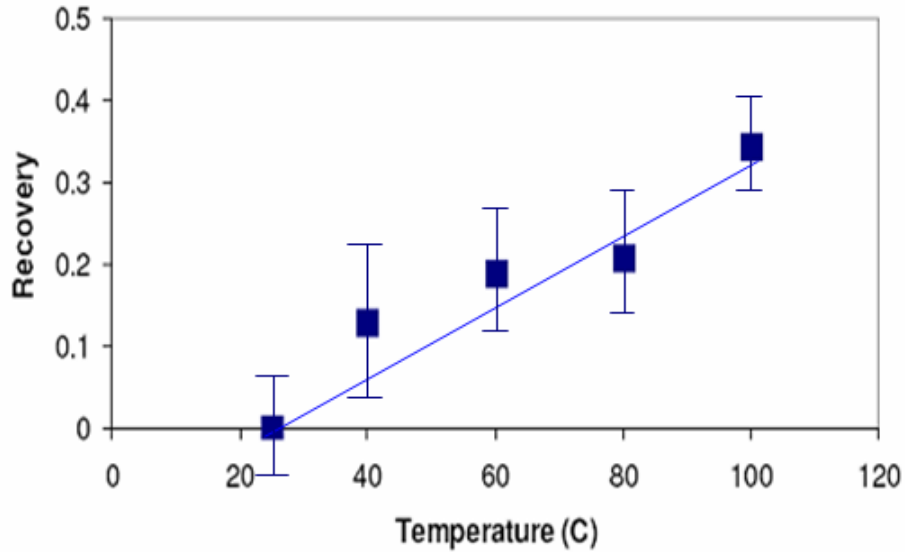


**Figure 4-31.** Recovery of initial deformation as a function of heat treatment temperature for an annealed 1  $\mu\text{m}$   $\text{Ni}_{47}\text{Ti}_{53}$  film on Si (100) substrate. The final recovery was found to be approximately 35%.

The initial scan was performed immediately following indentation at room temperature. The indent was scanned a second time to find the recovery at room temperature; the initial recovery was found to be essentially zero, as expected. Subsequent scans were performed after removing the sample, heating it in a furnace, replacing the sample in the nanoindenter, and finding the indent of interest. The first heat treatment of 40°C produced a recovery of approximately 0.15. The heat treatment of 60°C produced a recovery of approximately 0.20, while the next treatment at 80°C generated very little additional recovery. The last heat treatment at 100°C yielded a final recovery of approximately 0.35.

In previous studies with titanium-rich nitinol films, Wibowo et al. showed that an increase in titanium content from the equiatomic composition resulted in an increase in the transformation temperature [53]. At a composition of 51.7%

titanium, the transformation temperature was approximately 45 °C. Therefore, we expect the 53% titanium films used in this study to have a transformation temperature above 45 °C. It should also be noted that the recovery measured using this method was permanent. Tests performed on compositionally-graded SMA films showed no apparent recovery because the recovery was realized in the furnace, while the scans were run at room temperature where the indents had possibly reformed. Therefore, this technique is limited to characterizing films that display the one-way SME. This limitation will be addressed in the following section where a method for characterizing recovery *in situ* is discussed.

Besides the inherent limitation to testing one-way SMA films, there are two other main difficulties with this experimental approach. One limitation in this method is the size of the indenter tip. The radius of curvature of the Berkovich tip used in this study is approximately 150 nm. Therefore, the images taken with the nanoindenter tip will be a function of the size and geometry of the Berkovich probe. This limits the amount of information that can be found using this technique. The second challenge with this approach is the rotation of the indent with respect to the probe that occurs when the sample is removed for heat treatments and then replaced for subsequent scans. The Berkovich tip geometry will cause a deviation in the apparent indent depth if the sample is not aligned consistently. This method can be improved upon by scanning the indents with a smaller probe. This will improve the accuracy of the height measurements as the tip will be able to trace the indents with much higher accuracy. Using an

axisymmetric tip will make imaging less dependent on the orientation of the sample with respect to the indenter.

#### **4.4.2. AFM with *In Situ* Heating: Characterizing Two-Way SME**

The inherent limitations with the original technique were improved by using an atomic force microscope with an integrated heating stage [102, 103]. This enhanced method reduced or eliminated several deficiencies with the originally proposed technique. First, the accuracy associated with the new technique was greatly improved due to the reduction in tip size. The radius of curvature of the AFM probes used was approximately an order of magnitude smaller than the radius of the nanoindenter tip. Second, the error involved in imaging with the asymmetric nanoindenter probe was eliminated with the use of the symmetric conical AFM probe. Third, the *in situ* capability of the improved technique eliminated the potential errors associated with physically handling the specimens several times per experiment. This prevented the indent array from rotating and also avoided wear on the specimens. Lastly, the *in situ* capability of the AFM technique expanded the amount of information made available during the measurement.

The original method was limited to gathering information at room temperature; this is sufficient for observing the final recovery of the indent, which is important for characterizing the one-way SME. However, this method fails to detect phenomena associated with the two-way SME because information about the indent height at any point other than room temperature is unavailable. For example, a film that displays a perfect two-way SME, that is, the indent recovers

a certain percentage of the original deformation at a higher temperature, but returns to its original height at room temperature, would appear to be a standard passive material. The improved method allows for the recovery to be observed at each temperature interval, allowing the two-way SME to be characterized.

#### 4.4.2.1 Calibration of New *in situ* Technique using Gold Films

The indent array in the gold film first tested to ensure that the observed recovery in subsequent tests on the active films was solely due to the SME and not an artifact of the AFM measurement. Figure 4-32 displays the indent array in the gold reference sample at 300 K.

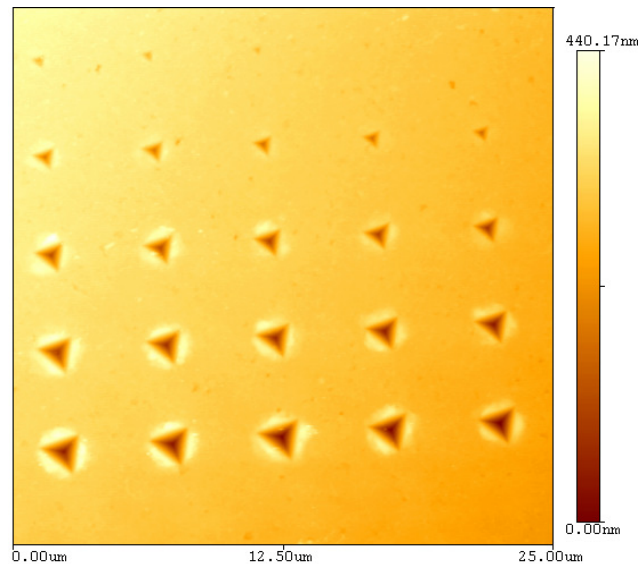


**Figure 4-32.** AFM scan of indent array in Au film. The scan area is 25 μm by 25 μm.

The recovery of the indents was defined as

$$R = \frac{h_i - h}{h_i} \quad (22)$$

where  $h_i$  was the initial maximum indent depth and  $h$  was the current maximum indent depth. Figure 4-33 shows the results of the recovery tests on the passive

reference sample. As expected, the data showed no clear trends over the tested temperature range. The measured recovery varied largely between +/- 5%.

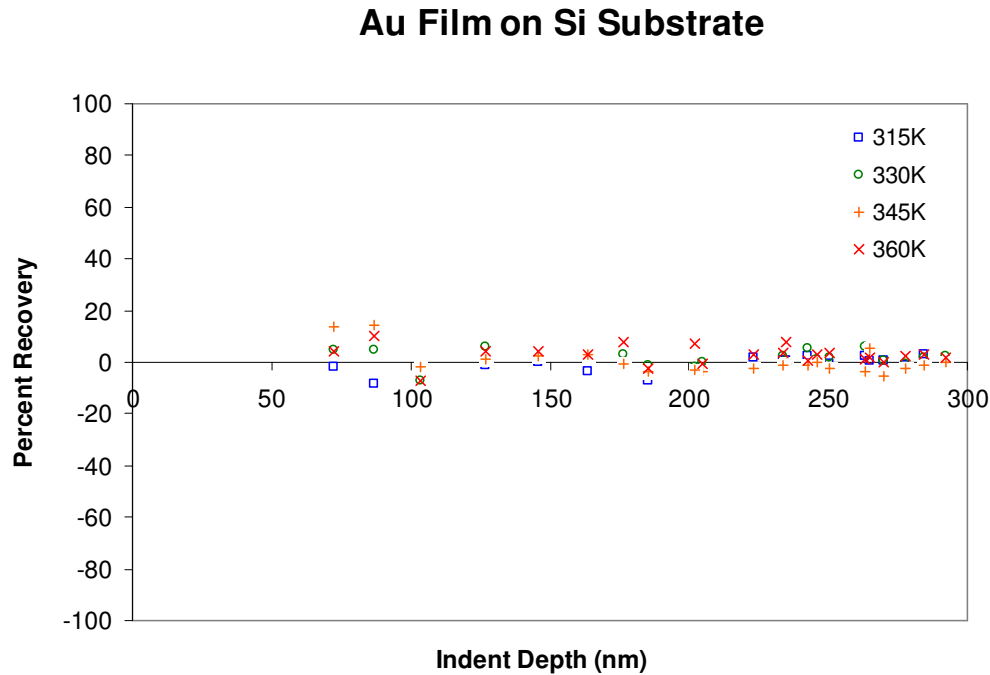


**Figure 4-33.** Recovery as a function of indent depth in a gold film for the temperature range tested for the active materials.

The recovery for indents less than approximately 100 nm was more scattered because the uncertainty in the measurement is magnified by the way the recovery is being defined. The recovery tests on the passive film also provided a general idea for the error associated with the measurement (~5-10%).

#### 4.4.2.2 Applying *in situ* Technique to Active Films

The negligible recovery observed in the passive films justified the use of the method for characterizing the SME in actively-transforming films [104]. Figure 4-34 shows AFM scans of the homogeneous NiTi film in the low-temperature martensite state and the high-temperature austenite state. Surface

relief of the martensitic variants on the surface was apparent at 300 K, due to the stress caused during the annealing process.

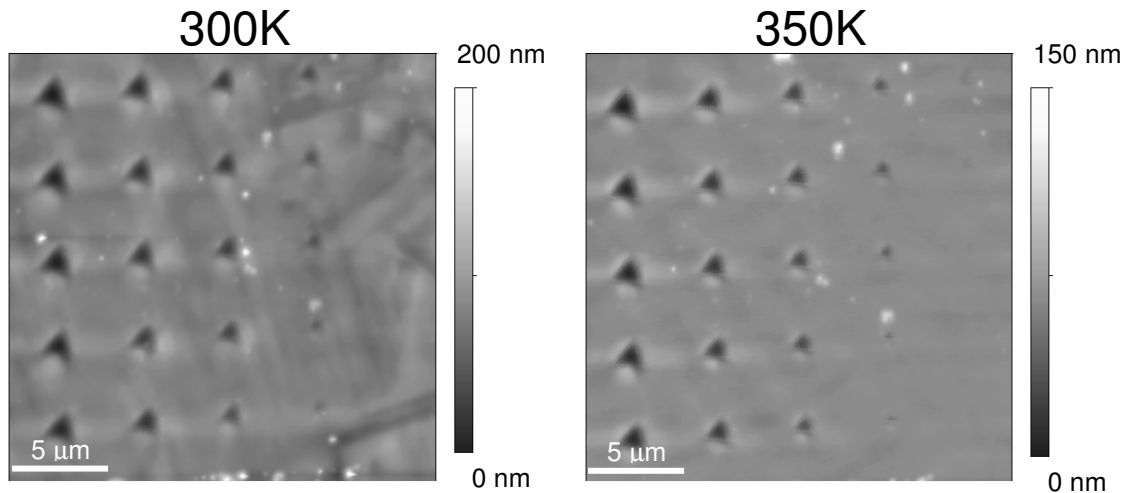


**Figure 4-34.** AFM scans of a homogeneous NiTi film in the low-temperature martensite state (left) and high-temperature austenite state (right).

At 350 K, the surface was relatively smooth, as the film had been transformed to the high-temperature austenite phase. This effect can be further explained by again referencing Figure 2-1 from the literature review section. The morphology of the graded films did not show this same effect due to the high initial austenite presence at the surface (see Figure 4-35). However, the indents in the graded film still varied as the temperature was changed.

The homogeneous and graded films showed distinctly different shape memory behavior. Figure 4-36 shows the maximum indent recovery observed in both the graded and homogeneous films as a function of indentation depth. The data were fit with linear trends to show the dependence on contact depth.

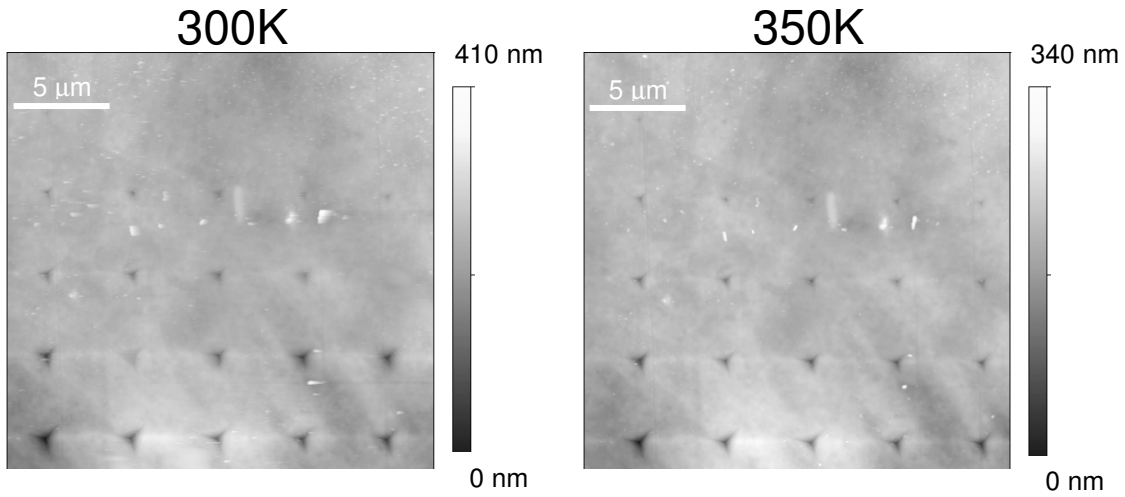


**Figure 4-35.** AFM scans of a graded 400 nm  $\text{Ni}_{47}\text{Ti}_{53}$  film on a  $\text{Ni}_{56}\text{Ti}_{44}$  substrate at 300 K (left) and 350 K (right).

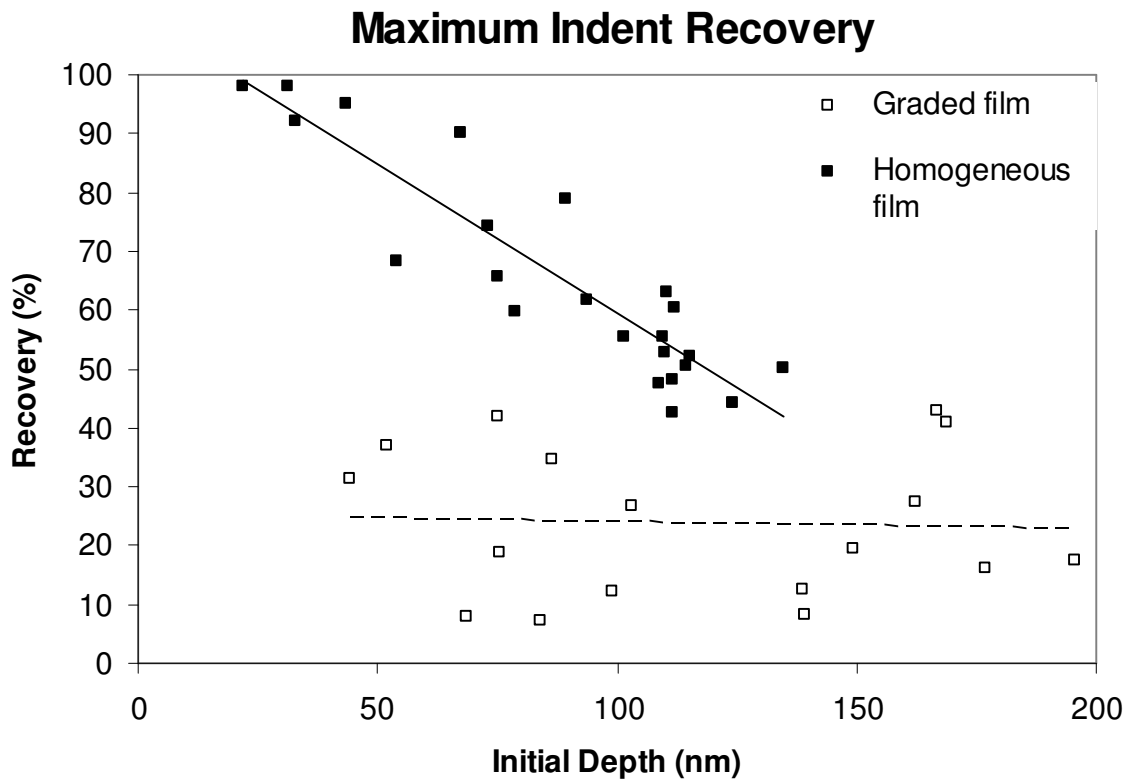


**Figure 4-36.** Maximum recovery of nanoindents observed in homogeneous film (filled) and graded film (unfilled). Data are fit to linear trends to indicate the recovery's dependence on depth.



In the case of the homogeneous film, the recovery increased as the indentation depth decreased. This result has been previously attributed to tip shape effects. The Berkovich geometry behaves more like a spherical geometry for shallow indents, due to the bluntness of the tip. As a result, there is less plastic deformation present in the shallow indents. Instead, a greater volume of material deforms by martensitic rearrangement, which in turn leads to a higher recovery. Recovery in the graded film showed no clear dependence on indent depth, likely because the tip effect for shallow indents is mitigated by the large austenite content near the surface. Furthermore, recovery in the homogeneous film appears to be converging towards the graded film between 150 nm to 200 nm, which would be consistent with the aforementioned tip effects. The recovery in the graded film could likely be improved by adjusting the processing parameters so as to yield more of the martensite phase near the surface of the film at room temperature.

#### **4.4.2.3 Studying SME in Individual Nanoindents**

Individual indents were also examined to study their height variation *in situ* as a function of temperature. Indents in a 2  $\mu\text{m}$  homogeneous NiTi film displayed the one-way SME. Figure 4-37 shows the results of temperature cycle scans for an indent that was approximately 100 nm deep before testing. Figure 4-38 shows the same test for an indent originally 70 nm deep. These indents, like all of the other indents in the array, consistently began their recovery at a temperature of approximately 330 K. For all indents, the recovery achieved at 350 K was roughly the same as the recovery observed when the film was cooled

down to room temperature. This is the well known one-way SME seen in homogeneous SMA films that have not been subjected to training.

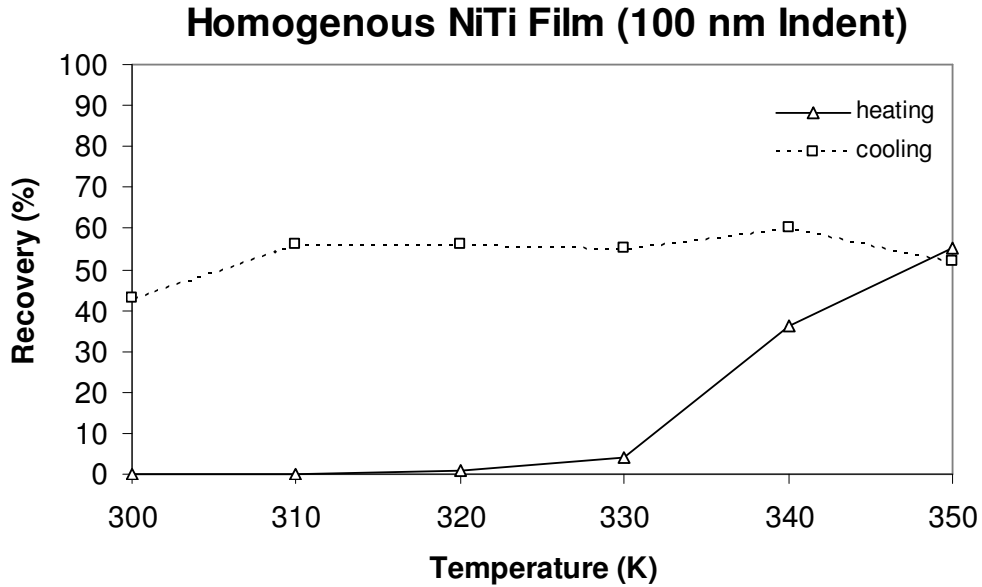


**Figure 4-37.** Recovery as a function of temperature for a 100 nm indent in a 2  $\mu\text{m}$  commercial homogeneous  $\text{Ni}_{50}\text{Ti}_{50}$  film on a Si substrate.

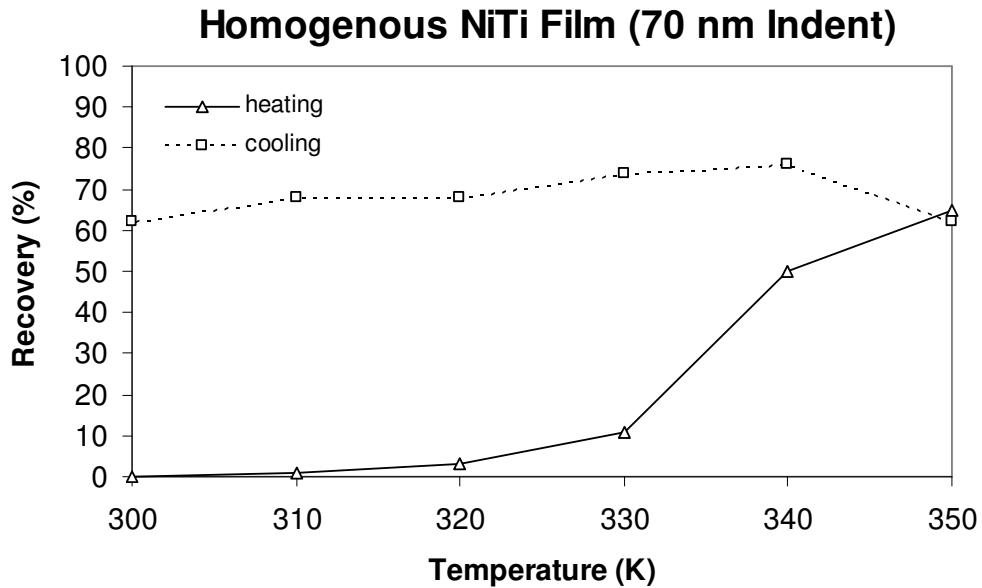


**Figure 4-38.** Recovery as a function of temperature for a 70 nm indent in a 2  $\mu\text{m}$  commercial homogeneous  $\text{Ni}_{50}\text{Ti}_{50}$  film on a Si substrate.

The magnitude of one-way reversible deformation showed a dependence on indent depth, as discussed in the previous section. In contrast, the compositionally-graded films displayed the two-way SME. The indent array did not exhibit the uniform recovery that was observed in the homogeneous film. Instead, some of the indents showed a two-way effect, while others recovered a negligible amount. This could be the result of a non-uniform deposition and/or the annealing process.

Performing the temperature cycle scans on the graded films produced a distinctly different result. Figure 4-39 shows the results of temperature cycle scans for an indent that was approximately 100 nm deep before testing. Figure 4-40 shows the same test for an indent originally 70 nm deep. Unlike the abrupt transformations seen in the homogeneous films, the recovery in the graded films was more gradual. The variation in composition through the thickness of the film resulted in a variation in the transformation temperature across the thickness. The resulting internal stresses are responsible for the two-way SME.

The recovery achieved at 350 K gradually decreased as the films were cooled, resulting in a final recovery of less than 5%. The graded films displayed a maximum recovery equal to roughly half that of the homogeneous NiTi film. The graded films also display a reduced hysteresis. From the individual indent temperature scans, it appears that the films are recovering deformation with a hysteresis of 15 °C, approximately half the hysteresis typically associated with homogeneous NiTi films [12]. This is critical for the design of microactuators, where a fast response is desirable.

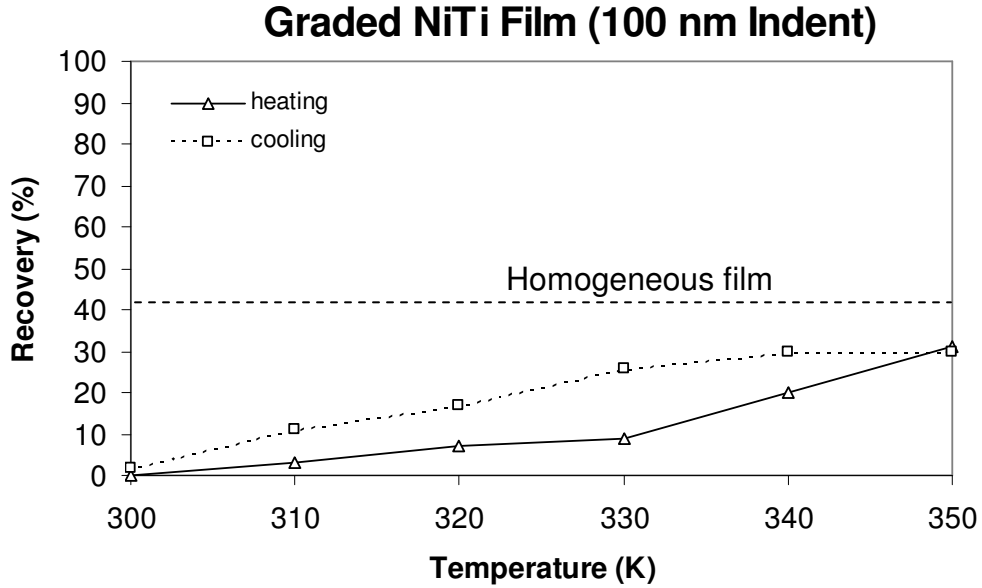


**Figure 4-39.** Recovery as a function of temperature for a 100 nm indent in a graded 400 nm  $\text{Ni}_{47}\text{Ti}_{53}$  film on a  $\text{Ni}_{56}\text{Ti}_{44}$  substrate.

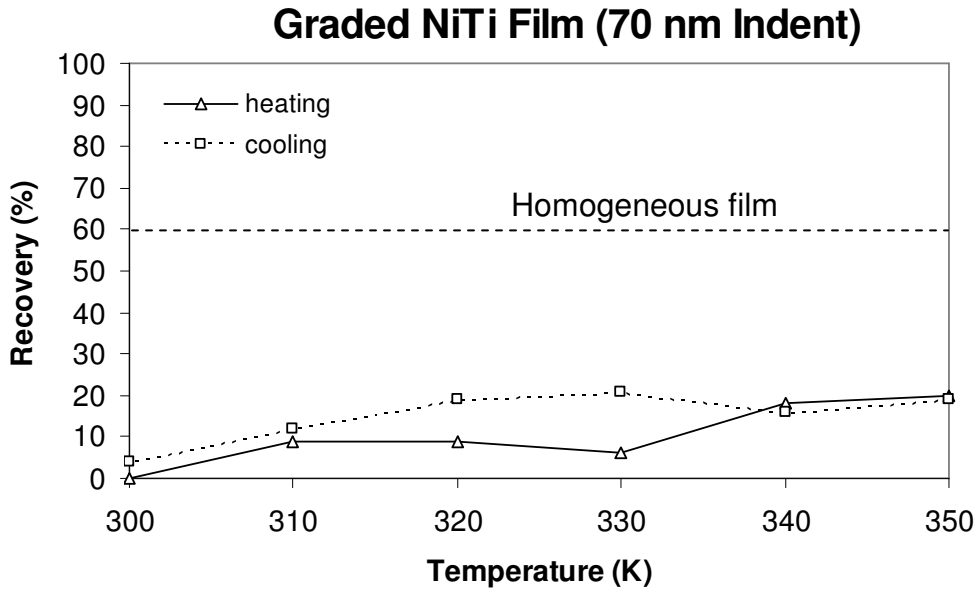


**Figure 4-40.** Recovery as a function of temperature for a 70 nm indent in a graded 400 nm  $\text{Ni}_{47}\text{Ti}_{53}$  film on a  $\text{Ni}_{56}\text{Ti}_{44}$  substrate.

The results obtained on the graded SMA films highlights the importance of the new *in situ* recovery characterization technique. First, conventional techniques for testing transformation temperatures, such as DSC, are inadequate for a graded material, where the transformation temperature varies at different

spatial locations. Second, techniques developed to test transformation behavior of films at various depths into the sample (i.e., the original recovery characterization technique discussed in section 4.4.1 or the work of Shaw et. al [34]) are limited to testing one-way recovery. A sample displaying the two-way SME will likely be indentified as a passive material because only the initial and final recoveries are measured, while the information about the recovery as the temperature is varied is not available.

## **5. Conclusions**

### **5.1. Scientific and Technical Contributions**

#### **5.1.1. Method for Processing Compositionally-Graded SMA Films with Intrinsic Two-Way SME using Diffusion Modification**

This work is the first attempt at creating compositionally-graded shape memory alloy thin films using multilayer deposition combined with a diffusion modification process. The technique was developed by sputter depositing onto a near equiatomic NiTi film or substrate using a NiTi target of a slightly different composition. Heating the films was shown to produce diffusion across the film-film or film-substrate interfaces. Subsequent tests showed that this graded interface resulted in the films exhibiting an intrinsic two-way SME as fabricated, an effect only seen in homogeneous films after extensive training. The method allows different kinds of graded films to be designed by varying the composition and thickness of the base layers and the time allowed for annealing.

#### **5.1.2. Using Nanoindentation to Characterize Extent of Graded Interface in Graded Films**

A nanoindentation technique was developed that enabled us to rapidly test the mechanical properties of films at various depths and then predict the extent of the graded interface. A self-similar relationship between elastic modulus and contact depth was observed for NiTi films of varying thickness. This similarity was shown to deviate for films thicker than approximately 500 nm, indicating that the diffusing species was not given ample time to reach the surface. This cutoff

film thickness was used as a characteristic diffusion length to approximate the diffusion coefficient of titanium-rich NiTi migrating into nickel-rich NiTi. Given the temperature and time of the annealing process, a diffusion coefficient of  $10^{-16}$   $\text{m}^2\text{s}^{-1}$  was predicted. This value agreed (within the same order of magnitude) with reported diffusion coefficients for a similar NiTi system. The developed technique also has the potential to be applied to general graded film systems.

### **5.1.3. Analyzing the Nanoindentation Response on Actively-Transforming and Graded Films**

An analysis was developed that helped advance the understanding of the nanoindentation response on a graded and phase-transforming thin film. The analysis was built on a previously-reported theory on the indentation response of a passive (no ability to change crystal structure under mechanical loading) and homogeneous film on a substrate with a different elastic modulus. The model improved on the old analysis by allowing for the properties to vary in the direction normal to the surface of the film. The model also accounts for the isothermal phase transformation that can occur during indentation when the mechanical stress reaches a critical point. The model agreed with experimental results obtained on a graded NiTi films.

### **5.1.4. Developing a Nanoscale Technique for Characterizing Recovery of Inelastic Deformation in SMA films**

A nanoscale technique for characterizing the recovery of inelastic deformation caused by nanoindentation was developed. Arrays of indents of varying depth were imaged with an AFM equipped with a heating stage. This

method allowed the heights of the nanoindents to be monitored *in situ* as the temperature of the films were varied. The recovery as a function of film temperature was calculated and used to determine the transformation temperatures. Tests on a homogeneous NiTi film showed a one-way SME, with the percent recovered depending on the initial depth of the indent. Tests on a graded NiTi film showed the two-way SME, with a depth-independent recovery. This technique is also a combinatorial approach to characterizing recovery in SMA films. Scanning an array with indents of varying height *in situ* allows for rapid characterization and the elimination of separate tests.

#### **5.1.5. Applying *in situ* Recovery Technique to Characterize Graded Films: Two-way SME and Reduced Hysteresis**

The graded films fabricated in this work were characterized using the *in situ* recovery characterization technique. The technique was used to show the two-way SME of the films that resulted from the compositional gradient. In addition, the graded films showed a narrower hysteresis when compared to their homogeneous counterparts. Most homogeneous NiTi films show a hysteresis of approximately 30 °C [12], while the graded films produced in this study showed a hysteresis of approximately half of that. This has important applications in the MEMS community, where high frequency actuators are desirable for actuation.

## **5.2. Future Work**

Throughout this investigation, a number of insights were identified which require additional work in order to realize their scientific potential.



### 5.2.1. Optimize Performance of SMA Films

#### *Optimizing compositional gradient to maximize martensite-to-austenite ratio*

To date, the films processed have been highly austenitic at room temperature which has limited the SME. The SME has been shown to be optimized for the NiTi system at room temperature around the equiatomic composition. The graded films sputtered up until now have had a small equiatomic band near the middle of the graded interface. The intent of this design was to produce a concentration gradient large enough to cause a diffusion band of at least a few hundred nanometers. This goal was realized, as shown by the nanoindentation self-similarity results, but it came at a cost. The transformation temperature varied along this interface which was responsible for the two-way SME, but the magnitude of recovery was nearly 50% of the magnitude recovered in the commercial homogeneous film. This was due to the relatively small amount of martensite present in the compositional gradient at room temperature. The films were nanoindented at room temperature, so the thin band of martensite was the only element available to accommodate the deformation through martensitic rearrangement.

The films to be processed in the future will be closer to the equiatomic NiTi composition, meaning that the SME will be more pronounced for the entire thickness, not limited to the center of the graded interface. This will require using layers with a difference in composition of around one or two atomic percent, instead of the eight or nine atomic percent used in this study.

*Produce films with larger grains by using a longer annealing process*

The films produced to date have consisted of grains on the order of 50 nm in size. Films with larger grains (on the order of hundreds of nanometers) will reduce the number of grain boundaries and improve the overall SME. In addition, if the grain sizes are large enough so that a nanoindent can be contained within a single grain, the response of the material may be approximated as a single crystal. A single crystal greatly simplifies the system and makes a modeling verification much easier.

A longer annealing process will also compliment the strategy of switching to a multilayer system with smaller differences in composition. The diffusion coefficient will be reduced compared to the original system, so the annealing time will need to be increased in order to get diffusion interfaces comparable to the original graded films. However, the longer annealing time and larger grain sizes may also reduce the gradient effect in the films.

### **5.2.2. Characterize Mechanical Properties of Films Further into Graded Region**

*Nanoindent graded films with 40 nm cube corner probe*

To date, the films have been indented with a 150 nm radius Berkovich diamond tip. Given the loading limits of the nanoindenter, this has restricted the indentation depth to approximately 300 nm for the NiTi system. Testing the same films with a 40 nm cube corner tip will allow for deeper indents to be made; the expectation is that indents of 500 nm will be possible with the smaller probe. In addition to tip size, the included angle of the 40 nm tip is 90°, significantly

sharper than the  $142^\circ$  angle in the Berkovich geometry. Penetrating deeper into the film will yield more information about the mechanical properties in the graded interface and provide more data to verify the theory of indentation on a graded and active film. The smaller radius of curvature will also reduce the tip size effects; as a rule of thumb, indents less than  $1/3$  of the tip radius can be expected to encounter size effect errors. This threshold is currently at around 50 nm for the Berkovich tip but could be improved to approximately 10-15 nm with the smaller cube corner probe.

#### *Nanoindent cross-section of graded films using 40 nm cube corner probe*

The smaller cube corner probe will also provide the opportunity to test the mechanical properties of the cross section of the graded films, instead of relying on indents normal to the surface of the films. This has the potential to show the gradient in mechanical properties more directly, provided the area is wide enough to perform several indents within the interface.

#### **5.2.3. Indent SMA Films with Spherical Probe for Recovery Tests**

The technique developed to characterize recovery of inelastic deformation in the SMA films was complicated by the inconsistent indent geometries due to tip size effects. For indents smaller than approximately 100 nm, the deformation was more spherical in shape due to the bluntness of the tip. Conversely, indents larger than 100 nm were shaped more like the pyramidal Berkovich geometry. The larger indents were found to recover less deformation, which was attributed to the higher percentage of plastic deformation associated with the sharper

indent. This can be avoided by indenting the films with a spherical indenter. Indents of all sizes will have the same semi-spherical geometry, thus making it easier to compare the recovery in indents of varying size. However, the tips will not be able to penetrate as far into the films with the spherical indenter.

#### **5.2.4. Implement Graded Film into MEMS Device**

The two-way SME was successfully demonstrated for the graded NiTi films, as shown by the *in situ* AFM recovery tests. The next step is to remove the films from their substrates and test their bulk mechanical properties using microtensile testing. Once this information is available, it will be possible to implement them into actual MEMS devices and test their practical use.

## Appendix

The following table is a list of specimens that were fabricated during the course of this research, but were not necessary to characterize. However, they could be used in future research investigations.

**Table II**

Date	Specimen	Heat Treatment	Tests on Sample
05.24.2006	800 nm Ni <sub>47</sub> Ti <sub>53</sub> on Si (100)	40 min @ 550 °C	none
06.13.2006	800 nm Ni <sub>47</sub> Ti <sub>53</sub> on Si (100)	30 min @ 575 °C	none
06.14.2006	800 nm Ti on Si (100)	30 min @ 500 °C	none
06.16.2006	1 μm Ti on 1 μm Ni <sub>47</sub> Ti <sub>53</sub> on Si (100)	30 min @ 400 °C	none
06.20.2006	600 nm Ti on 1 μm Ni <sub>47</sub> Ti <sub>53</sub> on Si (100)	20 min @ 450 °C	none
07.11.2006	800 nm Ni <sub>47</sub> Ti <sub>53</sub> on Si (100)	Heat lamp 30 min	none
07.20.2006	1.5 μm Ni <sub>47</sub> Ti <sub>53</sub> on 500 nm Ti on Si (100)	30 min @ 450 °C	none
07.21.2006	1.5 μm Ni <sub>47</sub> Ti <sub>53</sub> on 500 nm Ti on Si (100)	30 min @ 500 °C	none
08.16.2006	3 μm Ni <sub>47</sub> Ti <sub>53</sub> on Ni <sub>56</sub> Ti <sub>44</sub> substrate	15 min @ 550 °C	none
08.18.2006	1.5 μm Ti on Si (100)	none	none
08.23.2006	3 μm Ti on Si (100)	none	none
10.09.2006	1.5 μm Ni <sub>47</sub> Ti <sub>53</sub> on Ni <sub>56</sub> Ti <sub>44</sub> substrate	none	none
01.04.2007	1.5 μm Ni <sub>47</sub> Ti <sub>53</sub> on glass substrate	30 min @ 500 °C	none
02.14.2007	400 nm Ni <sub>47</sub> Ti <sub>53</sub> on Ni <sub>56</sub> Ti <sub>44</sub> substrate	40 min @ 550 °C	none
08.28.2007	3 μm Ni <sub>50</sub> Ti <sub>50</sub> on Si (100)	none	none
09.17.2007	200 nm Ni <sub>47</sub> Ti <sub>53</sub> on 2 μm Ni <sub>52</sub> Ti <sub>48</sub> on Si (100)	60 min @ 525 °C	none
09.19.2007	200 nm Ni <sub>47</sub> Ti <sub>53</sub> on 2 μm Ni <sub>52</sub> Ti <sub>48</sub> on Si (100)	none	none
09.20.2007	200 nm Ni <sub>47</sub> Ti <sub>53</sub> on 2 μm Ni <sub>52</sub> Ti <sub>48</sub> on Si (100)	30 min @ 525 °C	none
02.13.2008	1.5 μm Ni <sub>47</sub> Ti <sub>53</sub> on Si (100)	none	none
02.14.2008	1.5 μm Cu on Si (100)	none	none

**Table 2.** This table is a list of specimens made that were fabricated but not tested in this research effort. However, the samples have been retained in case a need to characterize them arises in the future.

## References

- [1] E. Baldwin, A. Rabiei, Materials Research Society Symposium Proceedings 785 (2004).
- [2] L. Gian, X. Xiao, Q. Sun, T. Yu, Applied Physics Letters 84 (2004) 1076-1078.
- [3] J. Gill, K. Ho, G. Carman, Journal of MicroElectroMechanicalSystems 11 (2002) 68-77.
- [4] E. Hornbogen, V. Mertinger, D. Wurtzel, Scripta Materialia 44 (2001) 171-178.
- [5] W. Tang, B. Sundman, R. Sandstroem, C. Qiu, Acta Materialia 47 (1999) 3457-3468.
- [6] W. Buehler, J. Gilfrich, R. Wiley, Journal of Applied Physics 34 (1963) 1475-1477.
- [7] T. Duerig, A. Pelton, D. Stoeckel, Materials Science and Engineering A 273-275 (1999) 149-160.
- [8] K. Otsuka, T. Kakeshita, MRS Bulletin 27 (2002) 91-100.
- [9] A. Pelton, T. Duerig, B. Berg, D. Hodgson, M. Mertmann, M. Mitchell, J. Profit, M. Wu, J. Yang, Advanced Materials and Processes October (2005) 63-65.
- [10] R. Adharapurapu, K. Vecchio, Experimental Mechanics 47 (2007) 365-371.
- [11] A. Pelton, T. Duerig, D. Stoeckel, Minimally Invasive Therapy and Allied Technology 13 (2004) 218-221.
- [12] Y. Fu, H. Du, W. Huang, S. Zhang, M. Hu, Sensors and Actuators A 112 (2004) 395-408.
- [13] G. Airoidi, A. Corsi, G. Riva, Materials Science and Engineering A 241 (1998) 233-240.
- [14] A. Gyobu, Y. Kawamura, T. Saburi, M. Asai, Materials Science and Engineering A 312 (2001) 227-231.
- [15] Y. Yang, H. Jia, Z. Zhang, H. Shen, A. Hu, Y. Wang, Materials Letters 22 (1995) 137-140.
- [16] N. Schell, R. Martins, F. Fernandes, Applied Physics A 81 (2005) 1441-1445.

- [17] D. Xu, L. Wang, G. Ding, Y. Zhou, A. Yu, B. Cai, *Sensors and Actuators A* 93 (2001) 87-92.
- [18] K. Ho, G. Carman, *Thin Solid Films* 370 (2000) 18-29.
- [19] R. Martins, N. Schell, R. Silva, F. Fernandes, *Nuclear Instruments and Methods in Physics Research B* 238 (2005) 319-322.
- [20] S. Suresh, *Science* 292 (2001) 2447-2451.
- [21] S. Takabayashi, K. Tanino, S. Fukumoto, Y. Mimatsu, S. Yamashita, Y. Ichikawa, *Japanese Journal of Applied Physics, Part 1: Regular Papers, Short Notes & Review Papers* 35 (1996) 200-204.
- [22] D. Ma, C. Ong, S. Wong, *Journal of Materials Research* 19 (2004) 2144-2151.
- [23] D. Ma, T. Zhang, C. Ong, *Journal of Materials Research* 21 (2006) 225-233.
- [24] W. Oliver, G. Pharr, *Journal of Materials Research* 19 (2004) 3-20.
- [25] Y. Cao, S. Allameh, D. Nankivil, S. Sethiaraj, T. Otit, W. Soboyejo, *Materials Science and Engineering A* 427 (2006) 232-240.
- [26] S. Han, R. Shah, R. Banerjee, G. Viswanathan, B. Clemens, W. Nix, *Acta Materialia* 53 (2005) 2059-2067.
- [27] P. Nagy, P. Horvath, D. Aranyi, E. Kalman, *Current Applied Physics* 6 (2006) 154-160.
- [28] Z. Xie, M. Hoffman, R. Moon, P. Munroe, *Journal of Materials Research* 21 (2006) 437-447.
- [29] H. Jang, D. Farkas, *Materials Letters* 61 (2007) 868-871.
- [30] W. C. Oliver, G. M. Pharr, *Journal of Materials Research* 7 (1992) 1564-1583.
- [31] W. Crone, H. Brock, A. Creuziger, *Experimental Mechanics* 47 (2007) 133-142.
- [32] K. Komvopoulos, X. Ma, *Applied Physics Letters* 87 (2005) 2631081-2631083.
- [33] W. Ni, Y. Cheng, D. Grummon, *Applied Physics Letters* 82 (2003) 2811-2813.
- [34] G. Shaw, D. Stone, A. Johnson, A. Ellis, W. Crone, *Applied Physics Letters* 83 (2003) 257-259.

- [35] R. Armstrong, L. Ferranti, N. Thadhani, *International Journal of Refractory Metals and Hard Materials* 24 (2006) 11-16.
- [36] W. Nix, H. Gao, *Journal of the Mechanics and Physics of Solids* 46 (1998) 411-425.
- [37] R. Saha, W. Nix, *Acta Materialia* 50 (2002) 23-38.
- [38] Y. Huang, F. Zhang, K. Hwang, W. Nix, G. Pharr, G. Feng, *Journal of the Mechanics and Physics of Solids* 54 (2006) 1668-1686.
- [39] S. Han, R. Saha, W. Nix, *Acta Materialia* 54 (2006) 1571-1581.
- [40] N. Botterill, D. Grant, *Materials Science and Engineering A* 378 (2004) 424-428.
- [41] J. Busch, A. Johnson, C. Lee, D. Stevenson, *Journal of Applied Physics* 68 (1990) 6224-6228.
- [42] Q. He, W. Huang, M. Hong, M. Wu, Y. Fu, T. Chong, F. Chellet, H. Du, *Smart Materials and Structures* 13 (2004) 977-982.
- [43] A. Johnson, *Journal of Micromechanics and Microengineering* 1 (1991) 34-41.
- [44] R. Martins, N. Schell, A. Mücklich, H. Reuther, M. Beckers, R. Silva, L. Pereira, R. Fernandes, *Applied Physics A* 91 (2008) 291-299.
- [45] D. Ford, S. White, *Acta Materialia* 44 (1996) 2295-2307.
- [46] A. Ramirez, H. Ni, H. Lee, *Materials Science and Engineering A* 438-440 (2006) 703-709.
- [47] G. Michal, R. Sinclair, *Acta Cryst.* B37 (1981) 1803-1807.
- [48] M. Sanati, R. Albers, F. Pinski, *Physical Review B* 58 (1998) 13590-13593.
- [49] A. Roytburd, *Materials Science and Engineering A* 273-275 (1999) 1-10.
- [50] A. Roytburd, T. Kim, Q. Su, J. Slutsker, M. Wuttig, *Acta Materialia* 46 (1998) 5095-5107.
- [51] J. Ryhaenen, PhD Dissertation, University of Oulu, Finland (1999).
- [52] P. Krulevitch, A. Lee, P. Ramsey, J. Trevino, J. Hamilton, M. Northrup, *Journal of MicroElectroMechanical Systems* 5 (1996) 270-282.
- [53] E. Wibowo, C. Kwok, *Journal of Micromechanics and Microengineering* 16 (2006) 101-108.



- [54] Y. Zhang, Y. Cheng, D. Grummon, *Journal of Applied Physics* 98 (2005) 0335051-0335054.
- [55] R. Benedictus, K. Han, C. Traeholt, A. Boettgers, E. Mittemeijer, *Acta Materialia* 46 (1998) 5491-5508.
- [56] T. Lehnert, S. Crevoiserat, R. Gotthardt, *Journal of Materials Science* 37 (2002) 1523-1533.
- [57] H. Cho, H. Kim, S. Miyazaki, *Science and Technology of Advanced Materials* 6 (2005) 678-683.
- [58] X. Wang, J. Vlassak, *Scripta Materialia* 54 (2006) 925-930.
- [59] C. Frick, T. Lang, K. Spark, K. Gall, *Acta Materialia* 54 (2006) 2223-2234.
- [60] K. Johnson, (Cambridge University Press, Cambridge) (1994) 171.
- [61] J. Uchil, F. Fernandes, K. Mahesh, *Materials Characterization* 58 (2007) 243-248.
- [62] X. Ma, K. Komvopoulos, *Applied Physics Letters* 84 (2004) 4274-4276.
- [63] X. Ma, K. Komvopoulos, *Applied Physics Letters* 83 (2003) 3773-3775.
- [64] A. Gouldstone, N. Chollacoop, M. Dao, J. Li, A. Minor, Y. Shen, *Acta Materialia* 55 (2007) 4015-4039.
- [65] Hysitron User Manual (2004).
- [66] G. Pharr, W. Oliver, F. Brotzen, *Journal of Materials Research* 7 (1992) 613-617.
- [67] I. Sneddon, *International Journal of Solids and Structures* 3 (1965) 47-57.
- [68] R. King, *International Journal of Solids and Structures* 23 (1987) 1657-1664.
- [69] M. Chen, D. Liu, C. You, X. Yang, Z. Cui, *Surface & Coatings Technology* 201 (2007) 5688-5691.
- [70] M. Finot, S. Suresh, *Journal of the Mechanics and Physics of Solids* 44 (1996) 683-721.
- [71] A. Ramirez, R. Saha, *Applied Physics Letters* 85 (2004) 5215-5217.
- [72] H. Wen, X. Wang, C. Zhong, L. Shu, L. Li, *Journal of the American Ceramic Society* 90 (2007) 2441-2445.

- [73] R. Yamauchi, S. Hata, J. Sakurai, A. Shimokohbe, *Japanese Journal of Applied Physics* 45 (2006) 5911-5919.
- [74] J. Zhai, X. Yao, Z. Xu, H. Chen, *Journal of Crystal Growth* 286 (2006) 37-41.
- [75] V. Lyahovitskaya, Y. Feldman, I. Zon, E. Wachtel, I. Lubomirsky, A. Roytburd, *Advanced Materials* 17 (2005) 1956-1960.
- [76] H. Tian, H. Chan, C. Choy, K. No, *Materials Science and Engineering B* 103 (2003) 246-252.
- [77] L. Freund, *Journal of the Mechanics and Physics of Solids* 44 (1996) 723-736.
- [78] J. Kruff, *Functionally graded nickel-alumina composites for armor applications* Master's thesis, University of Maryland (2007).
- [79] A. Gerson, A. Kota, H. Bruck, *Characterization of quasi-static mechanical properties of polymer nanocomposites using a new combinatorial approach. To appear in Journal of Composite Materials* (2009).
- [80] A. Giannakopoulos, S. Suresh, *International Journal of Solids and Structures* 34 (1997) 2357-2392.
- [81] A. Kota, L. Murphy, T. Stroehmer, D. Bigio, H. Bruck, D. Powell, *American Institute of Chemical Engineers Journal* 54 (2008) 1895-1900.
- [82] J. Walls, R. Smith, *Elesvier Science, Inc., New York* (1994) 25.
- [83] D. Woodruff, T. Delchar, *Cambridge University Press, Cambridge* (1994) 171.
- [84] S. Shabalovskaya, H. Tian, J. Anderegg, D. Schryvers, W. Carroll, J. Humbeek, *Biomaterials* 30 (2009) 468-477.
- [85] B. Clarke, W. Carroll, Y. Rochev, M. Hynes, D. Bradley, D. Plumley, *Journal of Biomedical Materials Research* 79A (2006) 61-70.
- [86] D. Mueller, U. Aebi, A. Engel, M.E. Mueller Institute, Basel, Switzerland  
Online resource (1996)  
<http://www.mih.unibas.ch/Booklet/Booklet96/Booklet96.html>.
- [87] B. Warren, *X-ray Diffraction*, Addison Wesley Publishing Company (1969).
- [88] E. Baldwin, B. Thomas, J. Lee, A. Rabiei, *Materials Science and Engineering A* 434 (2006) 124-130.
- [89] G. Fleury, C. Malhaire, C. Populaire, M. Verdier, A. Devos, P. Charvet, J. Polizzi, *Sensors and Actuators B* 126 (2007).

- [90] Y. Fu, H. Du, Surface & Coatings Technology 153 (2002) 100-105.
- [91] Y. Fu, H. Du, S. Zhang, Surface & Coatings Technology 167 (2003) 120-128.
- [92] D. Cole, H. Bruck, A. Roytburd, Journal of Applied Physics 103 (2008) 064315.
- [93] G. Bastin, G. Rieck, Metallurgical Transactions 5 (1974) 1827-1831.
- [94] G. Erdelyi, Z. Erdelyi, D. Beke, J. Bernardini, C. LExcellent, Physical Review B 62 (2000) 11284-11287.
- [95] M. Maaza, C. Sella, J. Ambroise, M. Kaabouchi, M. Miloche, F. Wehling, M. Groos, Journal of Applied Crystallography 26 (1993) 334-342.
- [96] S. Stemmer, G. Duscher, C. Scheu, A. Heuer, M. Rühle, Journal of Materials Research 12 (1997) 1734-1740.
- [97] D. Cole, A. Roytburd, H. Bruck, Nanomechanical characterization of graded NiTi films fabricated through diffusion modification. *To appear in Strain, 2009.*
- [98] T. Fang, W. Chang, Microelectronic Engineering 65 (2003) 231-238.
- [99] C. Wang, S. Jian, J. Jang, Y. Lai, P. Yang, Applied Surface Science 255 (2008) 3240-3250.
- [100] K. Tanaka, Res. Mechanica 18 (1986) 251-263.
- [101] C. LExcellent, S. Moyne, A. Ishida, S. Miyazaki, Thin Solid Films 324 (1998) 184-189.
- [102] J. Broekmaat, A. Brinkman, D. Blank, G. Rijnders, Applied Physics Letters 92 (2008) 0431021-0431023.
- [103] C. Park, T. Shultz, I. Dutta, Review of Scientific Instruments 75 (2004) 4662-4670.
- [104] D. Cole, H. Jin, W. Lu, A. Roytburd, H. Bruck, A nanoscale technique for characterizing recovery of inelastic deformation in graded shape memory alloy films. *Submitted to Applied Physics Letters (2009).*